MODULAR MULTILEVEL MATRIX CONVERTER FOR FRACTIONAL FREQUENCY TRANSMISSION IN OFFSHORE WIND POWER INTEGRATION

by

LUO, JIAJIE

A thesis submitted to

The University of Birmingham

for the degree of

DOCTOR OF PHILOSOPHY

Department of EESE,

School of Engineering

The University of Birmingham

Apr 2019

ABSTRACT

Offshore wind power plays an important role in reducing carbon emission and the reliability on fossil fuel. The traditional high voltage AC transmission suffers from the disadvantage of high charging reactive current and therefore the maximum transmission distance is very limited. Fractional frequency transmission (FFT) is proposed to overcome this difficulty. With the offshore side operating at one third of the onshore grid frequency, the reactive current demand of FFT is greatly decreased. Modular multilevel matrix converter (M^3C) is the core component of the FFT. With the advantages of easy scalability, excellent controllability and low loss, M^3C is considered to be the future-generation AC/AC converter for offshore wind transmission and other high power applications. To start with, the operating principle and the control strategy of the M^3C are presented. It is proven that M^3C is capable as the frequency changer for FFT.

Although M^3C FFT has various technical advantages, it is necessary to look into economic aspects to evaluate its feasibility in offshore wind power industry. A cost analysis of M^3C FFT as well as a cost comparison with modular multilevel converter (MMC) high voltage DC (HVDC) transmission is presented. A cost model is developed considering capital cost and time-related costs including unavailability cost, operation and maintenance cost and power loss cost for different components in offshore wind power systems. Cost elements taking up large proportions of the total cost are identified and the cost-effective transmission distance ranges for the two technologies are calculated. Also, sensitivity analysis is conducted to investigate the influence of various parameters on the cost comparison.

It is shown that M^3C FFT is a competitive candidate for offshore wind power transmission particularly at medium distance. Hence, there is need of a model to study its small signal

stability and its influence on existing power systems. A small signal model of M^3C is proposed for FFT system which considers the dynamics of AC currents from both sides, the sub-module capacitor voltage with DC and ripple components and the control system. In addition, a small signal analysis is presented to investigate the effect of controller parameters and sub-module capacitance on the small signal stability of the system. The small signal model is easy to implement and benefits system stability study and controller design.

Harmonic analysis is crucial from the stability point of view. In M^3C, two frequencies from both AC sides couple and produce a complex harmonic profile due to the interactions between the arm quantities and the fast-switching sub-modules. A harmonic analysis method is proposed to determine how the harmonic components at various frequencies are generated in M^3C. The harmonic components are quantified and factors that have large impact on the harmonic magnitude are discussed. The influences of different types of harmonics on the converter and external AC systems are analysed. Analyses are conducted on sub-module capacitors and arm inductors to give a guideline on their value selection to limit the harmonic level. A zero-sequence current mitigation controller is implemented and tested for M^3C.

Time domain simulations are carried out in the electromagnetic simulation tool Real Time Digital Simulator (RTDS) in order to validate the correctness and accuracy of the M^3C control strategy, the proposed small signal model and the harmonic analysis.

ACKNOWLEDGEMENT

Firstly, I want to express my deepest and most sincere gratitude to my lead supervisor Prof. Xiao-Ping Zhang, who expanded my research horizon and led me all the way through my PhD study. His wisdom is like a beacon and I never lost my way and hope with his guidance.

Secondly, I thank my co-supervisor Dr. Pietro Tricoli, who taught me knowledge of power electronics. Next, a special thank you goes to Dr Ying Xue and Dr Jianing Li, for their motivation, encouragement and help on my research. Also thanks for providing me invaluable advice on writing this thesis.

In addition, I would like to express my appreciation to all my friends, especially my colleagues in the research group. They made my days interesting and gave me a treasure trove of fun memories. They include: Dr Zuanhong Yan and Dr Xianxian Zhao in the offshore wind power sub-research group, Dr Conghuan Yang, Kanghui Gu, Min Zhao, Kai Lin, Cong Wu, Nan Chen, Longmao Fan and Chenyixuan Ni.

Finally, I would like to thank my family. I am grateful to my wife Xinyue Chen, who always backs me up when I am in trouble. I never feel lonely with her company. I thank my parents Zhigang Luo and Jiehua Zhou, my sister Jiahui Luo and also my grandparents. Their everlasting love and consistent support are my constant sources of power.

CONTENTS

LIST OF FIGURES

LIST OF TABLES

LIST OF ABBREVIATION

DFIG	doubly-fed induction generator
EMT	electromagnetic transient
FFT	fractional frequency transmission
FFTS	fractional frequency transmission system
HVAC	high voltage AC
HVDC	high voltage DC
IGBT	insulated-gate bipolar transistor
LCOE	levelized cost of energy
MMC	modular multilevel converter
M^3C	modular multilevel matrix converter
NLM	nearest level modulation
O&M	operation and maintenance
PLL	phase lock loop
PMSG	permanent magnet synchronous generator
RTDS	Real Time Digital Simulator
SVM	space vector modulation
THD	total harmonic distortion
rTHD	revised total harmonic distortion
VSC	voltage source converter

NOMENCLATURE

Symbol	Description	Units
i_x	$(x = a, b, c)$ Three phase current at low frequency side	A
i_y	$(y = u, v, w)$ Three phase current at high frequency side	A
u_x	$(x = a, b, c)$ Three phase voltage at low frequency side	V
u_y	$(y = u, v, w)$ Three phase voltage at high frequency side	V
I_a	Magnitude of the low frequency current component	A
I_u	Magnitude of the high frequency current component	A
ω_1	Angular frequency at low frequency side	rad/s
ω_3	Angular frequency at high frequency side	rad/s
β_1	Current phase angle of low frequency component in i_{au}	°
β_3	Current phase angle of high frequency component in i_{au}	°
E_a	Magnitude of the modulation voltage at low frequency side	V
E_u	Magnitude of the modulation voltage at high frequency side	V
α_1	Phase angle of the modulation voltage at low frequency side	°

α_3	Phase angle of the modulation voltage at high frequency side	°
U_{DC}	Total arm DC voltage	V
v_{auref}	Arm *au* voltage reference	V
$v_{dc\_measured}$	Measured average voltage of sub-modules in an arm	V
$NORD_{au}$	Order of inserted sub-module number for arm *au*	-
v_{xy}	$(x = a, b, c;\ y = u, v, w)$ Arm voltage of *xy*	V
i_{xy}	$(x = a, b, c;\ y = u, v, w)$ Arm current of *xy*	A
R	Arm resistance	Ω
L	Arm inductance	H
E_{d20}	D axis voltage reference from vector control at low frequency side	V
E_{q20}	Q axis voltage reference from vector control at low frequency side	V
E_{d60}	D axis voltage reference from vector control at high frequency side	V
E_{q60}	Q axis voltage reference from vector control at high frequency side	V

U_{d20}	D axis voltage at low frequency side	V
U_{q20}	Q axis voltage at low frequency side	V
U_{d60}	D axis voltage at high frequency side	V
U_{q60}	Q axis voltage at high frequency side	V
I_{d20}	D axis component after DQ transformation at low frequency side	A
I_{q20}	Q axis component after DQ transformation at low frequency side	A
I_{d60}	D axis component after DQ transformation at high frequency side	A
I_{q60}	Q axis component after DQ transformation at high frequency side	A
v_{xd}	$(x = a, b, c)$ D axis voltage component after DQ transformation	V
i_{xd}	$(x = a, b, c)$ D axis current component after transformation	A
v_{xq}	$(x = a, b, c)$ Q axis voltage component after transformation	V
i_{xq}	$(x = a, b, c)$ Q axis current component after transformation	A
v_{x0}	$(x = a, b, c)$ Zero-sequence voltage component after transformation	V

i_{x0}	$(x = a, b, c)$ Zero-sequence current component after transformation	A
P_{20ref}	Active power reference at low frequency side	W
U_{dcref}	DC voltage reference	V
Q_{20ref}	Reactive power reference at low frequency side	Var
Q_{60ref}	Reactive power reference at high frequency side	Var
I_{d20ref}	D axis current reference at low frequency side	A
I_{q20ref}	Q axis current reference at low frequency side	A
I_{d60ref}	D axis current reference at high frequency side	A
I_{q60ref}	Q axis current reference at high frequency side	A
${v_{xy}}^*$	$(x = a, b, c;\ y = u, v, w)$ Voltage reference of arm *xy*	V
C_{sys}	Total system cost	£
C_{CAP_sys}	Capital cost of the system	£
C_{UA_sys}	Unavailability cost of the system	£
C_{OM_sys}	Operation and maintenance costs of the system	£

C_{PL_sys}	Power loss cost of the system	£
C_{NPC}	Net present cost of a long-term cost	£
C_{annual}	Annual value of a long-term cost	£
n	Offshore wind system lifetime (in Chapter 4)	year
i	Discount rate	%
C_{CAP_cab}	Capital cost of cable	£
n_{cab}	Number of submarine cable sets	-
l_{cab}	Cable length	km
c_{cab}	Submarine cable price	£m/km
UA_{sys}	Unavailability rate of the offshore wind power system	%
t_{UA_sys}	Overall unavailable time within one year	hrs
T_{year}	Overall time in hours of one year (8760 hours)	hrs
P_{rated}	Nominal power rating of the offshore wind power system	MW
CF	Capacity factor	%
EP_{wind}	Offshore wind energy price	£/MWh

UA_{wt}	Unavailability of the wind turbine	%
UA_{tran}	Unavailability of the transformer	%
UA_{cab}	Unavailability of the cable	%
UA_{con}	Unavailability of the converter	%
$k_{O\&M}$	O&M cost ratio	%
$c_{O\&M\_com}$	Annual expenditure of O&M on the component	£
C_{CAP_com}	Capital cost of the component	£
C_{PL_com}	Power loss cost of the component	£
T_{rated}	Rated equivalent operation time of the system annually	hrs
S_{xy}	$(x = a, b, c;\ y = u, v, w)$ Switching function of arm *xy*	-
S_{armi}	Switching signal of the i^{th} sub-module in an arm	-
u_{dc}	Sub-module voltage	V
i_{arm}	Arm current	A
C	Sub-module capacitance	F
n	Inserted number of sub-modules (in Chapter 5)	-

N	Total number of sub-modules in an arm	-
S_{arm}	Arm switching function	-
u_{arm}	Arm voltage:	V
T	Park transformation matrix	-
ω	Angular frequency	rad/s
U_{dc_0}	DC component of the capacitor voltage	V
U_{dc_d2}	40 Hz component of the capacitor voltage on D axis	V
U_{dc_q2}	40 Hz component of the capacitor voltage on Q axis	V
U_{dc_2}	Magnitude of the 40 Hz component of the capacitor voltage	V
θ_2	Phase angle of the 40 Hz component of the capacitor voltage	°
U_{arm_20a}	20 Hz component in arm *au* voltage	V
U_{arm_60u}	60 Hz component in arm *au* voltage	V
U_{arm_20d}	20 Hz component of arm voltage on D axis	V
U_{arm_20q}	20 Hz component of arm voltage on Q axis	V
U_{arm_60d}	60 Hz component of arm voltage on D axis	V

U_{arm_60q}	60 Hz component of arm voltage on Q axis	V
e_x	$(x = a, b, c)$ Grid voltage at low frequency side	V
e_y	$(y = u, v, w)$ Grid voltage at high frequency side	V
i_{au_20}	20 Hz component of arm *au* current	A
i_{au_60}	60 Hz component of arm *au* current	A
x_{m3c}	State variables of M^3C	-
u_{m3c}	Input variables of M^3C	-
P_{20mea}	Measured active power at low frequency side	W
ω_{1_0}	Initial value of angular frequency at low frequency side	rad/s
ω_{3_0}	Initial value of angular frequency at high frequency side	rad/s
s	Laplace operator	-
T_{mea}	First order time constant for measurement	s
x_1	State variable of 20 Hz side outer loop controller	-
x_2	State variable of 20 Hz side inner loop on D axis	-
x_3	State variable of 20 Hz side inner loop on Q axis	-

x_4	State variable of 60 Hz side outer loop controller	-
x_5	State variable of 60 Hz side inner loop on D axis	-
x_6	State variable of 60 Hz side inner loop on Q axis	-
x_7	State variable of 20 Hz side PLL (intermediate)	-
x_8	State variable of 60 Hz side PLL (intermediate)	-
x_{pll20}	State variable of 20 Hz side PLL output	-
x_{pll60}	State variable of 60 Hz side PLL output	-
k_{pn}	$(n = 1 - 6)$ Proportional gain of PI controller	-
k_{in}	$(n = 1 - 6)$ Integral gain of PI controller	-
k_{ppll}	Proportional gain of PI controller in PLL	-
k_{ipll}	Integral gain of PI controller in PLL	-
λ	Eigenvalue of a mode	-
σ	Real part of the eigenvalue	-
ω	Imaginary part of the eigenvalue	-
ξ	Damping ratio of a mode	%

i_{20}	Phase currents of the fractional frequency side	A
i_{60}	Phase currents of the grid side	A
$i_{arm}^{harmonics}$	Arm harmonic current	A
m_a	Low frequency side voltage modulation ratio	-
m_u	High frequency side voltage modulation ratio	-
u_{dc_au}	Sub-module capacitor voltage of arm *au*	V
u_{dc_xy40}	$(x = a, b, c;\ y = u, v, w)$ 40 Hz component of sub-module capacitor voltage of arm *xy*	V
u_{dc_0}	DC component of the capacitor voltage	V
u_{dc_40}	40 Hz component of the capacitor voltage	V
$u_{arm\_au\_20}$	20 Hz component of arm voltage of arm *au*	V
$u_{arm\_au\_60}$	60 Hz component of arm voltage of arm *au*	V
$u_{arm\_au\_100}$	100 Hz component of arm voltage of arm *au*	V
i_{xy_20}	$(x = a, b, c;\ y = u, v, w)$ 20 Hz component of arm current	A
i_{xy_60}	$(x = a, b, c;\ y = u, v, w)$ 60 Hz component of arm current	A
i_{xy_100}	$(x = a, b, c;\ y = u, v, w)$ 100 Hz component of arm current	A

θ_n	$(n = 1 - 15)$ Phase angles of harmonic components (in Chapter 6)	°
Z_g	Grounding impedance of transformer	Ω
Z_0	Sum of primary side and secondary side leakage impedances per phase in a transformer	Ω
I_1^p	Fundamental positive-sequence current for a three-phase system	A
I_n	$(n = 1 - 4)$ n^{th} order component of the current	A
v_0	Zero-sequence voltage	V
θ_3	Angle of the zero-sequence current (only in chapter 6.6)	°
k_{pz1}	Mitigation controller proportional gain 1	-
k_{pz2}	Mitigation controller proportional gain 2	-
k_{iz1}	Mitigation controller integral gain	-

CHAPTER 1 INTRODUCTION

This chapter is to provide a background introduction of the doctoral research. The development of renewable energy sources is introduced and the focus is on offshore wind power. Transmission technologies are discussed with an emphasis on the relatively new technology fractional frequency transmission (FFT). The key component of the technology is modular multilevel matrix converter (M^3C), whose development history is introduced. The research motivations and objectives of the study are given. And how the thesis is organised is outlined at the end of the chapter.

1.1 Research Background and Motivations

1.1.1 Renewable Sources and the Role of Offshore Wind Power

Under the pressure of carbon emission reduction and fossil fuel depletion, countries across the world are developing renewable energy with their great effort. A roadmap for 139 countries to use 100% renewable energy including wind, water and solar in all energy sectors by 2050 was published in 2017 [1]. According to this roadmap, 1.5°C global warming would be avoided and 24.3 million long-term job positions would be created. It was estimated that wind energy would take up more than one third of the production. In 2017, 70% of the generation growth is from renewable sources [2]. Renewable energy can be replenished constantly with natural processes such as sunlight, wind and water movement. Mainstream types include wind power, hydropower, solar power, geothermal power and bio energy [3]. The global capacity growth of different types of renewable energy in recent years is plotted in Fig. 1.1 [2]. As it is shown, hydropower has the largest percentage but its growth is not very rapid. Wind power ranks

second with a dramatic increase in the recent ten years. Following is solar power which also has great potential. Technologies like biofuel take up small shares but they have specific promising applications, e.g., ethanol production for transportation. The historic datasheet for the growth of renewable power in the UK [4] and worldwide [2], including wind, solar and hydro between 2010 and 2017 is given in Table 1.1. As can be seen, solar and wind have significant growth in the UK, while hydro power remains almost unchanged. The increase of solar power in the UK peaks at 2015 and slows down afterward. Worldwide, the growth of solar has an increasing trend, and growth of hydro remains rapid. The wind power growing trend rises before 2016 and dips down slightly after that. At the moment, most renewable energy capacity is from grid-connected and large-scale projects, while small distributed projects are also becoming increasingly popular. One advantage of distributed projects is that they can benefit remote and developing areas where grid integration is difficult. In terms of wind power installation, over 50 GW of wind power was installed in 2017, making a total capacity of 539 GW worldwide. Undoubtedly, it is a very promising renewable energy source.

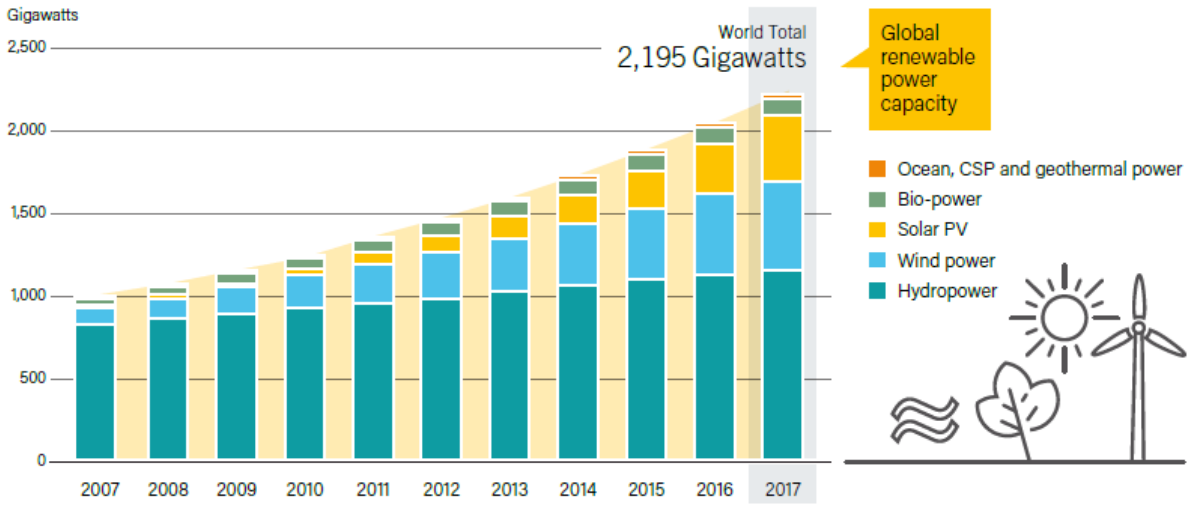

Fig. 1.1 Global renewable generation growth [2].

Table 1.1 Renewable Power Growth UK and Worldwide 2010-2017

Year	UK Renewable Power Growth (MW)			Worldwide Renewable Power Growth (MW)		
	Wind	Solar	Hydro	Wind	Solar	Hydro
2010	999	69	7	30,618	16,635	34,119
2011	1,175	905	32	39,294	30,651	30,650
2012	2,434	753	14	49,629	27,928	33,016
2013	2,252	1,184	16	31,909	38,679	44,512
2014	1,792	2,591	21	47,637	37,259	38,358
2015	1,232	4,073	48	67,610	49,984	34,818
2016	1,814	2,306	58	50,429	72,528	37,793
2017	3,465	703	26	46,712	93,752	22,448

Wind power can be divided into onshore wind and offshore wind. Early wind farms usually located onshore due to technical limitations, economic consideration and conveniences of installation and maintenance. However, with constant development for several decades, on one hand, constructing an offshore wind farm is no longer an engineering difficulty. On the other, it becomes increasingly difficult to find an ideal location on land that does not affect local residents and at the same time has high and stable wind speed. As a result, offshore wind is drawing more and more attention with advantages of rich resource and more straightforward space planning for large projects. Fig 1.2 shows the offshore wind power

installation capacity in Europe [5]. As can be seen, a rocketing trend can be observed both on the annual and the cumulative amount, particularly in the past ten years. It is anticipated that the offshore wind power sector would make prominent contribution to the net growth of renewable energy in the upcoming years. United Kingdom, Germany, Denmark, Netherlands and Belgium are the top five countries in terms of installation capacity in Europe. Beyond Europe, China is also expanding its offshore wind farms rapidly. In UK alone, there are 33 offshore wind farms operating and there are another eight under construction, which are estimated to add 4.5 GW over the following years. In 2017, UK offshore wind produced electricity of 20.8 TWh, which is the amount of 20% of the UK household need. In environmental aspect, 8.6 million tonnes of CO_2 emission was reduced thanks to the offshore wind power [6]. To sum up, offshore wind power plays an increasingly important role in power systems and de-carbonization process.

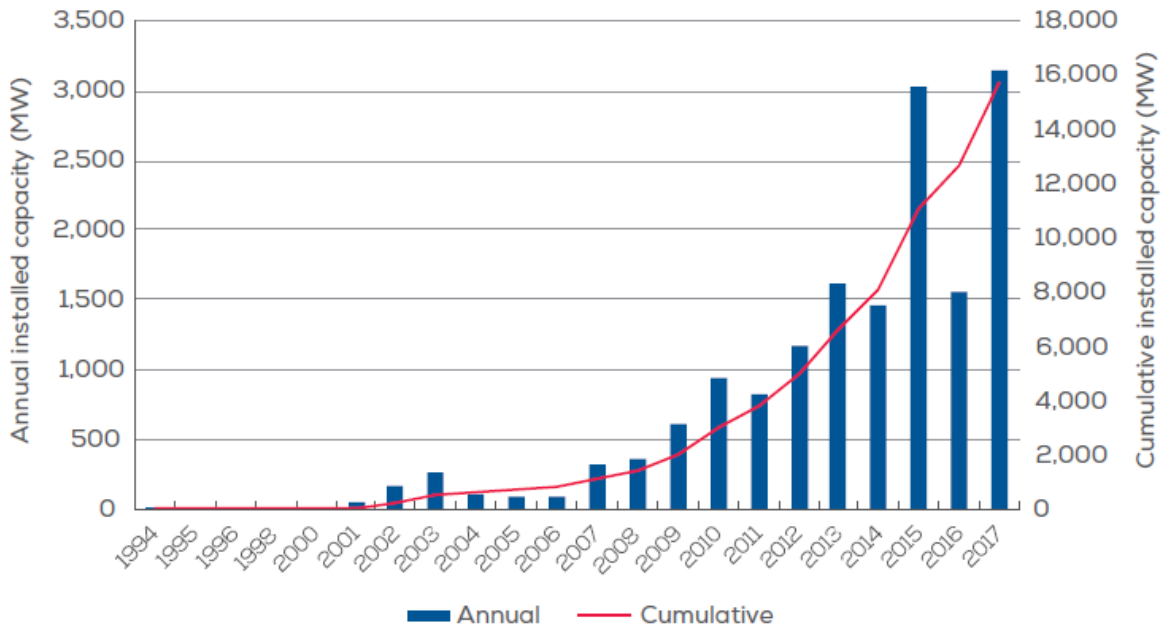

Fig. 1.2 Offshore installed capacity in Europe [5].

With those promising merits of offshore wind power, on the other hand, it also brings challenges to the existing power systems. The first problem is due to its intermittency. In unexpected high wind conditions, it is likely that power systems cannot absorb the excess amount of wind energy. For instance on October 8, 2018, Scotland became so windy that over 60 wind farms were paid £4.8m to shut down their wind turbines [7]. It reflected a fact that renewable energy development cannot be rushed over and energy storage devices need to keep up with the pace. The development of electric vehicles provides a great opportunity to offshore wind power [8]. As electric vehicles can be regarded as a source of energy storage and can be complementary to offshore wind power. If they can be well managed without impeding the functionalities of the users, it would be one of the most promising solutions to reduce carbon emission and to maximise the usage of renewable energy.

Secondly, replacing synchronous machines with converter connected renewable sources like wind or solar will reduce the total inertia of the existing power system [9]. As a result, the system stability would suffer and more research is needed in this area. Among academia, some control methods have been proposed [10, 11]. One of the ideas is to adopt a novel control method for the grid connected inverter so that it mimics the behaviour of a traditional synchronous generator. More prototypes and projects are required before they could serve the power system against the inertia problem.

Regarding the future trend, bid price of renewable energy has been decreasing for the past years and it is anticipated that the same trend would remain in the future years. The reasons can be concluded as technology innovation and scale effect. The trend of the wind turbine is to become larger both in size and in power rating. 10MW machines have been announced with a rotor diameter of over 150 m. According to [12], existing offshore wind farms have an average water depth of 27.5m and an average distance of 41km from the grid connection

point. Such a distance can be covered by the traditional AC transmission. But with the saturation of near-coast wind power development, future wind farms would inevitably move further offshore and that would certainly raise challenges for transmission technologies. In the next subsection, different technologies are introduced and their pros and cons are compared.

1.1.2 Fractional Frequency Transmission and Other Transmission Technologies

As is mentioned in the previous section, most offshore wind projects nowadays are at short distance (less than 100 km). In fact, all offshore wind farms currently operating in the UK adopts the traditional high voltage AC (HVAC) transmission [13]. In terms of the transmission technology, there is minor difference compared to onshore wind power transmission. HVAC is a mature technology and therefore it is a natural idea to transfer the technology to the offshore sector at the first place. Standardised products are available so that the overall project cost can be kept to the minimum level. However, the capacitive charging current constrains the active power capacity of the cable and this shortcoming is enlarged as the distance grows. Even with reactive compensation, it is generally regarded that HVAC cannot be applied to long distance transmission. Usually, the maximum transmission distance of HVAC is regarded as around 100 km [14, 15].

On the contrary, high voltage DC (HVDC) transmission is an ideal candidate for long distance transmission since it does not have charging current effect. The rectifier station converts the AC power to DC and then it is transmitted at DC until being converted back to AC again by the inverter station. HVDC can be categorised into Line Commutated Converter (LCC) and Voltage Source Converter (VSC). There is also a type of capacitor commutated converter proposed in order to cope with the commutation failure problem in LCC HVDC. A

capacitor is connected in series between the converter transformer and thyristor valves [16]. However, thyristor-based HVDC has a major economic drawback of large ac-filter banks. Even for capacitor commutated converter, filters rated up to 0.24 pu are still required [17]. In addition, it is very challenging for thyristor-based HVDC to satisfy the increasingly stringent grid codes of offshore wind farm connection and on fault ride through. As a result, for offshore wind power transmission, VSC is favoured over LCC or CCC because of better controllability and no reactive compensation needed at the terminals [18]. Although many researchers are working on it, one constraint of HVDC nowadays is the DC circuit breaker, which is tricky to design and costly to manufacture, making it troublesome for DC fault clearance and grid forming of HVDC [19].

Fractional frequency transmission, sometimes known by the name Low Frequency AC Transmission, was proposed in [20]. It uses a fraction of the grid frequency, mostly one third, for the low frequency AC system. For the application of offshore wind power, it enjoys the merit of no offshore converter station. In addition, the gearbox ratio or number of poles of generator can be reduced, leading to a simpler and lighter design of the wind turbine. The onshore converter station needs an AC/AC converter to triple the frequency back to the network frequency for grid integration. And the detailed operating principle and control strategy will be discussed in Chapter 3.

Table 1.2 concludes the main pros and cons of the technologies discussed above. The trend of offshore wind development is to push wind farms further offshore. But it is preferred not to locate the offshore site too remote due to maintenance inconvenience and economic considerations. Also the scale of the offshore wind farms is expected to grow larger and offshore grids are expected to be built which has merits of improving reliability and shared

infrastructure etc. Having strengths at medium distance transmission and the ability to form grids easily, FFT is competitive for offshore wind power transmission.

Table 1.2 Summary of transmission technologies: advantages and disadvantages

Technology	Advantages	Disadvantages
High voltage AC transmission	• Mature and easy to implement	• High charging current • Normally < 100 km
High voltage DC transmission	• Suitable for point to point long distance transmission • Isolation of two AC systems	• DC circuit breaker limits grid forming and fault ride through
Fractional frequency transmission	• Low charging current, • Can simplify wind turbine design • Easy to form grids	• Bulkier offshore transformer

1.1.3 Introduction of Modular Multilevel Matrix Converter

The core device of the FFT system (FFTS) is the frequency changer, which acts as an interface between the fractional frequency system and the network system. The performance of the FFTS is largely determined by the frequency changer. Before insulated-gate bipolar transistor (IGBT) devices got popular, the thyristor based device cycloconverter used to be adopted during early-stage research [21, 22]. It is an AC/AC converter which has been used for motor driving purposes. Nevertheless, later research proved that it was not suitable for offshore wind power applications because of the shortcomings of unsatisfactory controllability, heavy harmonics and poor capability for fault ride through [23]. Contrarily,

M^3C shows strengths in this area. It was first introduced in [24] in 2001. There are nine arms connecting the three phases of the first AC system to the three phases of the second system. Fig. 1.3 is a simplified schematic diagram of M^3C connecting two AC systems. Note that the current direction is only for illustrative purpose as M^3C is capable of bidirectional operation with the adoption of full bridge sub-modules. It is evolved from matrix converter, so the topology is similar, which is a three-by-three matrix. However, each arm of the M^3C is form of a number of IGBT-based full bridge sub-modules and an arm reactor. To give more contexts, a photo of sub-modules forming a multilevel converter [25] and a photo of IGBT module [26] are provided as Fig. 1.4 and Fig. 1.5.

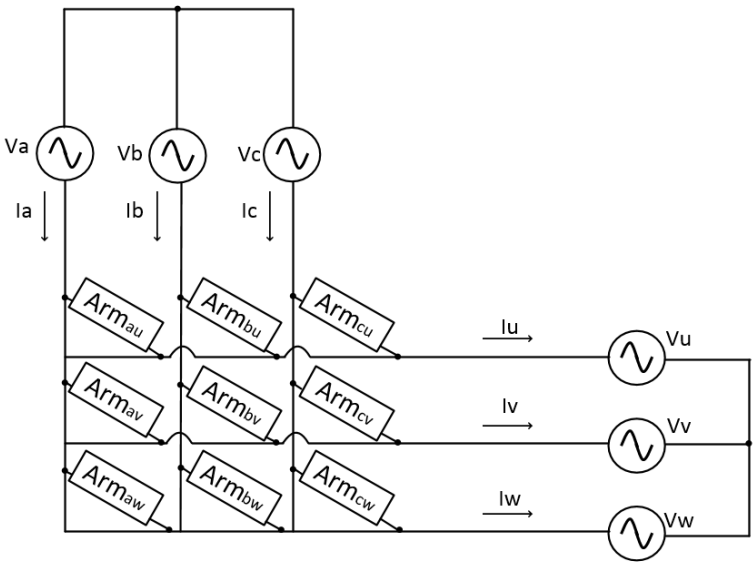

Fig. 1.3 A simple schematic diagram of M^3C connecting two AC systems.

M^3C is considered as the future AC/AC converter for high voltage and high power applications. Hence, it is particularly suitable for offshore wind power transmission. It is attractive with the advantages of low harmonic level and switching loss, flexible scalability and controllable power factor [27]. A more detailed review of M^3C will be given in the next chapter.

Fig. 1.4 A photo of sub-modules forming a multilevel converter [25].

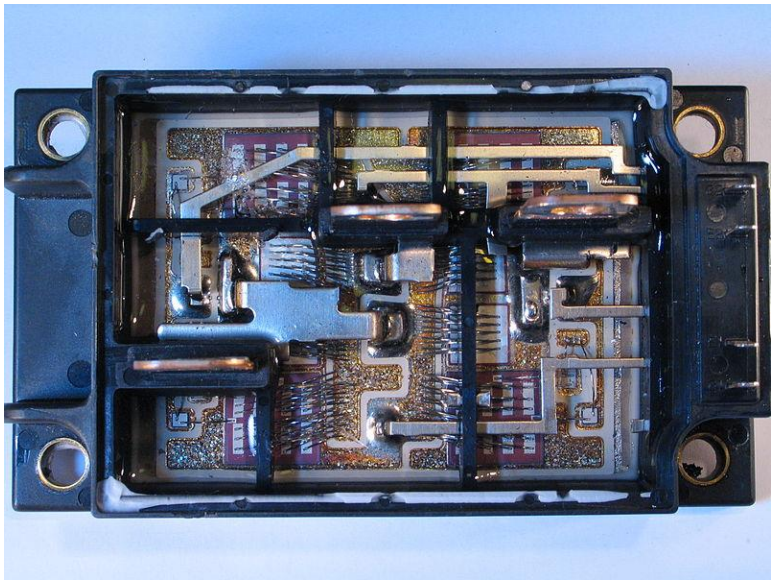

Fig. 1.5 A photo of IGBT module with four IGBTs (half of H-bridge) [26].

1.1.4 Research Motivations

It is a widespread consensus around the world to develop renewable energy to meet the challenge of fossil fuel depletion and environmental crisis. Among various types of renewable sources, offshore wind power is popular because of rich resource and the suitability for large-

scale development as it is away from population centre. Offshore wind farm projects are booming in Europe and it is anticipated that there will be a huge demand of offshore wind power integration in the developing areas in the future. As has been discussed, M^3C FFT has advantages over other kinds of transmission technologies. However, unlike HVDC which has been a popular research topic, the relatively new technology M^3C FFT has not received enough attention in the literature yet. Hence, to start with, Chapter 3 aims at giving a detailed introduction of the configuration, operating principle and the control strategy of M^3C. An overall picture is presented and the knowledge and the test system lay a foundation for following chapters.

With multiple technical advantages, M^3C FFT is a promising solution for offshore wind power transmission. However, the offshore wind industry is very cost-driven. The adoption of a technology largely relies on its economic capability. Although a number of researches can be found in the literature about M^3C control methods, the economic aspect of M^3C FFT is still not clear. Consequently, it is necessary to carry out a detailed cost analysis of M^3C FFT. This part of work is presented in Chapter 4.

After the economic strength of M^3C FFT is identified, the attention is paid to the technical aspect of M^3C. M^3C is the key component of the FFTS and it is broadly considered as the future AC/AC converter for high voltage and high power applications. However, a small signal model of M^3C is not yet available in the literature, making the system stability study difficult. Therefore, the doctoral study looks at developing a small signal model of the M^3C, which provides simple interfaces with the external AC systems on both sides and also the control system of the M^3C. After the model is developed, it is important to conduct small signal stability analysis to investigate the influences of the controller parameters and the

circuit elements. Guidelines are given on controller and circuit parameters selection. Chapter 5 covers the small signal modelling and analysis of M^3C.

Due to the lack of a DC link, electrical quantities at different frequencies from two AC systems couple in M^3C, resulting in a complex harmonic condition. With the interaction between the arm current and the switching function, capacitor voltage ripple is induced in the sub-modules. Harmonic currents of the M^3C have different frequencies and their behaviours are different. In addition, harmonics can lead to stability issues and adversely affect system components and therefore its analysis is of great importance. Nevertheless, a harmonic analysis of M^3C cannot be found in the literature yet to the best knowledge of the author. Motivated by the significance and the great need of the harmonic analysis, Chapter 6 carries out a detailed harmonic analysis of the M^3C focusing on its generation, influence and quantification. Effective measures are also proposed to mitigate M^3C harmonics.

1.2 Research Objectives and Contributions

1.2.1 Research Objectives

The objectives of the doctoral study are to:

• Provide knowledge on M^3C structure, operating principle and control method, and develop a test system for EMT simulation study to validate its performance as an AC/AC converter.

• Develop a cost analysis model of M^3C FFT for offshore wind power transmission, to study prominent cost components and determine economical transmission distance compared to the multilevel HVDC counterpart.

• Develop a small signal model of M^3C for offshore wind power transmission, which is easy to implement, helpful on controller parameters and sub-module capacitance selections and also beneficial to system stability study.

• Carry out a harmonic analysis of M^3C for FFT providing mathematical analysis, affecting factors and influences discussion, and harmonic mitigation solutions, which is beneficial to device modelling and control method development.

1.2.2 Research Contributions

The contributions of the doctoral thesis are summarised as follows:

• A novel cost analysis model is developed to investigate the economic aspects of M^3C FFT. Both capital cost and long-term costs are considered and an economic comparison between MMC HVDC and M^3C FFT are provided with sensitivity analysis.

• To fill in the gap of the literature, a small signal model of the M^3C is developed followed by a small signal analysis. The influences of the controller parameters and component values on small signal stability are analysed.

• A harmonic analysis method for M^3C is proposed. The unclear harmonic condition for M^3C is revealed from generation to influences. Also, the harmonic components are classified, quantified and can be mitigated by the proposed component selection guidelines and zero-sequence current mitigation controller.

1.3 Outline

Chapter 2 is a literature review of the research. Offshore wind power systems are reviewed focusing on the economic aspect. The fundamentals of small signal study are given together

with current studies on small signal modelling of multilevel converters. M^3C is discussed in terms of its applications and existing control methods.

Chapter 3 thoroughly discusses the operating principle and the control strategy of the M^3C. Control strategy is discussed hierarchically in terms of sub-module level, arm level and converter level. A test system of M^3C is developed for time domain simulations and it validates the performance of the M^3C and its controllers.

Chapter 4 studies the cost analysis and comparison between MMC and M^3C for offshore wind power application. The total cost decomposition of an offshore wind power system is discussed and the prominent components are highlighted. Cost comparison and economical breakeven distance are discussed through case studies. Sensitivity analysis is carried out to investigate the impact of parameter changes on the cost analysis.

Chapter 5 proposes a small signal model of M^3C for FFT. Interaction between the arm current and the switching function is first studied. Then the dynamics of AC currents, sub-module capacitor voltage with DC and ripple components and the control system are considered and included in the small signal model. Small signal analysis is carried out to study the impact of controller parameters and sub-module capacitance on the small signal stability of the M^3C FFT system.

Chapter 6 provides a detailed harmonic analysis of the M^3C. Analytical formulas are derived and arm current harmonics at different frequencies are classified and discussed. Factors that have large impact on harmonics are presented. The influences of each type of the harmonic components on the converter and the external AC systems are analysed in a detailed manner. Suppression methods of M^3C harmonics are proposed, including a proper selection of elements values and a zero-sequence current mitigation controller.

Chapter 7 gives a conclusion of the thesis. The outcomes of the research are summarised and the possible future work is proposed.

The chapters of this thesis are internally related. Literature review in Chapter 2 introduces the background and provides fundamental knowledge of the research. Chapter 3 presents the operating principle as well as the control strategy of M^3C, laying a foundation for the following chapters. On the economic side, Chapter 4 focuses on the cost analysis of M^3C. While on the technical side, Chapter 5 proposes a small signal model of M^3C and conduct stability analysis, and Chapter 6 investigates the harmonic aspect of M^3C and presents mitigation solutions. Overall, the thesis aims to provide a comprehensive profile of the novel AC/AC converter M^3C for offshore wind power application.

CHAPTER 2 LITERATURE REVIEW

2.1 Introduction

In this chapter, a literature review of the relevant subjects of the research is presented. Firstly, relevant previous studies on economic analysis of offshore wind power systems are reviewed and common analysis methods are discussed. Secondly, background knowledge of small signal analysis and various modelling approaches of converters are presented in preparation for the small signal modelling work in Chapter 5. Finally, relevant papers of M^3C in the literature are reviewed on topics of its applications and various control strategies.

2.2 Economic Analysis of Offshore Wind Power Systems

A number of economic analyses of offshore wind power are available in the literature already, focusing on different purposes. The International Renewable Energy Agency (IRENA) publishes reports on offshore wind power generation cost [28]. It aims to provide more transparent cost data to the public domain so that researchers, stake holders and key decision makers can have a clear view of the actual costs of renewable energy today. [28] collected and showed the global capacity factors for wind power, which had increased by 56% for the past three decades. Based on the analysis of the commissioned wind projects in 12 countries including the US, Denmark, Germany, UK and China, it predicted that the cost for offshore wind power had a reducing trend in the future due to three main drivers: advanced technology innovation, competitive procurement and increasingly mature project management experience. [29] reviewed available cost data in bibliography of offshore wind farm components, including wind turbine, cables, substations etc. They were helpful for

profitability studies or optimal economic analysis. But for some components, a regression curve was estimated from available empirical data and what technology was adopted was not taken into consideration.

Also, there are papers investigating the economic impact of combining different technologies with wind power systems. [30] carried out a cost-benefit analysis of using energy storage in wind power connection in Dutch power system. An economic despatch model was used taking account of CO_2 savings for three types of large-scale energy storage methods. It was found that energy storage was more effective on saving the operation cost when the wind farm capacity was large. However, the significant investment cost made the installed energy storage unit very difficult to breakeven and therefore a more cost-effective energy storage technology was expected to make the scenario more attractive. When the penetration level of wind power is high, the fluctuation of wind power may lead to a situation that wind power output is greater than the load or the transmission capability. An idea has been proposed to cope with such a problem, which is to utilize the wind power to produce hydrogen. In [31], an economic analysis of hydrogen production was presented in the microgrid context. According to the case study it was calculated that the cost of hydrogen was 17.65 $/kg and the payback period of the infrastructure was around 15 years. The results were greatly depended on the initial infrastructure investment, the wind power selling price and the hydrogen selling price. Hence, the conclusion may vary when price data change but the feasibility should increase with the technology development. [32] investigated the cost effectiveness of wind power for hydrogen production. The cost of hydrogen was calculated in different scenarios and it was found that the nominal power of the hydrogen production equipment played an important role in the cost analysis. When the nominal power was too small, energy storage system might be required to store the excessive wind power, making the price uncompetitive. When the

nominal power was too large, the utilization factor of the equipment might be poor depending on the actual wind power profile.

Besides, there are papers investigating the opportunity of combining multiple kinds of renewable energy. An optimal cost analysis was presented in [33] considering a wind-solar system for irrigation application. Wind power and solar power can sometimes be complementary and a hybrid renewable system can help the situation when no solar power can be produced at night or in a cloudy day or the situation when there is sufficient sunlight but very low wind speed. The total net present cost was set to be the objective function and the configuration of wind-solar capacities was optimised. Apart from solar, a wind-wave hybrid system was studied in [34]. Offshore wind and waves have great energy potential among the renewables and in the European coasts alone, 350 GW wind power and 320 GW wave power are available. Economic study showed offshore wind and wave power had plenty of synergies and there would be huge saving from combined wind-wave systems [35]. Grid integration infrastructure could be shared as well as the operation and maintenance. The hybrid system could also have common substructures or foundations.

In [36], a comparative economic analysis was carried out to achieve a certain nominal wind power generation. Three alternatives were: twenty low power (5 kW) turbines, five medium power (20 kW) turbines and one high power (100 kW) turbine. Result showed that the high power turbine was the optimal choice in terms of emission and life cycle electricity price of 25 years. The global warming impact was calculated to be 17.8 gCO_2/kWh, which was about 60% and 30% less than the medium and the low power turbine. The wind electricity price was 0.21 $/kWh which was the cheapest among the three choices. The conclusion agreed with the development trend of wind turbine in the industry, where single large volume high power turbine was preferred. [37] presented a benefit evaluation of wind generators. The purpose

was to select suitable capacity and hub height for commercial wind generators to maximise economic benefits. Weibull and Rayleigh distribution functions were used to model wind power density. Four commonly used methods for economic analysis were discussed, and the key points were concluded in Table 2.1.

Table 2.1 A brief summary of different economic-analysis methods

Economic-analysis methods	**Characteristics**
Payback period method	• Determine the time (often in years) required to recoup the initial investment • Calculated by the capital cost divided by the average annual profit
Cost of energy method	• Determine the cost to generate one unit of energy • From a generating perspective and often compared to other energy sources
Discounted cash flow method	• Determine the present value of money paid or received in the future • Emphasise the time value of money
Life cycle costing method	• Determine the most cost-effective candidate among all choices that are technically suitable • Include initial investments and all future costs, also consider time value of money

In [38], the authors applied an index ‘Energy Return on Investment’ to global available wind energy study. With high economic constraint as the energy return index > 10, it was found that several countries’ wind resource potentials were lower than previously established and were below what are needed to achieve 100% renewable energy target. A comprehensive review of techno-economic analysis methods for hybrid renewable energy system was provided in [39]. 31 computer tools and 20 arithmetical models were discussed and compared, giving useful references for researchers. Apart from introducing useful cost analysis methods, [36, 37] also pointed out that there were several salient differences between onshore wind farms and offshore wind farms regarding economic analysis. In 2017, many onshore wind projects commissioned had fallen within the price range of fossil fuel electricity [40], but offshore wind still has a relatively high cost of energy. Compared with onshore wind, offshore harsh marine environment leads to more complicated planning, construction, installation and maintenance. All these factors result in higher wind farm costs. Besides, due to the remote location, projects also have higher grid connection costs. For offshore wind power transmission, technical difficulties urge the use of more advanced technologies, and undoubtedly their costs would affect the economic analysis.

According to [41], the average capacity of offshore wind projects commissioned in 2016 was 380 MW and the average transmission distance to land was about 45 km. Such distance is still within the feasible range of HVAC transmission but future offshore wind farms will inevitably move further offshore. For long distance transmission, HVDC (usually refers to VSC HVDC when it comes to offshore transmission applications) is a popular option with various technical advantages. In the economic aspect, [42] presented a cost appraisal of HVDC in comparison to HVAC for offshore wind integration in Great Britain. The reactive compensation requirement was computed for wind farms with various capacities and

distances according to the UK Grid Code. As VSC HVDC does not have reactive power requirement, it was shown that the cost of reactive compensation equipment was a main shortcoming of HVAC. It was pointed out that capital and loss costs played a key role in the comparison. For HVDC, the capital cost was significantly higher mainly due to the expensive offshore converter station, while HVAC had larger energy loss especially at a long distance. Based on the specific case study it was calculated that the crossover distance between two technologies was between 120 km and 160 km for a 1 GW offshore wind farm. Another research [18] also focused on HVDC connection of offshore wind farms. The economic analysis was more detailed in terms of methodology taking into account the initial expenditure, operation and maintenance (O&M) and the energy not supplied cost. Analyses were carried out on transmission distance, DC converter reliability and converter losses. Case study showed that HVDC could be the cheaper option when capacity was 100 MW and transmission distance was longer than 90 km. However, the AC transmission method was limited to only two voltage levels: 150 kV and 400 kV. And the maximum capacity of the wind farm considered was 500 MW, which was insufficient for large-scale offshore wind farms in the future.

In terms of FFT for offshore wind power transmission, some but not enough attention has been paid to the economic analysis. An economic comparison was given in [43] between FFT, HVAC and HVDC in order to identify the most cost-efficient technology under different power capacities and transmission distances. An improvement was that AC transmission was considered in 132 kV, 220 kV and 400 kV and a non-linear and discontinuous cost function was yielded. However, the AC/AC converter station cost was estimated from a Line Commutated Converter HVDC station, which was too simple and could be inaccurate. And no detailed information was given on cost modelling of the AC/AC converter station, such as

O&M and loss costs. [44] presented an economic analysis of FFT and HVDC considering capital cost, power loss, and reliability. It was shown that FFT was the economical choice for wind farm with a capacity of 200 MW at 100 km. Nevertheless, the AC/AC converter considered in this paper was cycloconverter. It has heavy harmonics and poor controllability as discussed in Section 1.13 and it is not likely to be used for offshore wind power transmission. Also, costs for the filters and reactive power compensation were not included, which brought discrepancies to the results.

To conclude, some cost analyses of offshore wind power systems exist in the literature, and they focus on different aspects, such as providing useful data, investigating the impact of different technologies on offshore wind power, combining multiple renewable sources, determining transmission methods under different circumstances etc. Some cost-analysis methods are commonly used in the literature. Payback period method was used when breakeven time period was a concern before implementing a project. For instance, the decision makers would want to know how long it would take to recoup the investment back when installing energy storage or hydrogen production equipment to assist offshore wind farm. Cost of energy method is popular when carrying out economic analysis of different types of renewable energies and comparing their costs, pros and cons and future trend. Discounted cash flow method is often seen in accounting context. It emphasises the time value of money and represents the preference of companies that a payment is preferred to be made in the future rather than today, and an income is preferred to be received today rather than future. If the time value is considered in the cost of energy method, sometimes an improved version calculating levelized cost of energy (LCOE) is adopted in the literature. If several technologies can satisfy the same need in the technical aspect and the most cost-effective option needs to be identified, life cycle costing method would be adopted. After the

review, it is found that economic analysis is of significance in the offshore wind power industry. Some technologies may have great performance, excellent controllability or promising potential to help power systems during fault conditions. However, if they are not economical, or at least they are not economical enough nowadays, it would not be very likely that the technologies would be implemented into reality. Therefore, FFT as a relatively new technology is in great need of a thorough economic analysis. Data are necessary from reliable data sources, and they should be converted to the same common reference. The cost of the M^3C needs to be precisely modelled, and then substituted into a suitable economic-analysis method. These issues will be taken care of in Chapter 4.

2.3 Fundamentals of Small Signal Analysis and Multilevel Converter Modelling

2.3.1 Fundamentals of Small Signal Analysis

A power system or any dynamic system can be represented by a state space model which is formed of a number of nonlinear differential equations:

$$\dot{x} = Ax + Bu \tag{2.1}$$

where x is a set of state variables, u is a group of input variables and A and B are state matrix and control matrix respectively. The number of state variables is defined as the order of the system. As long as they can describe the system dynamics completely, state variables can be chosen in more than one way. The output of the system can be computed as:

$$y = Cx + Du \tag{2.2}$$

Outpurs are expressed as functions of the state variables and input variables. To carry out small signal analysis, the differential equations need to be linearized at equilibrium points. Those points can be got when all the derivatives are equal to zero, and they are referred to the initial state of the system. After linearization, Equations (2.1) and (2.2) become:

$$\begin{aligned} \Delta\dot{x} &= A\,\Delta x + B\,\Delta u \\ \Delta y &= C\,\Delta x + D\,\Delta u \end{aligned} \tag{2.3}$$

in which *A, B, C, D* are defined as the state matrix, control matrix, output matrix and feedforward matrix of the system [45]. Apply Laplace transform to the first line of (2.3), the characteristic equation of the matrix *A* can be calculated as:

$$\det(sI - A) = 0 \tag{2.4}$$

where the values of *s* satisfying (2.4) are the eigenvalues of the matrix. According to Lyapunov's theory, the system is small signal stable when all eigenvalues have negative real parts. When one or more eigenvalues have real parts with positive values, the system is small signal unstable. And when the real part equals to zero, the stability cannot be determined based on the criteria merely. In reality, a power system is always subjected to small disturbances, so it is important for the system to remain small signal stable. The small signal stability can be affected by the initial operating states and various controllers within the system [46]. Express the eigenvalues into real and imaginary parts:

$$\lambda = \sigma \pm j\omega \tag{2.5}$$

The real part determines the damping and the imaginary part indicates the oscillation frequency. A concept of damping ratio is defined to represent the rate of decay. These two characteristics can be expressed by (2.6) and (2.7). When the damping ratio is less than 5%,

the mode is regarded as poor damped and the system may be subjected to small signal instability.

$$f = \omega/2\pi \tag{2.6}$$

$$\xi = -\sigma/\sqrt{\sigma^2 + \omega^2} \tag{2.7}$$

2.3.2 Small Signal Modelling of Converters

Converters have been widely involved in power systems for different applications, for example Static Synchronous Compensator (AC/DC converter) [47], wind energy converter system (AC/DC/AC back-to-back converter) [48, 49], HVDC system (AC/DC/AC converter) [50], FFTS (AC/AC converter) [20] etc. A back-to-back converter was modelled in [51], the DC link was modelled by a capacitor and one order was used to considered the active power balance between the rectifier and the inverter. The converter was used in the doubly-fed induction generator (DFIG), a vector control was adopted for the rotor side converter to control the torque of the wind turbine and the DFIG side reactive power, and for the grid side converter, to control the DC link voltage and terminal reactive power. In [52], a feedback control strategy was designed according to small signal model for multilevel Static Synchronous Compensator. The purpose of the controller was to balance the capacitor voltages between individual sub-modules. Nevertheless, neither capacitor voltage ripple nor circulating current was considered in the small signal model. [21] proposed a small signal model of an FFTS with cycloconverter. It was found that the cycloconverter had a negative effect on the damping of the system. A simple feedback PI controller was added to overcome the insufficient damping problem. However, the key component AC/AC converter was simply modelled as a first order time delay, so the detailed dynamics of the semiconductor switches

were neglected and the potential interaction between the converter and the connected AC systems could not be studied. A VSC based HVDC was modelled in [53] to study the influence of HVDC on power system small signal stability. The topology was a single machine infinite bus system equipped with a HVDC. The eigenvalue analysis showed that the open loop system was unstable and a damping controller was designed using the speed deviation as the control input. The performance of the controller was examined by both small signal analysis and time domain simulation. However, the decoupling control of HVDC is so commonly used that it should be included in the small signal model or the designed controller should also be compared with the decoupling control to examine its performance.

Furthermore, some work has been available on MMC HVDC in terms of small signal modelling. [54] pointed out that when the internal dynamics of the MMC was neglected, its small signal model was similar to VSC configurations with two or three levels. Such average model facilitated large power system studies but it was based on the assumption that the internal damping of MMC was enough. [55] improved the small signal model of MMC by including the internal energy dynamics. It considered the DC component of the internal circulating current but it assumed that the energy unbalance controller could ensure zero fundamental frequency circulating current at steady state and it had no influence on the dynamics of the rest of the system. In fact, when the system experienced small disturbances, circulating current and arm energy were coupled so the influence of the circulating current controller needed to be considered. Such issue was resolved by [56], where the authors modelled the second order circulating current and the circulating current suppression control. The model also included the capacitor voltage oscillation at double system frequency in DQ frame. For multilevel converter such as MMC, there are a great number of sub-modules and each sub-module capacitor can be one order in the detailed model. However, the sub-module

number can get to several hundred so it is not mathematically efficient to consider all the dynamics within a single sub-module. The small signal model should be consisted of a reasonable number of state variables meanwhile maintaining sufficient accuracy.

After the review, it can be found that different kinds of converters have some common ground when it comes to small signal modelling. For the AC/AC converter M^3C, the average DC voltage of the capacitors needs to be maintained. But the situation is more complex as there are nine arms in an M^3C and each arm contains multiple sub-modules. MMC has capacitor voltage oscillations at double system frequency. But the capacitor voltage ripple of the M^3C is different from that in MMC and it is determined by the AC system frequencies from both sides. MMC and M^3C share some similarities as they are both multilevel converters. However, the operation of the M^3C is fundamentally different from its AC/DC/AC counterpart. In a MMC HVDC system, both sides are isolated by the DC link so two systems can be regarded as no coupling. In modelling, many papers only consider one side (either rectifier or inverter) due to symmetric reason. However there is no DC link in the M^3C, and as a result of which, quantities from two AC systems at different frequencies couple together in the converter. This situation is unique and therefore it is of significance to develop a small signal model of M^3C to understand its dynamics and its impact on the power systems.

2.4 Control and Applications of Modular Multilevel Matrix Converter

The concept of M^3C was first introduced in 2001 [24]. The authors presented a matrix configuration of nine switches that had four-quadrant operation ability. The configuration resembled the traditional matrix converter except that matrix converter contained only

switches to determine the on or off of the both side it connected, while M^3C adopted IGBT based full bridge sub-modules. Each sub-module could produce three voltage levels during operation. It was proposed that the input and output voltages could be controlled by space vector modulation (SVM) and simulation result was presented based on a M^3C with two sub-modules in each arm.

After that M^3C has been proposed for various applications, mainly in wind power integration [57, 58] and motor driving [59, 60], and sometimes in power quality enhancement as a unified power quality conditioner (UPQC) [61]. In the future, it is possible that M^3C could be used in the transport sector, for example in railway systems [62]. As railway has experience in running the system at fractional frequency. And with the bidirectional ability of the full bridge sub-modules and the good controllability of M^3C, it is likely that the regenerative braking energy could be increased and well-managed for railway vehicles [63]. In [64], a decoupled current control method of M^3C was presented for medium voltage motor drives with regenerative braking. The control method was able to regulate the output torque and balance the DC average capacitor voltage. A three-phase 400 V, 15 kW experiment system was developed to verify the performance. [60] focused on optimising the phase reactor of the M^3C to reduce its size and weight. The reactor was necessary for the current control of the M^3C. A zigzag winding was implemented to achieve that no magnetic flux was introduced in any of the nine arms by the three-phase supply or the motor currents. The effectiveness was proven by experimental results in a downscaled motor drive system. For offshore wind transmission, different from motor driving applications, the sub-module number is high to reach a high voltage rating, and the frequencies on both AC sides are controlled to be constant. This research focuses on offshore wind FFTS application.

In [65], a SVM based control was used on M^3C to realise wide frequency range operation. Simulation and experiments showed that the M^3C could stably operate without additional circulating current control under different conditions, including low frequency conversion and identical frequency conversion. However, the evaluated M^3C only had three sub-modules in each arm. In addition, SVM is not recommended to be used at high voltage level since the increasing number of sub-modules induces an exponential growth of the space vectors, making it time-consuming to compute and difficult to analyse. A widely used control method was developed in [66]. A concept of double $abc - \alpha\beta 0$ transformation was used to realise fully decoupled current control. But some variables after two transformations were not DC components even at steady state but with a mixture of frequency components, which was not good for controller design or small signal modelling. In [67], this method was further improved for FFTS by introducing the cross synchronous rotating frames, so that DC values are dealt with at most time in current loops. But the control method was complicated to be implemented with a number of transformations and controllers. When the sub-module level of M^3C increases, the total number of the sub-modules in all nine arms can be significant and therefore impose a challenge to control communication network and centralised control structure. In [68], a distributed control architecture for M^3C was proposed, featuring in a time-dimension decoupling strategy which separates the fast current control loop and the slow voltage control loop to reduce communication data. Good performance on both steady state and dynamic operation was verified by experimental results on an M^3C prototype with eased communication burden.

Plenty of researches have been carried out to improve the performance of M^3C in different aspects. As IGBT semiconductor is limited mainly by its current rating capability, [69] introduced a control strategy to damp the peak arm current of the M^3C by 14.6% to 21.6%,

giving potential for reducing cost and the converter footprint. In order to save components and reduce the number of switching, [70] worked on an alternative AC/AC multilevel converter topology. It was validated by simulation and experimental results that the sparse topology could also help on circulating current suppression. Authors from [71] looked into M^3C under fault conditions, featuring in an optimised branch current control when one or more arms of the M^3C were lost during faults. A nonlinear optimisation model was developed to optimise the branch current structure after the branch fault. Experimental results showed that the M^3C could convert from full arms to a reduced topology without shutting down the whole converter. In some other applications besides offshore wind power integration, M^3C may be required to operate at a frequency ratio near one, which is known as challenging with large voltage oscillations on capacitors. A vector control of M^3C was proposed in [72] aiming at operating it over a wider range of frequencies. With delicate transformation, filtering and energy balancing among arms, it was tested by a downscaled laboratory prototype that the M^3C was able to function well even when the input frequency is close to output frequency. The downside of this method is extra component rating for common mode voltage and circulating currents. In [57], the operation of M^3C under unbalanced grid conditions was investigated. A feedforward control strategy was proposed to compensate the imbalanced energy between arms induced by negative-sequence quantities. Simulation results showed that with the proposed control method, M^3C could cope with unbalanced grid conditions caused by single phase faults. With an increasing penetration level of offshore wind power, frequency support becomes a crucial issue for offshore wind farms in compliance with grid code. [73] investigated a frequency support control of M^3C to cope with frequency drop conditions. However, since the energy used is from the floating capacitors, the frequency support capability is limited.

Based on the review it was found that plenty of research work has been carried out on M^3C control method development. However, harmonic analysis of M^3C was rarely seen in the literature. Based on the ideal assumption that only components at AC system frequencies existed in the arm current, paper [74] derived the current expression of sub-module capacitance of M^3C. But the attention was paid to the sub-module capacitance selection and harmonic analysis was not provided for the M^3C. Authors of [75] verified the performance of M^3C as the frequency changer in FFTS and provided an analysis. A mathematical model was presented on one sub-converter, but no discussion was given on the harmonics and the capacitor voltage ripples were not taken into consideration. From the stability point of view, harmonic analysis of M^3C is of significant importance for FFTS, as offshore wind power is often connected to weak AC systems which are prone to stability issues. Harmonic instability and resonance have been found in research and in reality when power electronic devices with high switching frequencies interact with other components in power systems [76, 77].

In the BorWin1 offshore wind farm in Germany, harmonic interaction occurred and was reported in [78]. The incident caused the whole HVDC system to shut down and wind energy could not be delivered to the grid. Except for preventing economic loss, harmonic analysis is also crucial to avoid device damage. Although MMC and M^3C are both multilevel converter and share some similarities, the harmonic situation of M^3C (AC/AC converter) is different from that of MMC (AC/DC/AC converter), due to fundamentally different operation principle and the lack of a DC link. In M^3C FFTS, quantities at two frequencies intertwine in the converter and interact with the switching devices, resulting in a complicated frequency profile. For MMC HVDC, it was found that the circulating currents were in even orders, mainly in second order [79]. The capacitor voltage was also in second order and in negative sequence for MMC and the harmonic current only circulated within the converter. But for M^3C, the

harmonic situation is still not clear and needs to be fully investigated, which is the main focus of Chapter 6.

CHAPTER 3 OPERATING PRINCIPLE AND CONTROL STRATEGY OF THE M^3C

3.1 Introduction

The aim of this chapter is to provide a detailed discussion on the configuration, operating principle and the control strategy of the M^3C. The control strategy is introduced hierarchically in terms of the sub-module level, arm level and converter level controls. A time domain simulation system is developed to validate the performance of the M^3C as an AC/AC converter. The knowledge presented in this chapter lays a foundation for the following chapters, particularly the small signal modelling of M^3C in Chapter 5 and the harmonic analysis of M^3C in Chapter 6.

3.2 Operating Principle of the M^3C for FFT

An offshore wind FFTS is shown in Fig. 3.1, where the grid frequency is set to be 60 Hz. The offshore wind generator produces power at 20 Hz, and the voltage is raised by the offshore step-up transformer before the power is transmitted at the fractional frequency to the onshore station. The M^3C station triples the frequency back to 60 Hz and the power is delivered into the main grid.

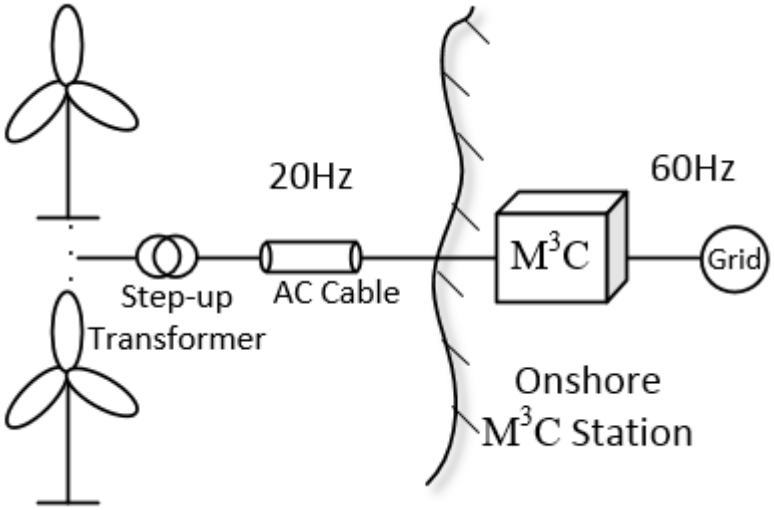

Fig. 3.1 Illustrative diagram of an offshore wind FFTS.

The schematic diagram of the M^3C is shown in Fig. 3.2. It is a three-phase to three-phase AC/AC converter with a total of nine arms. The subscripts *a, b, c* represent quantities at the generator side for voltage and current while subscripts *u, v, w* represent quantities at the system side. Voltage and current directions are shown in Fig. 3.2. In each of the nine arms, there are *N* IGBT based full bridge sub-modules and an arm reactor.

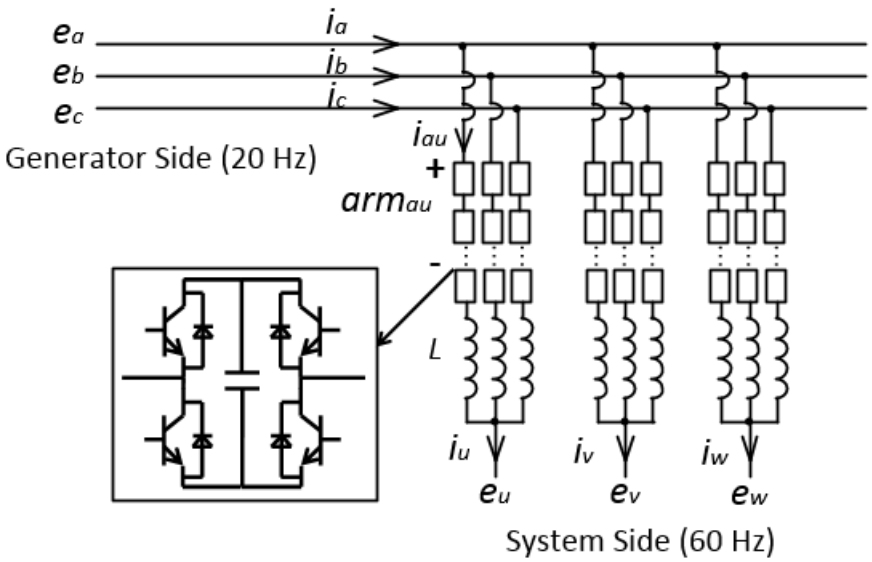

Fig. 3.2 Schematic diagram of a M^3C.

Quantities at the generator side frequency (20 Hz) and those at system side frequency (60 Hz) couple in the M^{3}C. At balanced steady state, AC side phase current spreads equally into three arms that are connected to it [75, 80]. Take arm current i_{au} for instance, it contains one third of the phase current i_a and one third of the phase current i_u. It can be mathematically expressed as:

$$i_{au} = I_a \sin(\omega_1 t + \beta_1) + I_u \sin(\omega_3 t + \beta_3) \quad (3.1)$$

where I_a, I_u ω_1, ω_3, β_1 *and* β_3 are the magnitudes (equal to one third of the AC system phase currents magnitudes), angular frequencies and phase angles of the 20 Hz and 60 Hz currents in the arm. Similarly, the arm switching function is formed of components at 20 Hz and 60 Hz and it can be given by Equation (3.2), where $\frac{E_a}{U_{DC}}$ and $\frac{E_u}{U_{DC}}$ are the modulation ratios at 20 Hz and 60 Hz. E_a, E_u, α_1 and α_3 are the magnitudes and phase angles of the modulation voltages. U_{DC} is the total arm DC voltage.

$$S_{au} = \frac{E_a}{U_{DC}} \sin(\omega_1 t + \alpha_1) + \frac{E_u}{U_{DC}} \sin(\omega_3 t + \alpha_3) \quad (3.2)$$

3.3 Control Method of the M^{3}C for FFT

This section discusses the control strategy of the M^{3}C adopted in this study, which is introduced at sub-module level, arm level and converter level. Operation modes of the full bridge sub-module are introduced first, followed by the arm level modulation strategy. Then the transformation technique and the decoupling control of the M^{3}C are presented.

3.3.1 Switching Modes of Full Bridge Sub-Module

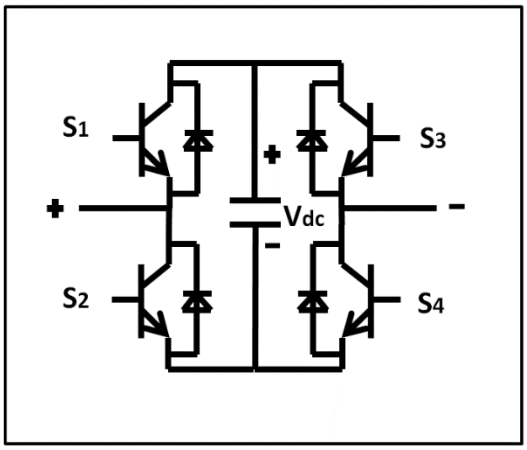

Fig. 3.3 Schematic diagram of a full bridge sub-module.

A schematic diagram of a full bridge sub-module is plotted in Fig. 3.3. In this topology, each sub-module consists of four switch units and a capacitor. And each switch unit has an IGBT and a freewheeling diode. The on and off combination of the switch units determines the operation mode of the sub-module. To be specific, when S_1 and S_4 are switched on and S_2 and S_3 are switched off, the capacitor is positively inserted. Similarly, when S_2 and S_3 are switched on and S_1 and S_4 are switched off, the capacitor is negatively inserted. The bypass mode can be implement by two ways: either switching on S_1 and S_3 or switching on S_2 and S_4. The sub-module would be in block mode if all the switch units are off but this is not the case at normal operation. The operation modes of the full bridge sub-module are summarised as Table 3.1. Each sub-module can output three voltage states: +Vdc, 0 V and –Vdc. When an arm is formed of *N* sub-modules, *2N+1* levels of output voltage are possible. As the terminal voltage can be regulated by the switching, M^3C is therefore a kind of voltage source converter.

Table 3.1 Full bridge sub-module operation modes

IGBT switches on	IGBT switches off	Sub-module output mode
S_1 and S_4	S_2 and S_3	+Vdc inserted
S_2 and S_3	S_1 and S_4	-Vdc inserted
S_1 and S_3	S_2 and S_4	Bypass
S_2 and S_4	S_1 and S_3	Bypass
N/A	S_1 to S_4	Block

3.3.2 Control Method at Arm Level

The output of the vector control is the voltage reference in DQ frame. After Park inverse transformation the voltage reference of each arm is ready for modulation. In this study the nearest level modulation (NLM) [81] is adopted to convert the voltage reference to the switching states of the sub-modules. Fig. 3.4 shows the control diagram of NLM taking arm *au* for example. The arm voltage reference v_{auref} is divided by the measured DC average capacitor voltage of the arm to determine how many sub-modules should be switched on. But the value after division should be approximated to the nearest integer level and limited by the maximum sub-module number. The output $NORD_{au}$ is the inserted sub-module number for arm *au*, where a negative value indicates that the sub-modules are negatively inserted.

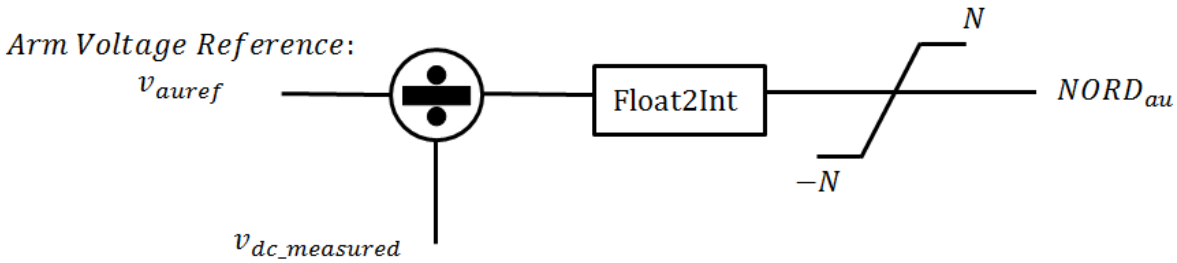

Fig. 3.4 Schematic diagram of NLM.

The voltage balancing technique of the sub-modules within an arm is the same as [79] and the principle is described as follows:

• If the arm current direction is to charge the sub-module capacitors, the sub-modules with the lowest capacitor voltages will be inserted first.

• If the arm current direction is to discharge the sub-module capacitors, the sub-modules with the highest capacitor voltages will be inserted first.

3.3.3 Control Method at Converter Level

One challenge of M^3C control is the mixture of two frequencies in the converter. In this subsection, it is illustrated that how components at 20 Hz and 60 Hz are extracted and the decoupling control is achieved for M^3C. The control objective is to use the D axis of the 20 Hz side to regulate transmitted active power and the D axis of the 60 Hz side to maintain capacitor voltage balance, and to regulate reactive power on both Q axes.

Based on Fig. 3.2, the Kirchhoff's law equations for the nine arms of the M^3C are expressed in the following equations, where an additional resistor R is added to represent the internal converter losses:

$$u_a = v_{au} + \left(R + L\frac{d}{dt}\right) \cdot i_{au} + u_u \tag{3.3}$$

$$u_a = v_{av} + \left(R + L\frac{d}{dt}\right) \cdot i_{av} + u_v \tag{3.4}$$

$$u_a = v_{aw} + \left(R + L\frac{d}{dt}\right) \cdot i_{aw} + u_w \tag{3.5}$$

$$u_b = v_{bu} + \left(R + L\frac{d}{dt}\right) \cdot i_{bu} + u_u \tag{3.6}$$

$$u_b = v_{bv} + \left(R + L\frac{d}{dt}\right) \cdot i_{bv} + u_v \tag{3.7}$$

$$u_b = v_{bw} + \left(R + L\frac{d}{dt}\right) \cdot i_{bw} + u_w \tag{3.8}$$

$$u_c = v_{cu} + \left(R + L\frac{d}{dt}\right) \cdot i_{cu} + u_u \tag{3.9}$$

$$u_c = v_{cv} + \left(R + L\frac{d}{dt}\right) \cdot i_{cv} + u_v \tag{3.10}$$

$$u_c = v_{cw} + \left(R + L\frac{d}{dt}\right) \cdot i_{cw} + u_w \tag{3.11}$$

v_{xy} and i_{xy} $(x = a, b, c;\ y = u, v, w)$ are referred to the arm voltage and arm current consisting of 20 Hz and 60 Hz components. Divide the above nine equations into three sets (3.3) – (3.5), (3.6) – (3.8) and (3.9) – (3.11), representing three clusters *a*, *b*, *c*. Apply $\mathrm{ABC} - \alpha\beta 0$ transformation to three sets of equations respectively. Considering that AC systems at both sides are balanced, the zero term of u_u, u_v and u_w does not exist, and the three equations can be expressed as:

$$u_a = v_{a0} + \left(R + L\frac{d}{dt}\right) \cdot i_{a0} \tag{3.12}$$

$$u_b = v_{b0} + \left(R + L\frac{d}{dt}\right) \cdot i_{b0} \tag{3.13}$$

$$u_c = v_{c0} + \left(R + L\frac{d}{dt}\right) \cdot i_{c0} \tag{3.14}$$

where v_{x0} and i_{x0} $(x = a, b, c)$ are the zero voltage and current components for cluster *a*, *b*, *c*. In (3.12) - (3.14), the 20 Hz components are decoupled from the 60 Hz ones. Apply $\mathrm{ABC} -$

DQ transformation to (3.12) - (3.14), the DQ components can be calculated and they can be used for the vector control on the 20 Hz side:

$$E_{d20} = U_{d20} - \left(R + L\frac{d}{dt}\right) \cdot I_{d20} + \omega_1 L I_{q20} \tag{3.15}$$

$$E_{q20} = U_{q20} - \left(R + L\frac{d}{dt}\right) \cdot I_{q20} - \omega_1 L I_{d20} \tag{3.16}$$

PI controllers can be applied and E_{d20} and E_{q20} are the output voltage references from the vector control. Similarly, the 60 Hz components can be decoupled using the same approach. Or after the first ABC − αβ0 transformation, apply αβ − DQ transformation to three sets of equations in alpha/beta frame. The following equations are derived for clusters *a, b, c* respectively:

$$U_{d60} = v_{ad} + \left(R + L\frac{d}{dt}\right) \cdot i_{ad} - \omega_3 L i_{aq} \tag{3.17}$$

$$U_{q60} = v_{aq} + \left(R + L\frac{d}{dt}\right) \cdot i_{aq} + \omega_3 L i_{ad} \tag{3.18}$$

$$U_{d60} = v_{bd} + \left(R + L\frac{d}{dt}\right) \cdot i_{bd} - \omega_3 L i_{bq} \tag{3.19}$$

$$U_{q60} = v_{bq} + \left(R + L\frac{d}{dt}\right) \cdot i_{bq} + \omega_3 L i_{bd} \tag{3.20}$$

$$U_{d60} = v_{cd} + \left(R + L\frac{d}{dt}\right) \cdot i_{cd} - \omega_3 L i_{cq} \tag{3.21}$$

$$U_{q60} = v_{cq} + \left(R + L\frac{d}{dt}\right) \cdot i_{cq} + \omega_3 L i_{cd} \tag{3.22}$$

At symmetrical state, three clusters are balanced [82] so V_{adq}, V_{bdq} and V_{cdq} can be uniformly denoted as E_{d60} and E_{q60} and i_{adq}, i_{bdq} and i_{cdq} can be uniformly denoted as I_{d60} and I_{q60}. Hence, the voltage relation on the 60 Hz side can be represented as:

$$E_{d60} = -U_{d60} - \left(R + L\frac{d}{dt}\right) \cdot I_{d60} + \omega_3 L I_{q60} \tag{3.23}$$

$$E_{q60} = -U_{q60} - \left(R + L\frac{d}{dt}\right) \cdot I_{q60} - \omega_3 L I_{d60} \tag{3.24}$$

Again PI controllers are applied to balance capacitor voltage for the 60 Hz side and E_{d60} and E_{q60} are the output voltage references from the vector control. The schematic diagram of the M^{3}C control strategy is plotted in Fig. 3.5 to visualise the control methods at sub-module level, arm level and converter level as discussed in this section.

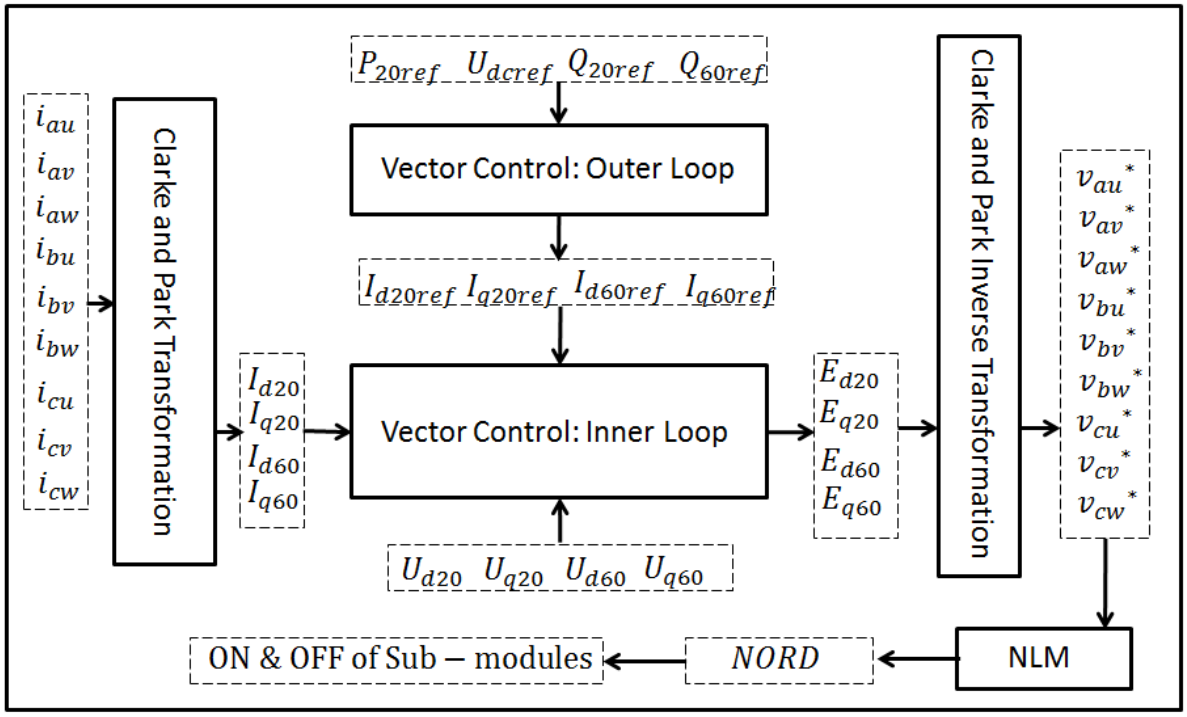

Fig. 3.5 Overall control diagram of the M^{3}C.

3.4 Simulation Results of the M^{3}C

To examine the control strategy discussed in the previous section, a detailed model of M^{3}C is developed in RTDS for EMT simulations. In terms of power system simulation software, some commonly-used tools include Matlab/Simulink, PowerFactory, PSCAD and RTDS.

They have similarities but each of the software has its advantages. Matlab/Simulink is able to perform power system simulations but it is not confined in power system application but also capable of a wide range of system simulations in engineering domain. It has strong flexibility as it can be supported by Matlab scripts and user-defined S functions. PowerFactory is specialised at load flow calculation, short circuit analysis and reliability study etc. PSCAD is well known by its suitability for simulating electromagnetic transient responses of power systems. It is also popular for controller design especially with power electronic components. The above three software can be installed and run on PCs. But as the system grows, or detailed behaviour of power electronics needs to be studied, the simulation speed of the abovementioned software can be relatively slow and therefore they could become inefficient. To cope with this issue, RTDS is an ideal tool as it provides real time digital simulations. The power system basic component models are similar between PSCAD and RTDS, where the main difference is that RTDS adopts additional hardware to accelerate simulations [83] while PSCAD largely relies on the computational capability of the PC. In this thesis, RTDS is adopted for M^3C EMT simulations due to its time-efficiency when the simulation system contains a large number of power electronic components.

The topology of the simulation system is as shown in Fig. 3.2 with the AC system modelled as a voltage source behind a Thevenin impedance. The power flow direction is from the 20 Hz side to the 60 Hz side. And each arm of the M^3C contains 40 sub-modules. Full details of the system parameters can be found in Appendix A. And a further explanation of the simulation model is given in Appendix B. The M^3C test system built in this chapter will further serve the small signal modelling in Chapter 5 and the harmonic analysis in Chapter 6. The tuning of controller parameters in Appendix A is subject to certain rules. Increasing the proportional gain has the effect of proportionally increasing the control output for the same level of input

error. Therefore, bigger proportional gain pushes the closed-loop system to react more quickly, and also help reduce but not eliminate steady state error. However, that would lead to a higher overshoot and push the poles of the system to the right half panel, which are unfavourable for system stability. The inclusion of the integral gain helps reduce steady state error. But for an integrator, when the error changes sign, it may take a while to cancel out the integration and change sign for the output, so it can slow the controller reaction. Integral controller is rarely used alone as it creates an open-loop pole on the original point and delays the output signal by 90 degrees, which is adverse for system stability. Sometimes a derivative term would be added to the controller. With this term, the control output could react when the error signal starts to ramp but the magnitude of the error is still small. It brings an open-loop zero to the system, and has not effect on steady state error. For the down side, it is very sensitive to system noise. In this thesis, PI controller is adopted.

3.4.1 Terminal Voltage and Current

In the time domain simulation, Fig. 3.6 (a) to Fig. 3.6 (d) show the sinusoidal voltage and current waveforms at the 20 Hz and 60 Hz AC sides respectively. As can be seen, voltage waveforms at both sides are ideal sinusoidal, while the current waveforms are sinusoidal but subjected to a slight distortion. The reason of the distortion will be discussed in Chapter 6 and solutions will be presented. Harmonics will be investigated in Chapter 6. Besides that, the control method performs well and two AC systems with different operating frequencies are able to be connected by the M^3C. The voltage and current profiles within the M^3C are analysed in the next subsection.

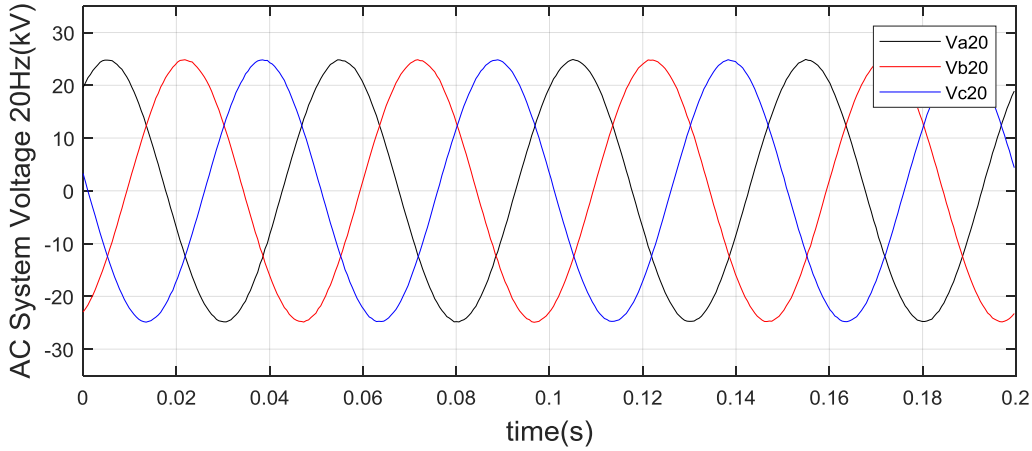

(a) 20 Hz AC side voltage.

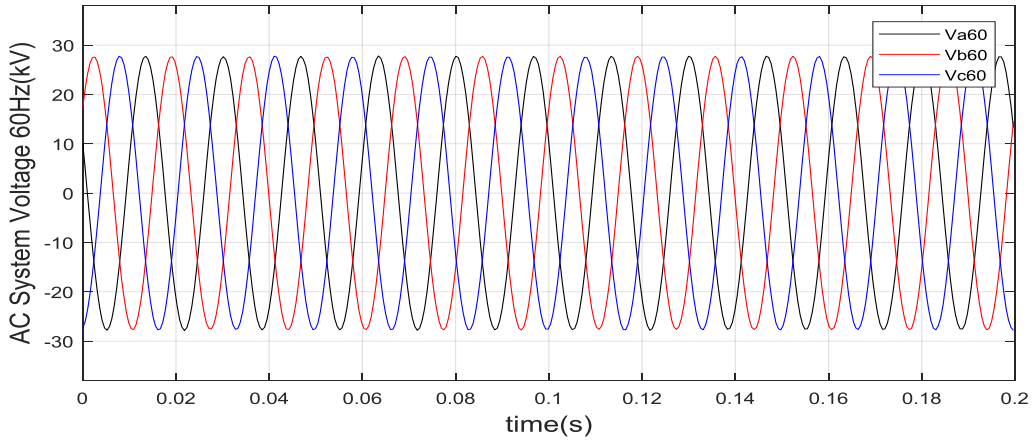

(b) 60 Hz AC side voltage.

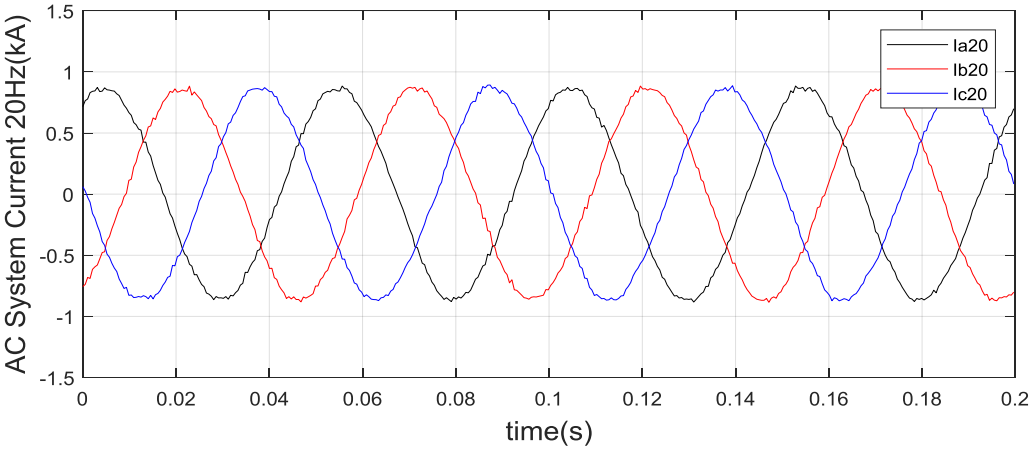

(c) 20 Hz AC side current.

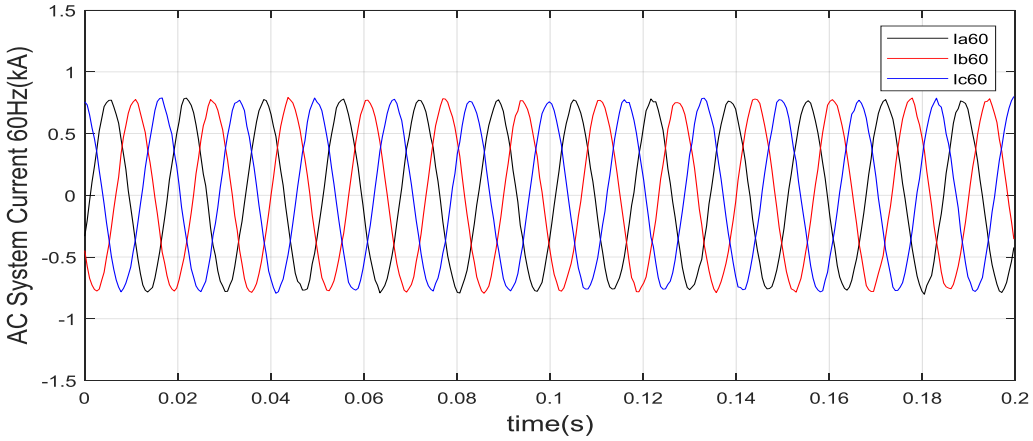

(d) 60 Hz AC side current.

Fig. 3.6 AC side voltage and current waveforms of M^3C.

3.4.2 Arm Voltage and Current

The original arm voltages and currents are shown in the subplots (a) from Fig. 3.7 to Fig. 3.10. To be specific, Fig. 3.7 (a) shows the arm voltages of arm *au*, *av*, *aw*, Fig. 3.8 (a) shows the arm voltages of arm *au*, *bu*, *cu*, Fig. 3.9 (a) shows the arm currents of arm *au*, *av*, *aw* and Fig. 3.10 (a) shows the arm current of arm *au*, *bu*, *cu*. As can be seen, they are waveforms with a superposition of 20 Hz and 60 Hz sinusoidal components. Subsection 3.3.3 discusses how the 20 Hz and the 60 Hz components are isolated from the arm quantities and it can be validated by the time domain simulation. For instance from equations set (3.3) – (3.11) to equations set (3.12) – (3.14), 20Hz components have been isolated. They are further transformed into DC values (at steady state) using DQ transformation, to Equations (3.15) and (3.16). On the 20 Hz side, take cluster *a* for example, applying ABC − αβ0 transformation to the arm voltages of arm *au*, *av*, *aw* and extract the zero component, v_{a0} only contains 20 Hz component. Similarly v_{b0} and v_{c0} are calculated and the three voltage variables that contain 20 Hz component are plotted in Fig. 3.7 (b). When ABC − DQ transformation is further applied, the three voltage variables are transformed into DQ components and it can be seen in Fig. 3.7 (c)

that the DQ components are DC values at steady state. Using the same approach, the DQ components of the arm currents are calculated and they are fed into the 20 Hz side vector controller. On the 60 Hz side, after the $ABC - \alpha\beta 0$ transformation is applied to the arm voltages of arm *au*, *av*, *aw*, the 60 Hz voltages are extracted as the alpha and beta components since the 20 Hz voltage only exists in the zero component. Therefore, it can be seen in Fig. 3.8 (b) that the alpha and beta components are sinusoidal waveforms at 60 Hz. Then $\alpha\beta - DQ$ transformation is applied to convert the alpha and beta components into DQ frame so that DC values are acquired for control purpose. The transformation of the arm currents is the same so it is not repeated again. However as the arm currents contain a small amount of harmonic components, the DQ components after transformation are not purely constant. A filter can be applied to the current signal to improve the controller performance. For instance in Fig. 3.10 (c), a first order low pass filter is applied with a time constant of 0.005s.

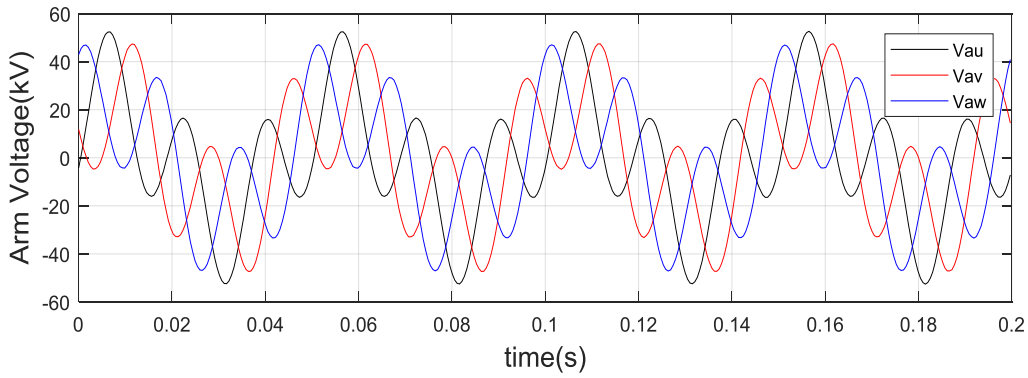

(a) M^3C arm voltages: arm *au*, *av*, *aw*.

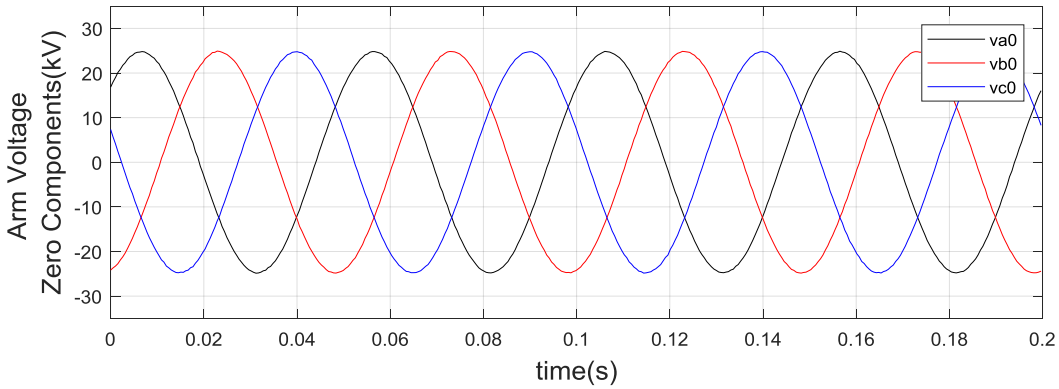

(b) Zero components (20 Hz) of M^3C arm voltage after ABC - αβ0 transformation.

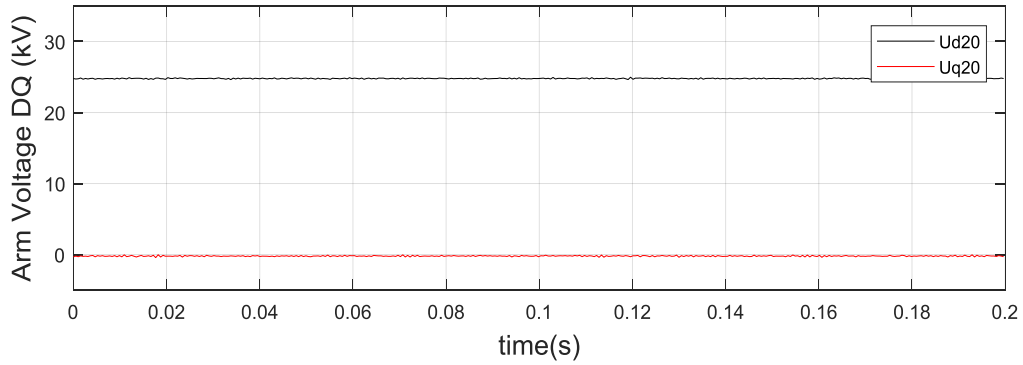

(c) DQ components of M^3C arm voltage after ABC - DQ transformation.

Fig. 3.7 M^3C arm voltages of the 20 Hz side and components after transformation.

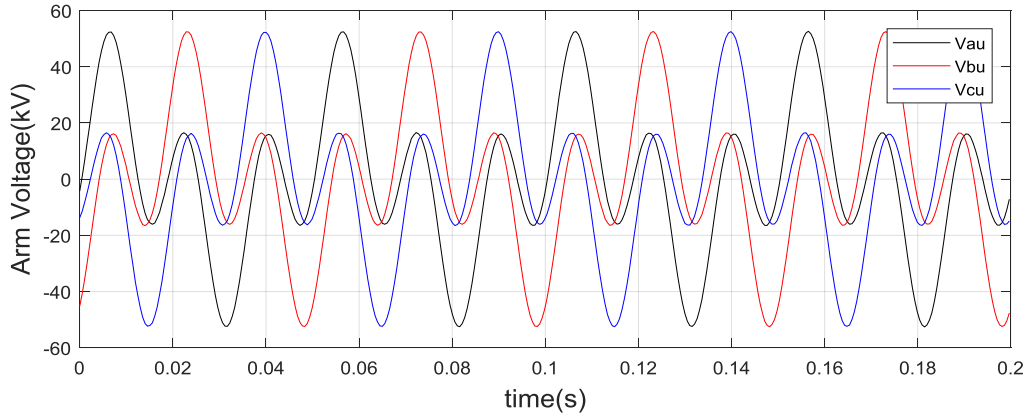

(a) M^3C arm voltages: arm *au*, *bu*, *cu*.

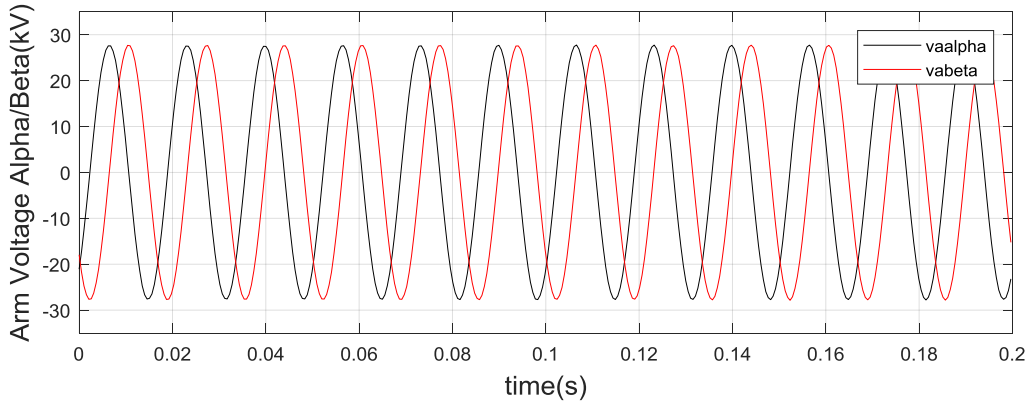

(b) Alpha and Beta components (60 Hz) of M^3C arm voltage after ABC- αβ0 transformation.

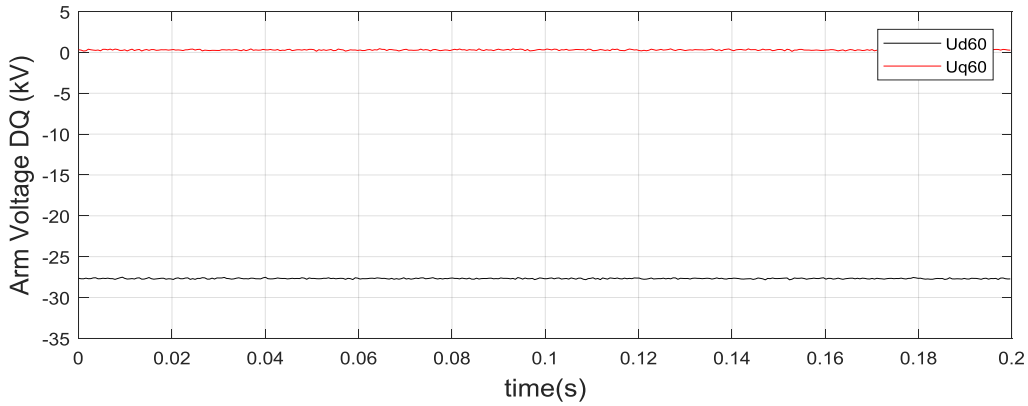

(c) DQ components of M^3C arm voltage after αβ - DQ transformation.

Fig. 3.8 M^3C arm voltages of the 60 Hz side and components after transformation.

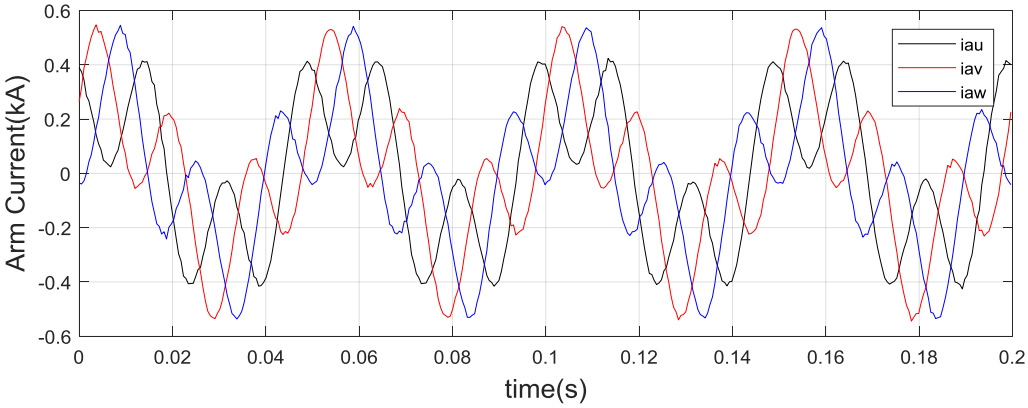

(a) M^3C arm currents: arm *au*, *av*, *aw*.

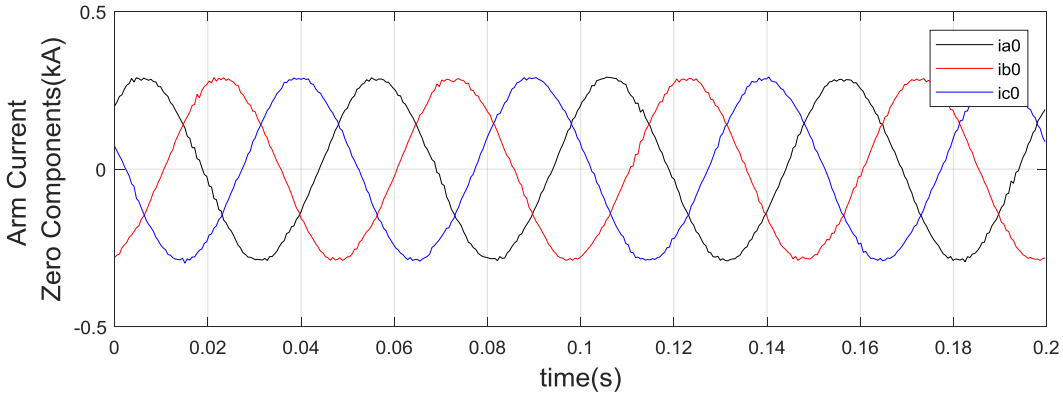

(b) Zero components (20 Hz) of M^3C arm current after ABC - αβ0 transformation.

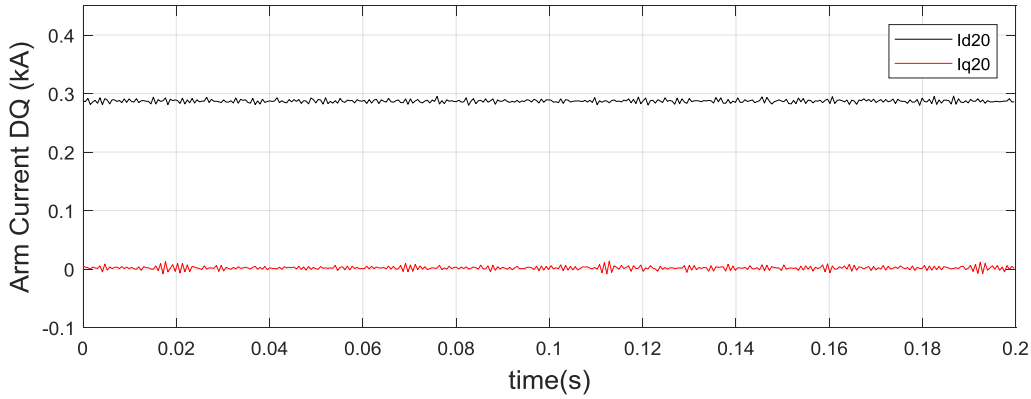

(c) DQ components of M^3C arm current after ABC - DQ transformation.

Fig. 3.9 M^3C arm currents of the 20 Hz side and components after transformation.

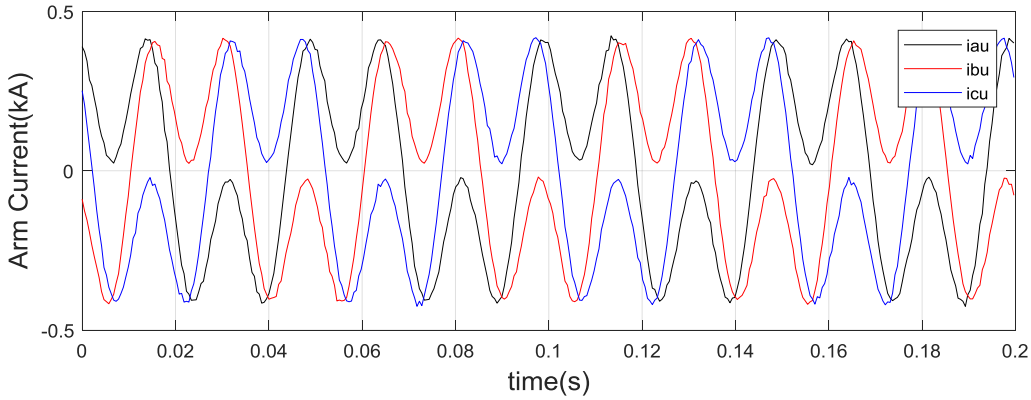

(a) M^3C arm currents: arm *au*, *bu*, *cu*.

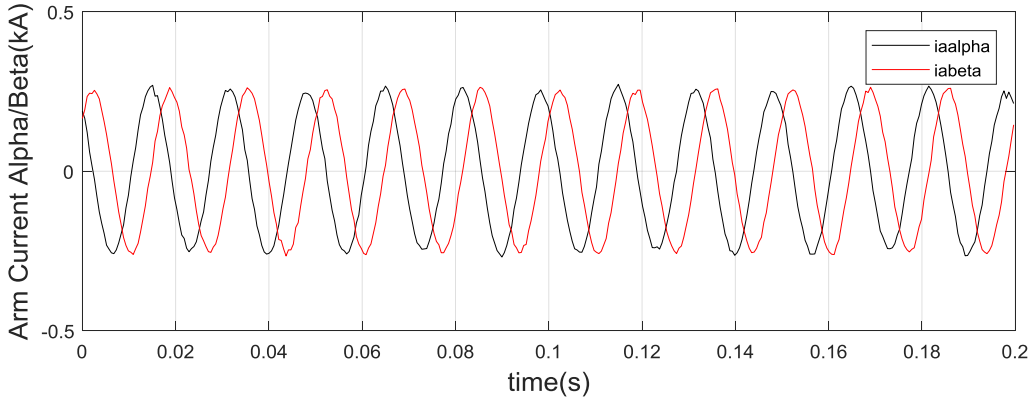

(b) Alpha and Beta components (60 Hz) of M^3C arm currents after ABC- αβ0 transformation.

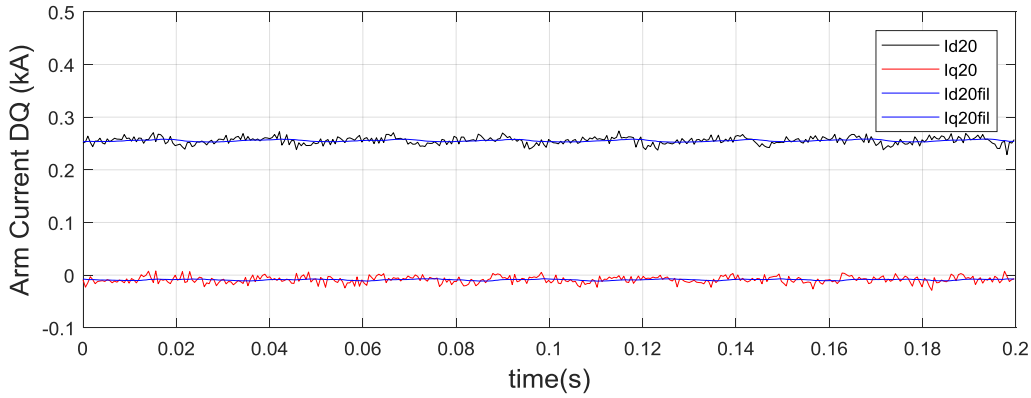

(c) DQ components of M^3C arm current after αβ - DQ transformation.

Fig. 3.10 M^3C arm currents of the 60 Hz side and components after transformation.

In addition, the 20 Hz arm voltage components of *au*, *av* and *aw* are extracted and plotted in Fig. 3.11 (a). As can be seen, three curves are overlapped, indicating that the arm voltages are balanced at the 20 Hz side. Similarly, the 60 Hz arm voltage components of *au*, *bu* and *cu* are plotted in 3.11 (b) and the arm voltages are also balanced at the 60 Hz side. For the arm currents, same process is conducted and the current waveforms are of very minor difference, indicating that the AC side phase current spreads equally into the three arms connected to it. These results show that the assumptions of balanced arm voltages and balanced arm currents are valid. Overall, the performance of the M^3C as a frequency changer is satisfactory.

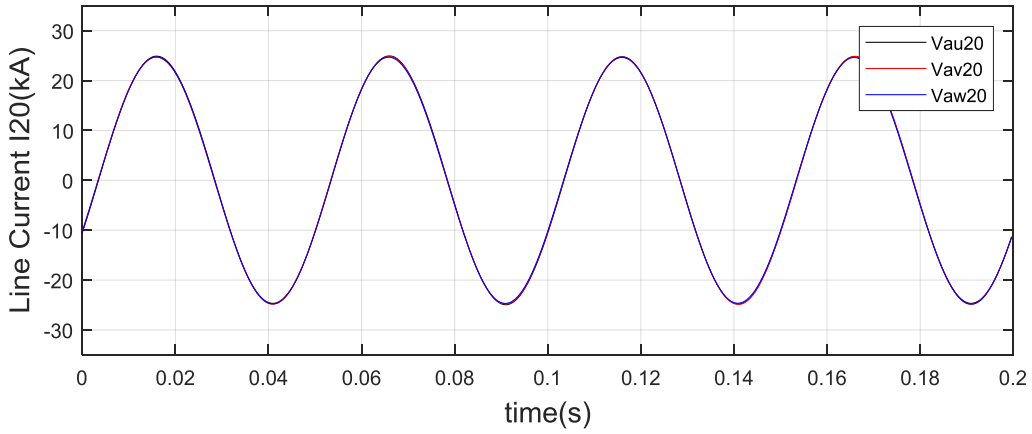

(a) 20 Hz components of M^{3}C arm voltages: arm *au*, *av*, *aw*.

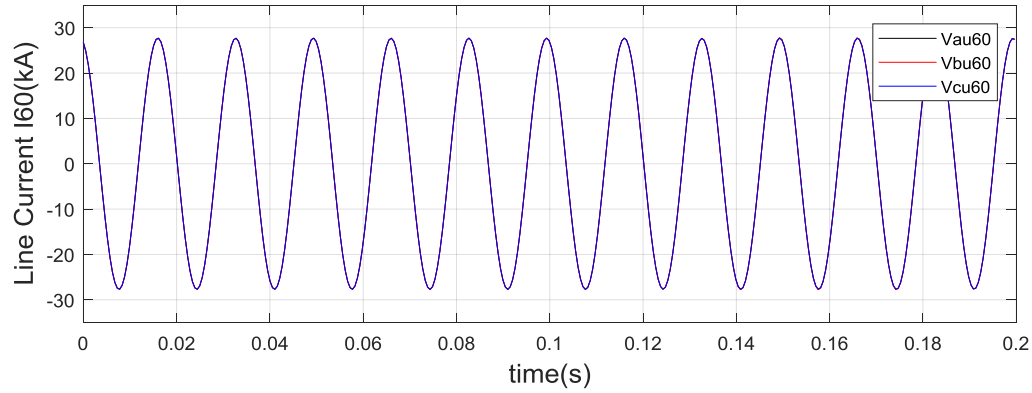

(b) 60 Hz components of M^{3}C arm voltages: arm *au*, *bu*, *cu*.

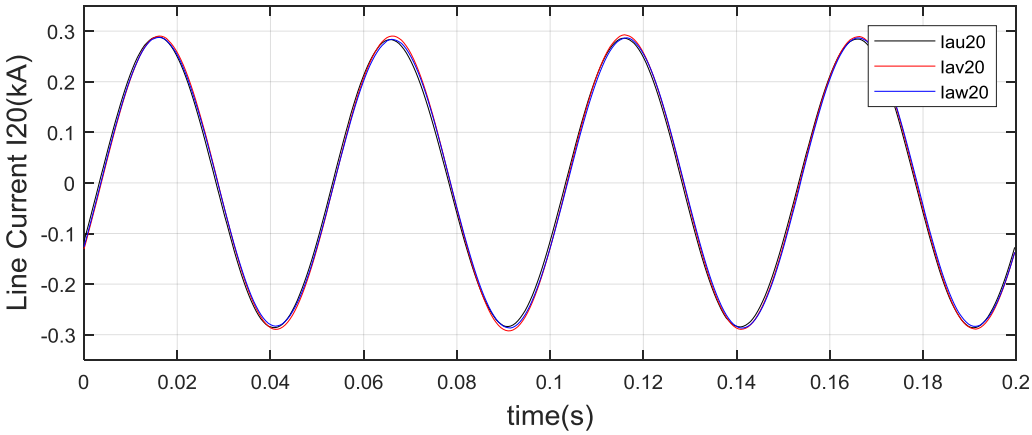

(c) 20 Hz components of M^{3}C arm currents: arm *au*, *av*, *aw*.

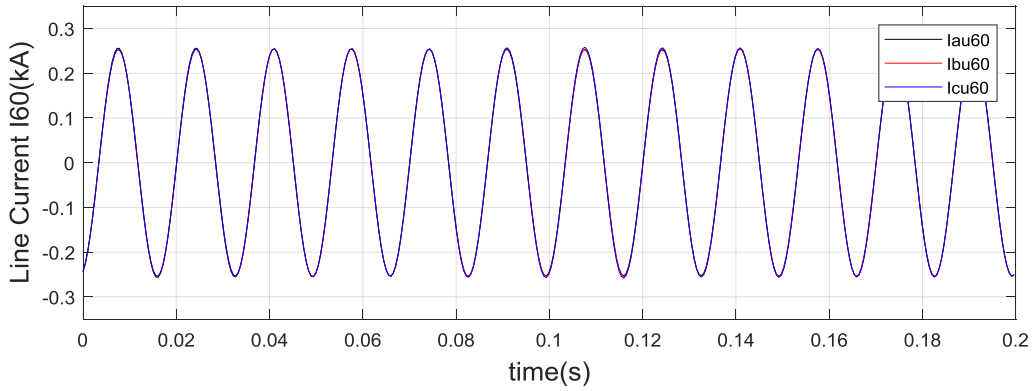

(d) 60 Hz components of M^3C arm currents: arm *au*, *bu*, *cu*.

Fig. 3.11 20 Hz and 60 Hz components of arm voltages and currents.

3.5 Power Flow Reversal

With the adoption of full bridge sub-modules, M^3C has bidirectional four-quadrant operation capability. In this section, a power flow reversal test case is designed to investigate the transient performance of the M^3C. During start-up or wind farm fault period, it is likely that the grid side provides active power to support the fractional frequency side. In this case, the reversal starts at t = 0.2 s and the power command is to reverse the active power flow in one second. Fig. 3.12 to Fig. 3.16 show the simulation results.

The reference and measured active power on the 20 Hz side are plotted together in Fig 3.12. It is shown that two curves are almost overlapped, proving that the controller performance is satisfactory and the actual active power is able to track the power reference at a rapid rate. Fig 3.13 shows the current signals of the inner loop of the vector control, where the D axis current has the same varying trend of the active power and the Q axis current remains static to be zero as it is decoupled from the D axis controller. If required, the reactive demand can be adjusted to provide reactive power support from the M^3C to both sides of the AC systems. But under

normal operation, the reactive power is regulated to be zero to maximise the capacity factor of the transmission system.

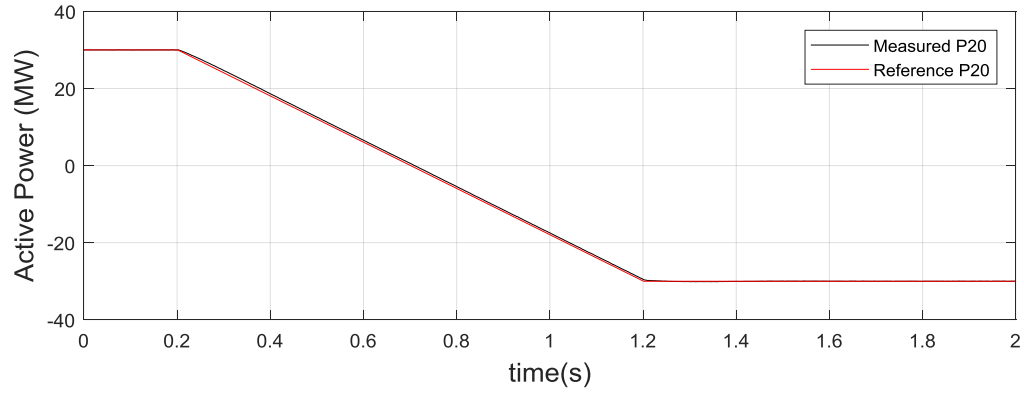

Fig. 3.12 Measured active power and its reference during power flow reversal.

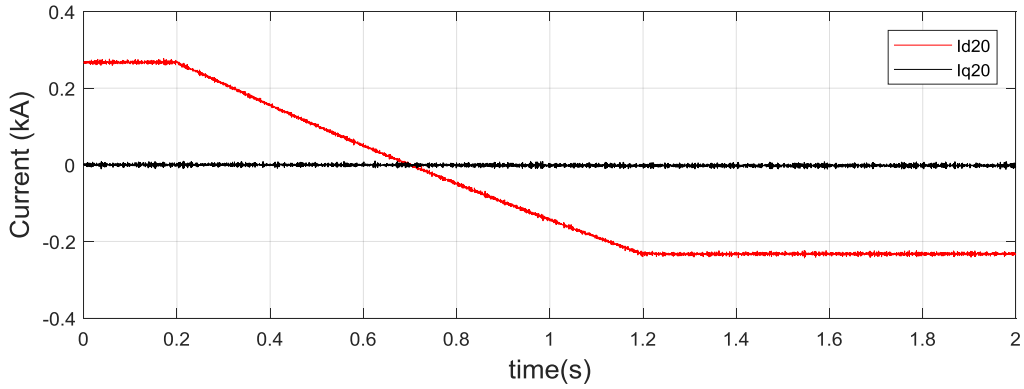

Fig. 3.13 DQ components of 20 Hz arm current during power flow reversal.

Also, the 20 Hz and 60 Hz sides AC currents are plotted in Fig. 3.14 and Fig. 3.15 respectively. They share a similar trend that the three-phase currents gradually drop to zero first as the magnitude of the power decreases, and then currents go up again as the magnitude of the power increases. In addition, Fig. 3.16 shows the DC component of the capacitor voltage, whose reference is set to be 1.5 kV. As can be seen, after the power flow reversal begins, the capacitor voltage drops about 3.3% to 1.45 kV. It remains that level until the reversal finishes and it recovers to the normal voltage level. At steady state, the active power

flowing in the M^3C equals to the active power flowing out so the sub-module capacitor voltage is balanced. However during the transient period in this case, the input active power from the 20 Hz side keeps dropping and therefore resulting in a decrease of the capacitor voltage. When the 60 Hz side controller detects the capacitor voltage drop, it takes action and reduces the 60 Hz D axis current coming out from the converter. This prevents a continuous drop of the capacitor voltage and when the power reversal finishes, the capacitor voltage is regulated to the reference value again. To sum up, the performance of the M^3C is satisfactory and the designed controllers work well.

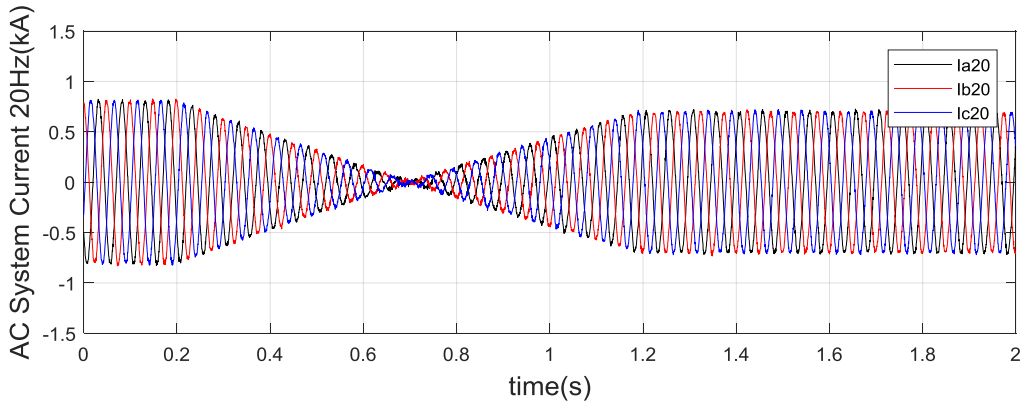

Fig. 3.14 AC system current of the 20 Hz side during power flow reversal.

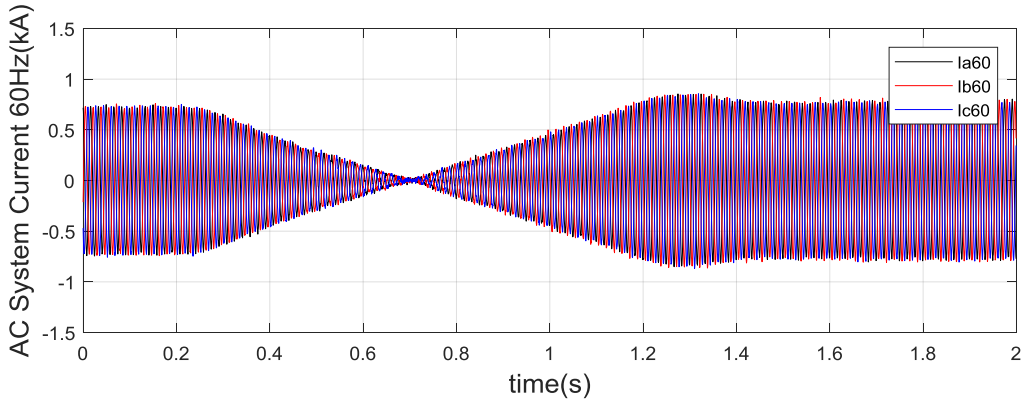

Fig. 3.15 AC system current of the 60 Hz side during power flow reversal.

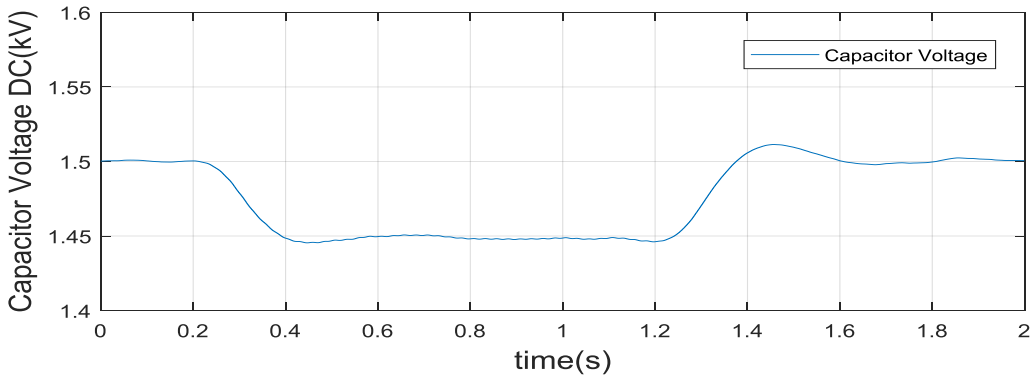

Fig. 3.16 Average capacitor DC voltage during power flow reversal.

3.6 Summary

In this chapter, the configuration, operating principle and the control strategy of the M^3C for FFTS have been discussed in details. It has been shown that voltages and currents at frequencies of the AC systems from both sides couple in the M^3C, and what transformation process should be carried out to extract the 20 Hz components and the 60 Hz components. The control method has been presented in a detailed manner including sub-module level, arm level and converter level. A time domain simulation test system has been developed to examine the operating principle and the discussed control strategy. Performance has been validated both at steady state and at transient state when a power flow reversal was conducted. It has been proven that the M^3C works well and is capable of acting as the frequency changer in an FFTS.

CHAPTER 4 COST ANALYSIS AND COMPARISON BETWEEN MMC AND M^3C FOR OFFSHORE WIND POWER TRANSMISSION

4.1 Introduction

4.1.1 Background

After extensive exploitation in recent years, the development of near-coast wind farm is nearly saturated. Development of wind power systems is moving further offshore where richer wind resource is available and large-scale project planning is easier. It has been discussed in previous chapters that M^3C FFT is a promising option for offshore wind power transmission at medium distance. For long distance transmission, MMC HVDC is a popular candidate. According to [41], the average capacity of offshore wind farm commissioned in Europe in 2016 was 380 MW and the average distance to land was about 45 km. Such figures present a great opportunity for FFTS development. Therefore, it is vital to carry out a cost analysis of M^3C FFT and a cost comparison with MMC HVDC. Current researches either do not model the cost of M^3C properly, or consider only the initial investment and neglect the long-term costs. However, the life time of offshore wind power systems are often designed between twenty to twenty five years. The overall value of the long-terms costs can be considerable and has a great effect on the analysis and decision making. In this chapter, a cost model is developed to include capital cost and time-related costs to provide a precise cost profile of the technology. The overall cost is classified into elements and those take up large percentages in the total cost are emphasised. Cost comparison between M^3C FFT and MMC HVDC is

presented. Economical crossover distance of the two technologies is analysed at different power ratings. Also, sensitivity analyses are carried out on discount rate, wind farm capacity factor, wind energy price and turbine generator type to gain in-depth understanding into their impact on the cost comparison.

4.1.2 Cost Breakdown of Offshore Wind Power System

On one hand, the overall cost of an offshore wind farm can be formed of the costs of system components, which are wind turbine for generation, transformer for voltage stepping up, undersea cable for power transmission and converter station for frequency changing. On the other, the overall cost can also be divided by the nature of the costs, which are caused before operation or during operation. They include capital cost, unavailability cost, O&M cost and power loss cost. The latter classification can be expressed mathematically as:

$$C_{sys} = C_{CAP\_sys} + C_{UA\_sys} + C_{OM\_sys} + C_{PL\_sys} \quad (4.1)$$

in which C_{CAP_sys} is capital cost, C_{UA_sys} is unavailability cost, C_{OM_sys} is O&M cost and C_{PL_sys} is defined as power loss cost of the offshore wind power system and they will be introduced in later sections respectively. Except the capital cost, the other three costs are long-term costs that are introduced during the operation and through the life time of the system. To consider the time effect of the money, Equation (4.2) is used to convert the time-related costs throughout the wind farm life time to net present cost (NPC) [84]:

$$C_{NPC} = C_{annual} \frac{(1+i)^n - 1}{i(1+i)^n} \quad (4.2)$$

in which C_{annual} is the annual value of the long-term cost, n is the offshore wind system life time (20 – 25 years) and i is the discount rate. Table 4.1 shows the detailed cost breakdown of an offshore wind power project in two dimensions which has been discussed above.

Table 4.1 Cost breakdown of an offshore wind power project

Total Cost (TC) =	**Wind Turbine Cost (WTC)**	**Transformer Platform Cost(TPC)**	**Cable & Compensation Cost (CCC)**	**Converter Station Cost (CSC)**
Capital Cost (CC)	Wind Turbine Capital Cost (WTCC)	Transformer Platform Capital Cost (TPCC)	Cable & Compensation Capital Cost (CCCC)	Converter Station Capital Cost (CSCC)
Unavailability Cost (UC)	Wind Turbine Unavailability Cost (WTUC)	Transformer Platform Unavailability Cost (TPUC)	Cable & Compensation Unavailability Cost (CUC)	Converter Station Unavailability Cost (CSUC)
Operation & Maintenance Cost (OMC)	Wind Turbine Operation & Maintenance Cost (WTOMC)	Transformer Platform Operation & Maintenance Cost (TPOMC)	Cable & Compensation Operation & Maintenance Cost (CCOMC)	Converter Station Operation & Maintenance Cost (CSOMC)
Power Loss Cost (PLC)	Wind Turbine Power Loss Cost (WTPLC)	Transformer Platform Power Loss Cost (TPPLC)	Cable & Compensation Power Loss Cost (CCPLC)	Converter Station Power Loss Cost (CSPLC)

4.2 Capital Cost

In this section, the capital costs of different components in the offshore wind power system are discussed and analysed. Relevant data are collected and presented in graphs and tables.

When it comes to wind turbine generators, permanent magnet synchronous generator (PMSG) and doubly-fed induction generator (DFIG) are the two most popular types in the wind energy market nowadays [40]. Generally, the capital cost of a wind power generator introduces in the process of manufacture, transport, installation and also includes foundation construction.

Because of confidential reasons, the cost data of wind turbine generators are scarce in the public domain and they may vary from supplier to supplier and from project to project. Estimated by the National Renewable Energy Laboratory (NREL), the generator cost of offshore wind turbine is approximated to be £1m/MW [85]. But it is an average number and does not consider the difference between various types of wind turbine generators. According to [86], the reference costs of specific wind turbine generators are given, with PMSG at about £1.55m/MW and DFIG at about £1.8m/MW. Thanks to technology development and commercial competition, a decreasing trend of the wind turbine price is anticipated. Except that there is a concern for PMSG, as its cost is greatly affected by the expensive rare earth magnets whose price is fluctuating along time. In [87], the cost breakdown of a DFIG is presented and it is shown as in Fig. 4.1.

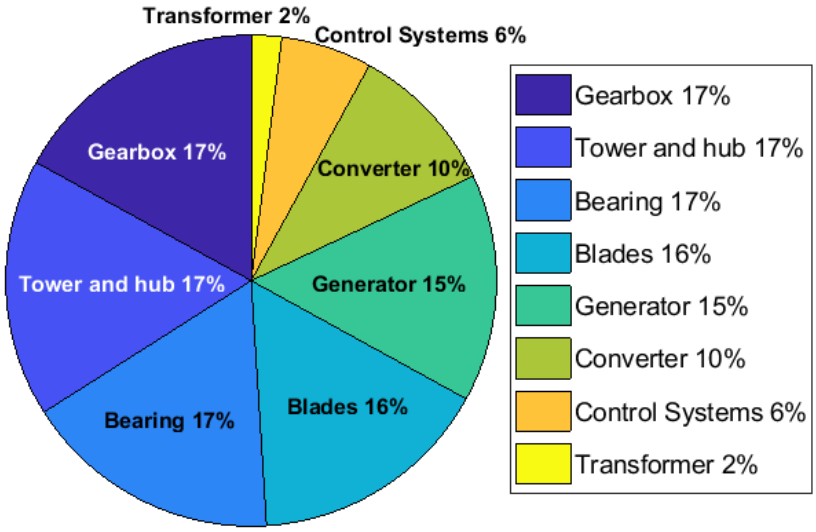

Fig. 4.1 Cost components of a DFIG wind turbine generator.

As can be seen, gearbox, tower and hub are some of the main cost components. The research shows that when the wind turbine generator works at the low frequency, the gearbox can be simplified and the switch ratio is reduced to one third so the cost on gearbox can be

decreased. In addition, simplified structure of the gearbox leads to a lighter weight of the wind tower and the hub. It is estimated that the cost of DFIG can be saved by 5.2% [88]. This advantage is not taken into consideration in this research when the wind turbine generator type is PMSG, as most PMSGs available nowadays are direct-driven and does not include a gearbox. However, it may be useful to point out that the novel high power PMSG (8 - 10 MW) also employs a one-level gearbox [89]. Consequently, saving could apply to PMSG as well.

For the capital costs of the offshore transformer station and the converter stations, average costs are given in a Northseagrid report [90] and are listed in Table 4.2. At the same nominal power, transformer at the fractional frequency tends to be bulker and more expensive. Calculation result in [91] shows that the transformer would be about 75% more expensive for FFTS. For an onshore converter station, capital cost includes the cost of land, building construction, cost of valves etc. Considering that MMC can use half bridge sub-modules while M^3C needs to use full bridge sub-modules, the valve cost is higher for the onshore M^3C station. [92] shows that when using full bridge converter, the overall converter station cost is 20% higher than a half bridge converter station. For MMC HVDC, 6 arms are placed in the offshore rectifier station and the other 6 arms are placed in the onshore inverter station. For M^3C FFT, there is no offshore station and all 9 arms are located onshore. Taking that into consideration, the capital expenditure of the M^3C converter station is approximately 1.8 times as the price of the MMC HVDC onshore converter station.

The mathematical equation to calculate the capital cost of the cable is given as:

$$C_{CAP\_cab} = n_{cab} \cdot l_{cab} \cdot c_{cab} \tag{4.3}$$

in which n_{cab} is the number of submarine cable sets, l_{cab} is refined as the transmission distance (km) and c_{cab} is the submarine cable price (£m/km). For standardisation reason, cables are available only at certain voltage levels. In this research, 132 kV, 220 kV and 400 kV are considered for AC and 150 kV and 300 kV are considered for DC. Capital costs of cables are extracted from [43] and are listed in Table 4.2. Selection of undersea cable is determined by the power capacity of the wind power system and transmission distance. For HVAC cables, the maximum transmitted active power decreases as the distance increases, since the charging current would take up more and more rating of the cable. FFT is meant to address the main disadvantage of HVAC. Operating at one third of the frequency, the required charging current is greatly reduced and therefore the transmission capability is increased. For instance, [93] shows that FFTS is capable of transmitting 500 – 600 MW power to a distance of 300 – 400 km at a voltage level of 220 kV with the help of reactive power compensation. This capability can satisfy most requirements of offshore wind power systems in terms of distance, and higher voltage level can further improve the transmitting capacity. For reactive compensation, different costs are given when compensation methods are different, such as: single compensation from one end, compensation from both ends with equally split capacity, compensation from both ends with different capacities for two ends, and three compensation locations at both ends and the midpoint. In this research, it is adopted that the reactive power compensation is provided from both ends with same capacity. Compensation costs are available in [94] and they are plotted with transmission distance in Fig. 4.2 considering three voltage levels. It can be viewed that the costs are nearly linearly dependent on distance, so first-order linear cost functions are calculated to determine compensation cost.

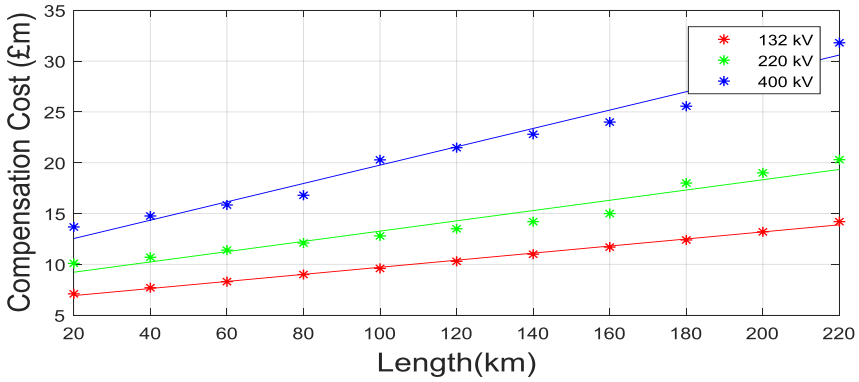

Fig. 4.2 Compensation cost for reactive power at different voltage levels.

Table 4.2 Summary of capital costs of offshore wind power system components

Component	Capital Cost
DFIG	£1.8m/MW
DFIG at fractional frequency	£1.7m/MW
PMSG	£1.55m/MW
Offshore transformer (plus platform)	£0.129m/MW
Offshore transformer FFT (plus platform)	£0.194m/MW
Offshore Converter Station	£0.254m/MW
Onshore Converter Station	£0.107m/MW
Onshore M^3C Station	£0.171m/MW
AC Cable (FFT)	
132 kV (0-300 MW)	£0.86m/km
220 kV (300-600 MW)	£1.00m/km
400kV (600-1000 MW)	£2.15m/km
DC Cable	
±150 kV (0-500 MW)	£0.785m/km
±300 kV (500-1000 MW)	£1.015m/km

4.3 Unavailability Cost

Unavailability cost is determined by the amount of energy not delivered to the power system resulting from the unavailability of an offshore wind power system. Based on the IEC Standard 61400 [95], the unavailability of a system is defined as the ratio between the total unavailable time of the system and the time length of the studied period. It is mathematically expressed as Equation (4.4) on an annual base, in which UA_{sys} is the unavailability rate of the offshore wind power system, t_{UA_sys} is refined as the overall unavailable time of the offshore wind power system within one year (in hours) and T_{year} is the overall time of one year which equals to 8760 hours.

$$UA_{sys} = \frac{t_{UA\_sys}}{T_{year}} \times 100\% \tag{4.4}$$

The unavailability cost equals to the total amount of energy not supplied multiplied by the unit energy price:

$$C_{UA\_sys} = UA_{sys} \cdot P_{rated} \cdot CF \cdot EP_{wind} \cdot T_{year} \tag{4.5}$$

in which C_{UA_sys} is defined as the unavailability cost of the system, P_{rated} is defined as the nominal power rating of the offshore wind power system (MW), CF is defined as the capacity factor of the system and EP_{wind} is defined as the offshore wind energy price (£/MWh). It should be pointed out that unavailability only takes into account the unscheduled down time and excludes planned maintenance time out of the calculation. Also, it is presumed that only one fault could happen in the system at a time. That is to say, when one component suffers from a fault, the system would stop operating so there would not be another fault happen on

the rest components. As a consequence, the total unavailability of the system can be calculated as the sum of unavailability of each single component:

$$UA_{sys} = UA_{wt} + UA_{tran} + UA_{cab} + UA_{con} \quad (4.6)$$

where UA_{wt}, UA_{tran}, UA_{cab} and UA_{con} are the unavailability of the turbine, transformer, submarine cable and converter respectively.

In a wind turbine, most unavailable time is from the gearbox, rotor blade, generator, and converter power electronic devices [96]. The data of wind turbine annual failure rate and downtime (in day) are collected from [96, 97] and they are summarised as in Table 4.3. The unavailable time in a year can be calculated by multiplying failure rate and downtime.

Table 4.3 Unavailability of components in a wind turbine

Failure Rate (per year)	PMSG	DFIG	Downtime(/days)
Gearbox	/	0.185	42
Generator	0.046	0.123	32
Rotor Blade	0.16	0.16	42
Converter Electronics	0.593	0.106	2

It can be seen from Table 4.3 that for PMSG, the failure rate of power electronics is higher than that of DFIG. But its advantage is that it does not have gearbox and therefore there is no gearbox failure time. The reason of higher converter failure rate is that PMSG employs a fully rated converter that is more prone to faults with higher power rating and larger size than the partially rated converter employed by DFIG. As has been discussed in Section 4.2, the structure of the gearbox can be simplified to a great extent for wind turbine generators

working at the low frequency. Accordingly, the gearbox failure rate would also drop and it is presumed that the reduction of the failure rate is also one third of the original.

Fractional frequency has been adopted for more than one century in railway systems in a number of countries [98]. Therefore, the technology of transformers at fractional frequency is mature and it is considered that they operate as reliably as the transformers at normal grid frequency. The failure rates and downtime of the cables and transformer are available in [90] and they are listed in Table 4.4. For the sake of simplicity, the unavailability of multilevel converters is assumed to be linearly dependent on the power electronic sub-module number. But onshore and offshore converter stations should be considered separately. For onshore converter station, unavailability data are extracted from a thorough GIGRE survey of the reliability of a large number of HVDC systems all over the world [99]. For offshore converter station, data for the past three years on existing offshore wind farm projects are collected and an average unavailability rate is calculated [100]. In total, the components unavailability in offshore wind power systems is given in Table 4.5.

Table 4.4 Reliability of transformers and cables

Component	Failure Rate(per year)	Downtime(/hours)
Transformer	0.024	2160
AC Cable(/100km)	0.1114	1440
DC Cable(/100km)	0.1114	1440

Table 4.5 Unavailability of offshore wind components

Symbol	Quantity	Value (%)
UA_{wt}	Unavailability of wind turbine	/
UA_{PMSG}	Unavailability of PMSG	2.57
UA_{DFIG}	Unavailability of DFIG at grid frequency	5.11
UA_{DFIGFF}	Unavailability of DFIG at fractional frequency	3.69
UA_{tran}	Unavailability of transformer	0.59
UA_{cab}	Unavailability of cable per 100km	0.18
UA_{con}	Unavailability of converter station	/
UA_{mmc_on}	Unavailability of MMC HVDC onshore converter station	0.35 [99]
UA_{mmc_off}	Unavailability of MMC HVDC offshore converter station	0.8 [100]
UA_{m3c}	Unavailability of M^3C onshore converter station	0.52

4.4 Operation & Maintenance Cost

For offshore wind power systems, the O&M costs can be produced from multiple activities [101]. Labour, replaced components, vessel expenses, rent, accounting costs and insurance are common sources of O&M costs. The challenge is that the actual data for O&M costs of existing offshore wind farm projects are not available in the public domain. And actual O&M costs are varied from case to case depending on the geographical condition and the location of the offshore wind power system. O&M costs may be different as the maintenance frequency, availability of skilful workers and ships, and weather and sea condition are varied in each offshore wind power system. Since average statistics may not be representative, in economic

studies, the O&M cost for each component on an annual base can be estimated as a ratio of the capital cost [42, 102]. This O&M cost ratio $k_{O\&M}$ is defined as:

$$k_{O\&M} = \frac{c_{O\&M\_com}}{C_{CAP\_com}} \times 100\% \tag{4.7}$$

where $c_{O\&M\_com}$ is the annual expenditure of O&M on the component and C_{CAP_com} is the capital cost of the component. Various components have different O&M cost ratios, for instance, the offshore wind turbine needs more O&M while the transformer needs less maintenance as it is more mature in terms of technology and has no rotating mechanical part. Also, a converter station located offshore has a higher O&M ratio than the one locating onshore. References [85, 90] present the O&M cost ratios for various components in offshore wind power systems, which are listed in Table 4.6.

Table 4.6 O&M ratio for different components

Component	O&M Ratio(/ year)
Wind Turbine	3.4%
Offshore Converter Station	2%
Onshore Converter Station	0.7%
Submarine Cable	2.5%
Offshore Transformer	0.15%

4.5 Power Loss Cost

The economic effect of power loss is considered in this section. The overall power loss of the offshore wind power system is calculated as the sum of power loss from each of the

components and it is converted to power loss cost based on the offshore wind energy price. It can be mathematically expressed as:

$$C_{PL\_com} = PL_{com} \cdot P_{rated} \cdot T_{rated} \cdot EP_{wind} \quad (4.8)$$

in which C_{PL_com} is the power loss cost, PL_{com} is the power loss ratio (%) of the component, T_{rated} is the operation time of the system annually. In offshore wind power systems, power loss is normally in the forms of mechanical loss, iron loss, copper loss and converter power electronic loss. Comparing two types of wind turbines, according to [103], power loss of PMSG is mainly converter electronic loss due to the efficiency of the two or three levels converter is not very high, and PMSG adopts fully rated back-to-back converter. For DFIG, mechanical loss particularly gearbox loss takes up large proportion of the overall wind turbine loss. DFIG operating at the fractional frequency has lower gearbox loss and it is approximated to be one third of the original. A detailed calculation of the power loss for the two kinds of wind turbines is available in [103]. The result is shown in Table 4.7.

For transformers, power losses are mainly brought by the heating current in the windings and the magnetizing current in the core. According to [104], the efficiency of transformers is found to be high and the average power loss ratio is 0.8%. Hence, the difference of the transformer power loss ratio between operating at the fractional frequency and at grid frequency is neglected for simplicity and only negligible discrepancy would be brought. It can be confirmed by comparing the power loss ratio to those of other elements in the offshore wind power system in Table 4.7.

The power loss ratios are different for AC cable and DC cable. For DC cable, the primary source of the power loss is the active current flowing through the cable, while for AC cable, both the active current and the reactive current which is produced by cable capacitance

contribute to the power loss. Therefore, the loss of AC cable is larger than that of DC cable. [15, 94] present calculation details of the power loss for AC and DC cables. Results show that AC cable has a power loss ratio between 3-5% depending on the voltage level when length is 100 km. And DC cable only has 0.5-2.5% at the same length.

For converter, switching loss and conduction loss are two main sources of power loss. MMC HVDC adopts half bridge sub-modules, the total converter loss per converter station nowadays is about 1% of the rated power. For M^3C, sub-modules are full bridge so power loss is higher. Based on the analysis in [105], the switching loss for full bridge and half bridge valve are the same, while the conduction loss for full bridge valve is double than half bridge valve. As a result, the power loss of the M^3C is calculated to be 1.95%.

Table 4.7 Power loss for different components

Component	Power Loss (%)
PMSG	6.4
DFIG	5.0
DFIG at fractional frequency	3.0
Transformer	0.8
AC Cable (per 100 km)	3.0 - 5.0
DC Cable (per 100 km)	0.5 - 2.5
Offshore Converter Station	1.0
Onshore Converter Station	1.0
Onshore M^3C Station	1.95

4.6 Case Studies of Cost Analysis and Comparison

4.6.1 Cost Constituents of MMC HVDC and M^{3}C FFT

Previous sections present the cost breakdown of the overall cost of offshore wind power systems. Capital cost, unavailability cost, O&M cost and power loss cost are discussed and necessary cost data are provided. In this subsection, quantitative analysis of offshore wind power systems costs for MMC HVDC and M^{3}C FFT are presented. Elements that have large influences on the total cost are indicated. In this case, the power rating is chosen as 500 MW, the transmission length is set to be 100 km, the wind turbine type is selected to be PMSG and the system life time is deigned to be 20 years. Other parameters required to compute the cost components are listed in Table 4.8 and they can be referred to [84, 106, 107]. The cost constituents for offshore wind power systems based on the two technologies are plotted in Fig. 4.3.

Table 4.8 Parameters for economic analysis case study

Symbol	Explanation	Value
CF	Capacity factor	40% [106]
T_{rated}	Rated operation time	2500hrs [106]
i	Discount rate	5% [84]
EP_{wind}	Offshore wind energy price	£50/MWh [107]
n	Project life	20 years

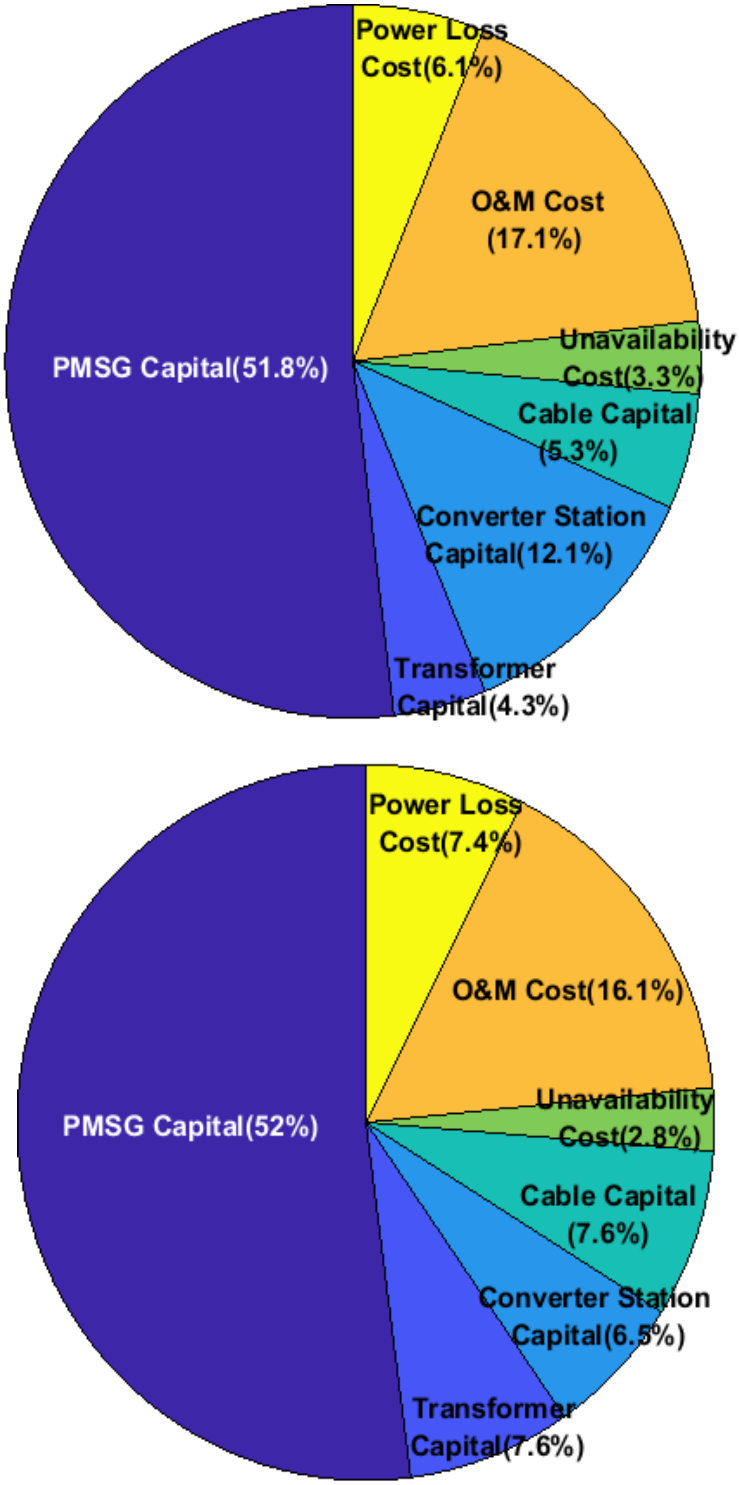

Fig. 4.3 Cost constituents for MMC HVDC (top) and M^3C FFT (bottom) offshore wind power systems.

As can be seen, there are some similarities between the two technologies. For example, no matter which transmission technology is adopted, about 50% of the total project cost is spent on the capital expenditure of the wind turbines, which is the biggest cost contributor. Ranking second is the O&M cost, which is about and less than 20%. The amount is the total value for 20 years converted to net present cost, and the same rule applies to all the other long-term costs, including unavailability cost and power loss cost. Both technologies result in a power loss cost of less than 10% and the smallest proportion is taken up by the unavailability cost. On the other hand, there are some differences between the two technologies. For M^3C FFT, the undersea cable and the offshore transformer station are more expensive. But there is a huge saving compared to MMC HVDC on converter station capital cost. To conclude, the total cost of offshore wind power systems is greatly driven by capital costs, among which the wind turbines are the most costly so it is important to carry out research on how to cut the wind turbine capital cost down to make offshore wind power more competitive. In the next two subsections, focus is paid on comparing the two technologies and determining the economical transmission distance for each of the technology.

4.6.2 Economical Transmission Distance: Case Study 1

In this case study, the economical transmission distances for the two technologies are determined when the rated capacity of the offshore wind power system is 500 MW. The crossover point is indicated and an analysis of the cost difference is provided. Fig. 4.4 plots the total costs of the two technologies against the transmission distance. As can be seen, the crossover point lies at distance L = 109 km, before which the M^3C FFT option is of lower cost while a transmission distance longer than that results in MMC HVDC being the cheaper choice. To analyse the reason behind, two points are selected which are slightly shorter and

longer than the crossover distance (L = 100 km and L = 120 km) and the cost differences are plotted at each point in Fig. 4.5, regarding capital, unavailability, O&M and power loss costs. Note that delta in the figure represents MMC HVDC minus M^3C FFT, so a positive value means that MMC HVDC is more expensive.

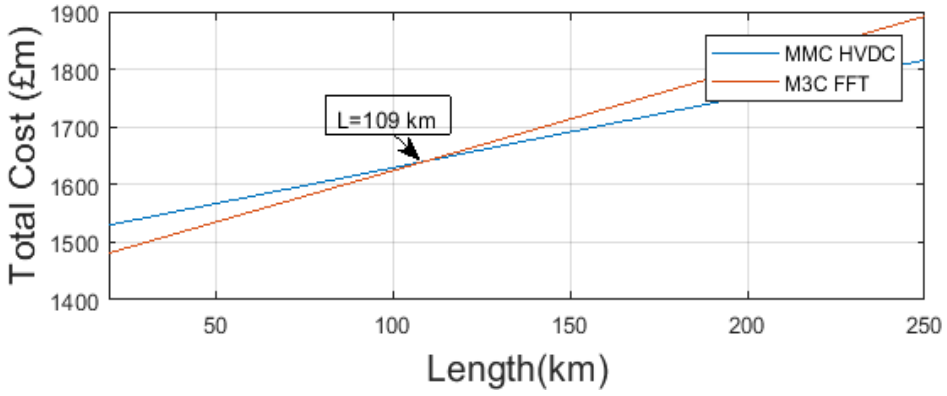

Fig. 4.4 Total cost against transmission distance at 500 MW.

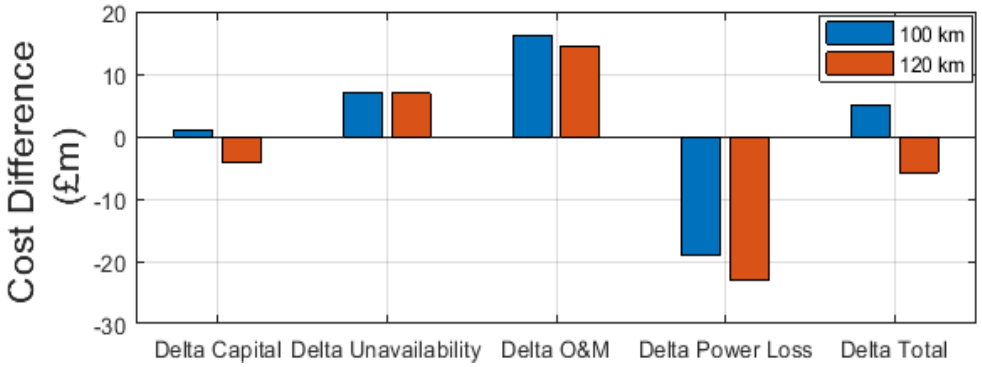

Fig. 4.5 Cost differences around the crossover point (L = 100 km and L = 120 km).

When the distance is short, the converter stations play a more significant role in the total cost. At the distance L = 100 km, MMC HVDC has a higher capital cost on converter station due to the extra offshore rectifier station, while the AC cable and the offshore transformer station for M^3C FFT are more expensive. Combining both factors results in a very small cost difference on capital cost. The biggest positive cost difference comes from O&M, again due to the offshore converter station. The M^3C station locates onshore and is therefore much easier for

O&M, as it does not depend on the weather and sea condition or the availability of the vessels. However the main disadvantage comes to the higher power loss of the AC cable compared to the DC cable. To conclude, the cost difference of capital, unavailability and O&M costs are positive and the cost difference of power loss cost is negative, leading to a positive cost difference of total cost. Nevertheless, as the transmission distance becomes longer at L = 120 km, the shortcoming of the AC cable becomes more prominent, as its capital, O&M and power loss costs all increase. The growth is so large that it compensates for the advantages on unavailability and onshore M^3C converter station. Hence, the total cost difference at this distance reduces to negative and M^3C FFT is less cost-effective than MMC HVDC at long distance transmission.

4.6.3 Economical Transmission Distance: Case Study 2

In case study 2, the rated capacity of the offshore wind power system is considered to be larger at 1 GW, while all the other parameters remain the same. The focus is to discover how the power rating affects the economical transmission distance crossover point. Again the total costs of the two technologies against the transmission distance are plotted.

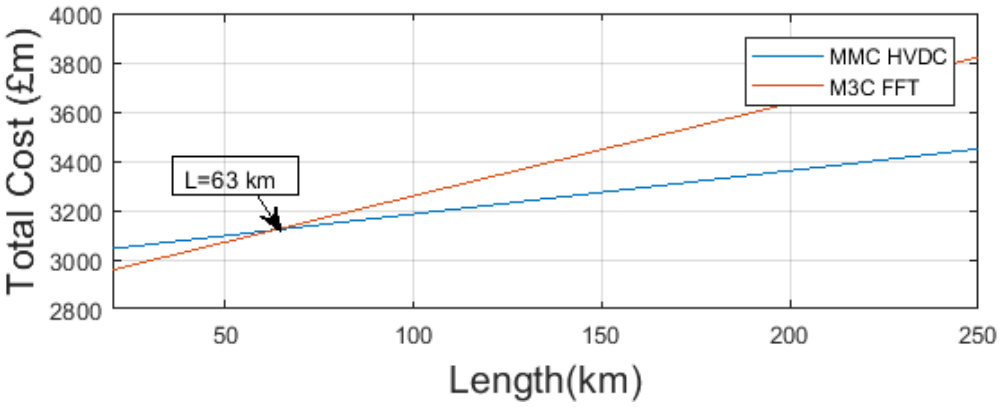

Fig. 4.6 Total cost against transmission distance at 1 GW.

In Fig. 4.6, it can be observed that when the power rating doubles, the total cost also increases to about two times of the original. However, it is interesting that the crossover distance reduces to only 63 km in this case. The reason is that in the high power rating case, the AC cable becomes dominant as its price is way too expensive when comparing to the DC cable. The economic advantage developed from other savings is rapidly cancelled out with the growth of the distance. At a distance as short as 63 km, the traditional HVAC technology may be taken into consideration since it is a capable choice with the support of the reactive power compensation and does not have costs on converter station and has lower costs on the offshore transformer. If that is the case, there may be no economical distance range for M^3C FFT. Based on the result, conclusion can be drawn that increasing the rated capacity of the offshore wind power system has a negative effect on the economic competitiveness of M^3C FFT. Apart from the economic consideration, M^3C FFT still has the technical advantages on offshore grid forming and better fault handling ability. But attention should be paid to AC submarine cable technology in order to cut down the high price and make M^3C FFT more competitive for large capacity transmission.

4.6.4 Sensitivity Analysis

Undoubtedly, the industry of offshore wind power is far from being mature and dramatic changes are still happening. As a consequence, it is essential to carry out sensitivity analysis to gain insights into the economic analysis and determine how parameter changes would influence the economical transmission distance. In this subsection, a) discount rate (i), b) energy price (EP_{wind}), c) capacity factor (CF), d) wind power project life time (n) and e) the wind turbine generator type are considered in the sensitivity analysis. Results are plotted in Fig. 4.7 when capacity is chosen to be 500 MW which is the same as in case one.

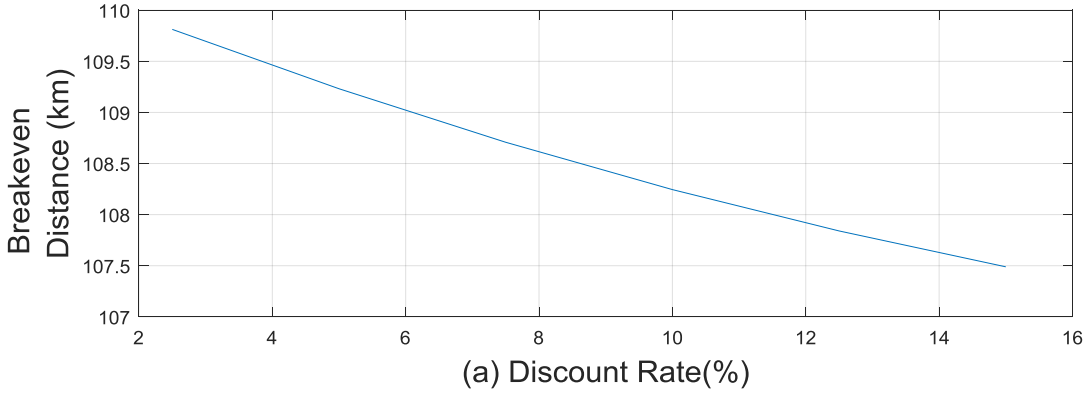
Breakeven
Distance (km)
110
109.5
109
108.5
108
107.5
107
2
4
6
8
10
12
14
16
(a) Discount Rate(%)

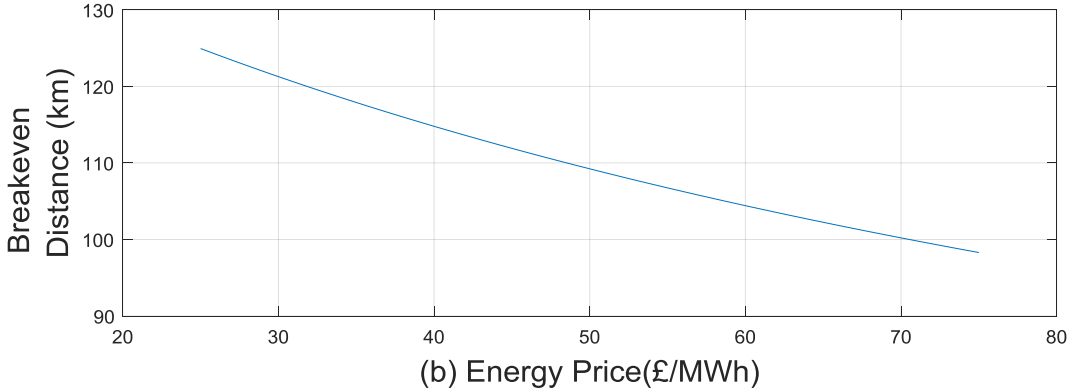
Breakeven
Distance (km)
130
120
110
100
90
20
30
40
50
60
70
80
(b) Energy Price(£/MWh)

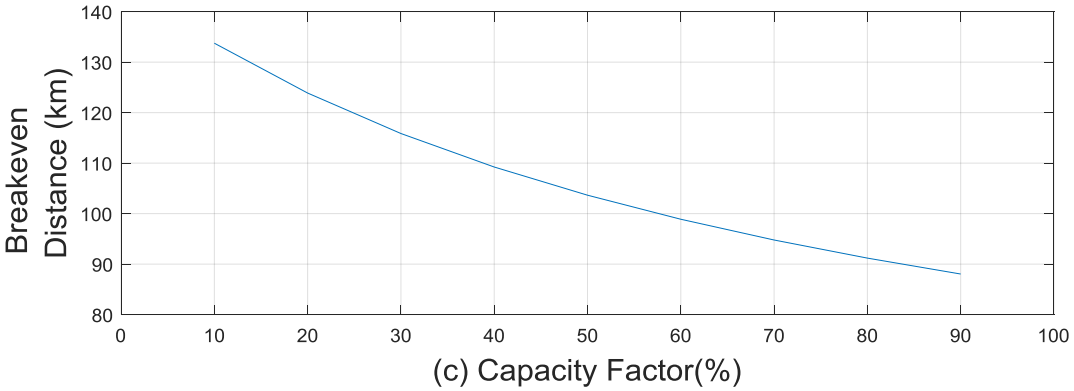
Breakeven
Distance (km)
140
130
120
110
100
90
80
0
10
20
30
40
50
60
70
80
90
100
(c) Capacity Factor(%)

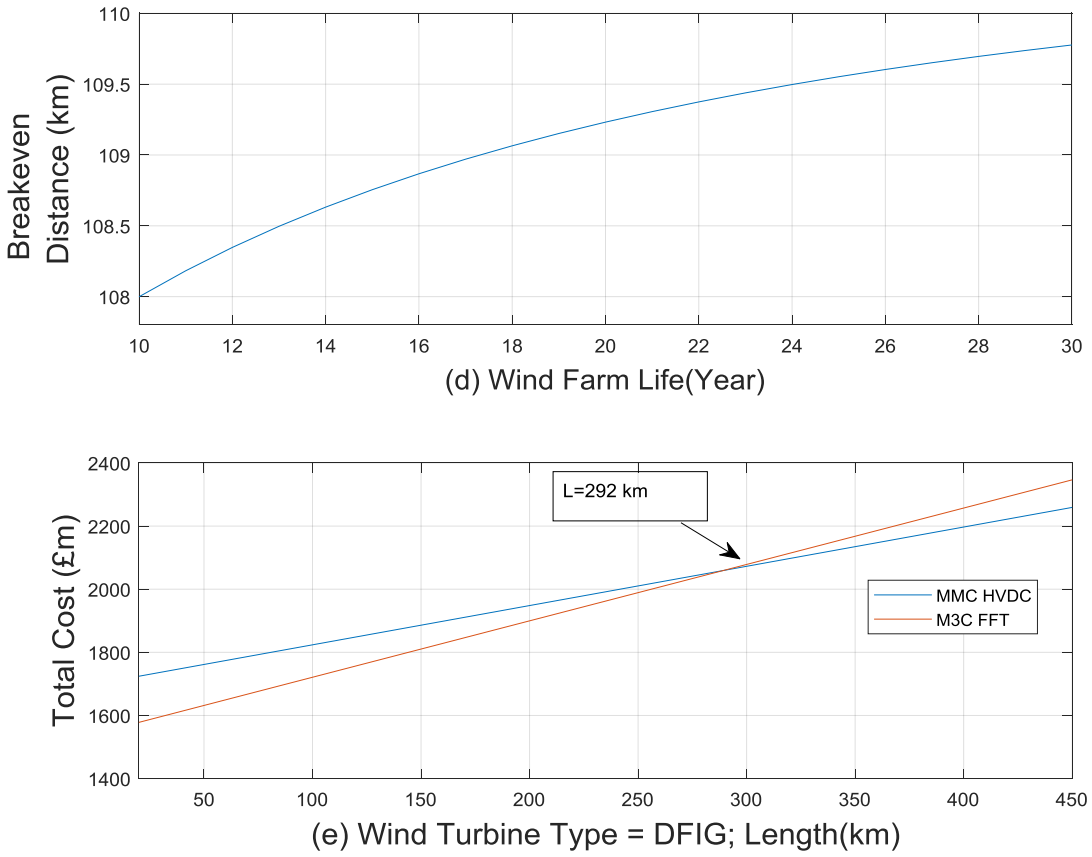

Fig. 4.7 Sensitivity analysis on economical distance and wind turbine type.

The value of discount rate is affected by the social inflation rate, risk of the capital investment and the profit return capability of the project. Discount rate only causes influence on costs that happen in the future. A larger discount rate would emphasise the capital cost and weaken the effect of the long-term costs (unavailability, O&M and power loss costs). This trend magnifies the disadvantage of the AC undersea cable so a larger discount rate negatively affects M^3C FFT. Hence, Fig. 4.7 (a) shows that the crossover distance point moves down as discount rate grows.

Besides, similar trend can be found as energy price increases. As discussed in Sections 4.3 and 4.5, energy price influences the unavailability cost and power loss cost. But unavailability cost takes up the smallest proportion in the cost constituents and is less dominant than the

power loss cost. A more important factor is that higher power loss is induced for longer transmission distance but cost difference of unavailability is not sensitive with length changes. With the same amount of AC cable power loss, a higher energy price means higher power loss cost. Therefore, a decreasing trend can be seen in Fig. 4.7 (b).

In terms of capacity factor, it linearly affects unavailability cost according to Equation (4.5). It is known that near the crossover distance the unavailability cost of MMC HVDC is higher than that of M^3C FFT. From this perspective it seems that higher capacity factor would be advantageous to M^3C FFT. However, higher capacity factor results from higher wind power captured or longer annual operation time of the system, which means the delivered power as well as the power loss on AC cable also enhances. This factor is more significant and therefore Fig. 4.7 (c) shows a descending trend as capacity factor grows.

Regarding the wind project life time, longevity means more long-term costs and same capital cost. Because of the offshore converter station, the unavailability cost of MMC HVDC is more expensive than M^3C FFT, as well as the O&M expense. On the contrary, the power loss cost is lower and overall, the annual long-term costs are slightly higher for MMC HVDC around the crossover point. As a consequence, longer offshore wind power system life time is beneficial to M^3C FFT. From another angle, same as capacity factor, the project life time only relates to long-term costs. The difference is that higher capacity factor emphasises capital cost while longer project life time emphasises long-term costs. So an opposite trend can be seen in the sensitivity analysis plots.

Finally, the other type of wind turbine is considered. DFIG is adopted in the offshore wind power systems and the total cost against distance is re-plotted in Fig. 4.7 (e). From previous sections, it is indicated that there are multiple benefits for DFIG working at the fractional

frequency. And as can be observed, the crossover distance is now pushed way further to nearly 300 km. The root reason is that the percentage of the capital cost of wind turbine is so large that the saving is enormous in the cost difference analysis. Besides the saving on capital cost, DFIG also has reduction in unavailability, O&M and power loss costs.

4.7 Summary

This chapter has presented a detailed cost analysis and comparison between MMC and M^3C for offshore wind power transmission. Both technologies have their pros and cons and it is of significant importance to figure out which one is more cost-effective and under what circumstances. It is also vital to study the impact of various parameters on the analysis result. The economic-analysis method has been introduced as well as the cost decomposition of the total cost. Capital cost, unavailability cost, O&M cost and power loss cost have been discussed in details respectively. The cost analysis has shown that regardless of the transmission method, almost half of the overall cost is spent on wind turbine initial investment. Taking up around 20% of the total cost, O&M cost is the second largest decisive element in the analysis. Results from the first case have shown that M^3C FFT is a very promising choice for offshore wind power transmission at several hundred MW rating and at medium transmission distance. It has been found that three major factors that hampering it from being cost-effective are: costly submarine AC cable, more power loss compared to DC cable and larger offshore transformer station. For MMC HVDC, the offshore rectifier station is the main negative factor. It has expensive capital cost, higher unavailability rate, difficult maintenance compared to onshore station and extra power loss. However, a magnificent merit is the DC cable, with lower price, no reactive power compensation need and less power loss, making MMC HVDC the optimal solution for long distance transmission.

One constraint of the study is that the outcome of the cost analysis relies on the parameters. Consequently, sensitivity analysis has been carried out to provide insights to the impacts of parameter variation on the economical transmission distance. It has been found that discount rate, capacity factor and offshore wind energy price all have descending trend when the parameter increases, while longer wind power system life time results in farther crossover distance between the two technologies. Some parameters are more sensitive than others in terms of the impact on economical transmission distance range. Energy price and capacity factor have larger influence but discount rate and project life time are less decisive. In addition, DFIG has found to be very suitable for M^3C FFT, the economic advantage can be maximised and the cost-effective range is extended to almost 300 km.

CHAPTER 5 SMALL SIGNAL MODEL OF M^3C FOR FRACTIONAL FREQUENCY TRANSMISSION SYSTEM

5.1 Introduction

Offshore wind power develops rapidly in recent years. Its penetration keeps growing and the market witnesses increasing investments and a decrease of product prices [5]. In 2018, Europe added an additional capacity of 2.6 GW and the accumulated offshore wind capacity has reached 18.5 GW. Away from the population centre, offshore wind is advantageous not only because of not taking up city land, but also due to higher wind speed and suitability for large-scale exploitation. Traditional HVAC is merely capable of short distance offshore transmission nowadays, but after years of exploitation, the development of near-coast wind power is close to saturation, pushing the future offshore wind farms further offshore. But offshore wind farms may not be too far away from the coast, as construction and maintenance would become rather difficult and expensive. In that case the project profit return ability is doubtful and the payback of the investment is not optimistic. The FFT is proposed to overcome the HVAC cable shortcoming. And based on the economic analysis in Chapter 4, it has been found that M^3C FFT is a cost-effective technology for medium distance offshore wind power transmission, which is likely to cover most future offshore wind farms.

The core component of a FFTS is the frequency changer, or the AC/AC converter M^3C. In M^3C, there is no DC link so quantities at two frequencies from both AC sides couple together in nine arms of the converter. Such operation is not common and therefore it is of significant importance to gain understanding of dynamics of the M^3C and its impact on the power grids.

However, to the best knowledge of the author, a small signal model of M^3C does not exist in the literature yet. The main contribution of this chapter is to develop a small signal model of the M^3C for FFTS which can be used for power system small signal stability study as well as controller design. Quantities at frequencies of both AC sides mingling in the M^3C are isolated and decoupled. The model is developed in DQ frame and it can be interlinked simply with the external AC systems and the control system. It is shown that the model is with a reduced number of variables but maintains satisfactory accuracy. Also, a small signal analysis is conducted when controller parameters or sub-module capacitance varies.

5.2 Arm Voltage and Current Relations

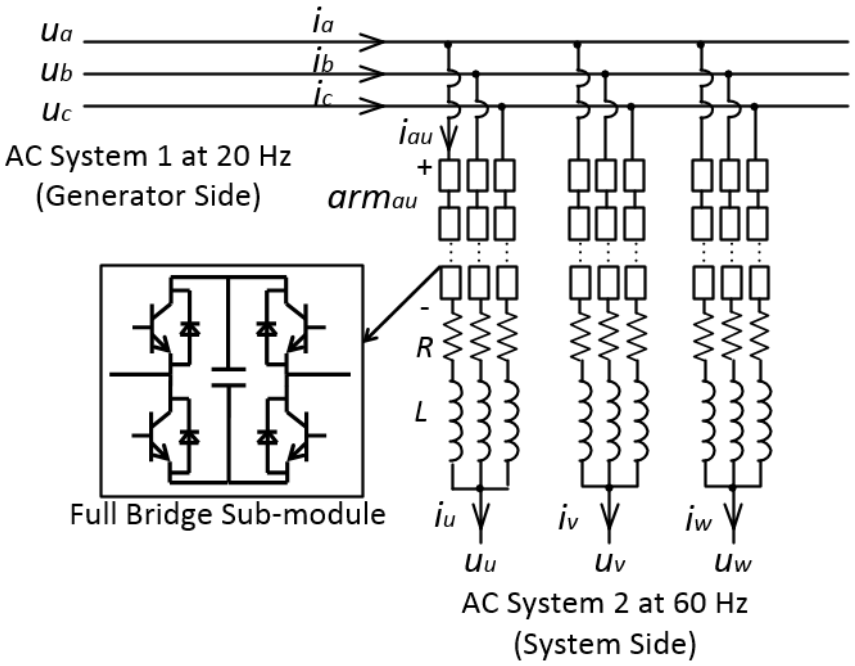

Fig. 5.1 Schematic diagram of a M^3C.

Fig. 5.1 depicts a M^3C connecting two AC systems. The fundamental operating principle of M^3C has been introduced in Subsection 3.2. The quantities of the fractional frequency side are denoted by the subscripts *a, b, c* and the quantities of the grid side are denoted by *u, v, w*. An

arm resistor is added to represent the internal converter losses. Recall the equations of arm current and arm switching function as (5.1) and (5.2). At steady state, the phase current is equally spread into the three arms connected to that phase. For example, the 20 Hz components of the arm currents i_{au}, i_{av} and i_{aw} have the same amplitude and it equals to one third of the phase current i_a. Similarly, the 60 Hz components of the arm currents i_{au}, i_{bu} and i_{cu} have the same amplitude and it equals to one third of the phase current i_u.

$$i_{au} = I_a \sin(\omega_1 t + \beta_1) + I_u \sin(\omega_3 t + \beta_3) \tag{5.1}$$

$$S_{au} = \frac{E_a}{U_{DC}} \sin(\omega_1 t + \alpha_1) + \frac{E_u}{U_{DC}} \sin(\omega_3 t + \alpha_3) \tag{5.2}$$

In the model, current harmonics are not taken into consideration due to the reasons below:

1) By carefully selecting the values of circuit components, for example capacitances and arm inductances, the magnitudes of the current harmonics can be kept to a negligible level [108, 109].

2) The small signal model focuses on the external characteristics of the M^{3}C. For circulating currents flowing within the converter, their influence on the outer AC systems can be neglected.

3) Under AC system unbalance, current harmonics may be salient. But such situation is out of the scope of this study.

Considering a single sub-module in an arm, the switching signal S_{armi} (=1, 0, -1) determines the operation mode of the i^{th} sub-module. When the switching signal equals to 1, the sub-module is positively inserted with the capacitor voltage u_{dc}. Contrarily, $-u_{dc}$ will be inserted if the signal is -1. And the sub-module will be bypassed if the signal is 0. Refer i_{arm} to the

arm current and *C* is the sub-module capacitance. The current equation of one sub-module and one arm can be given by (5.3) and (5.4):

$$S_{armi}\, i_{arm} = C\, \frac{du_{dc}}{dt} \tag{5.3}$$

$$\begin{aligned} \sum_{i=1}^{N} S_{armi}\, i_{arm} &= N\, C\, \frac{du_{dc}}{dt} \\ n\ i_{arm} &= N\, C\, \frac{du_{dc}}{dt} \end{aligned} \tag{5.4}$$

Under normal operation, sub-modules are inserted in the same direction. Therefore, the magnitude of *n* is the inserted number of sub-modules, with $n > 0$ indicating that sub-modules are positively inserted and $n < 0$ indicating that sub-modules are negatively inserted. Define the arm switching function $S_{arm} = n/N$, Equation (5.4) becomes:

$$S_{arm}\ i_{arm} = C\, \frac{du_{dc}}{dt} \tag{5.5}$$

Equation (5.5) gives the current relation of a M^3C arm, and the voltage relation can be expressed by the following Equation (5.6), where u_{arm} represents the arm voltage:

$$u_{arm} = N\, S_{arm}\, u_{dc} \tag{5.6}$$

Within an arm, the sub-module voltage balancing method is the same for MMC HVDC [79], which has been widely researched and tested [110, 111]. In this study, it is assumed that the sub-modules voltage balancing control performs satisfactorily. Equation (5.5) and (5.6) assume that the sub-module voltages are balanced at steady state. Also, the focus of this research is to develop a compact and manageable M^3C small signal model. But multilevel converters for transmission applications contain up to several hundred sub-modules, making it mathematically inefficient to consider dynamics on every single sub-module for a small signal model.

5.3 Small Signal Model of M³C

5.3.1 Dynamics of the Capacitor Voltage

The ABC quantities are transformed into DQ components using Park transformation. The transformation matrix is denoted as *T*:

$$T = \frac{2}{3}\begin{bmatrix} cos(\omega t) & cos(\omega t - \frac{2}{3}\pi) & cos(\omega t + \frac{2}{3}\pi) \\ -sin(\omega t) & -sin(\omega t - \frac{2}{3}\pi) & -sin(\omega t + \frac{2}{3}\pi) \end{bmatrix} \tag{5.7}$$

When frequency equals to 20 Hz, $\omega = \omega_1$, and when frequency is 60 Hz, $\omega = \omega_3$. The dynamic phasors of the quantities in DQ frame can be expressed as a function of the magnitude and the phase angle in ABC frame. For example:

$$\begin{cases} E_{d20} = E_a sin\alpha_1 \\ E_{q20} = -E_a cos\alpha_1 \\ I_{d20} = I_a sin\beta_1 \\ I_{q20} = -I_a cos\beta_1 \end{cases} \tag{5.8}$$

Substitute (5.1) and (5.2) into (5.5), the DC component of the capacitor voltage is extracted and expressed as:

$$C \cdot \dot{U}_{dc\_0} = \frac{E_a I_a}{U_{DC}}\cos(\alpha_1 - \beta_1) + \frac{E_u I_u}{U_{DC}}\cos(\alpha_3 - \beta_3) \tag{5.9}$$

Express the right side of Equation (5.9) with DQ components and rearrange the equation, the differential equation of U_{dc_0} can be given by:

$$\dot{U_{dc\_0}} = \frac{1}{2U_{DC} \cdot C}\left(E_{q20}I_{q20} + E_{d20}I_{d20} + E_{q60}I_{q60} + E_{d60}I_{d60}\right) \tag{5.10}$$

Similarly, the 40 Hz components of the capacitor voltage (transformed into DQ frame) are modelled by the following Equation (5.11) and (5.12). Detailed derivation can be found in Appendix C.

$$\dot{U_{dc\_d2}} = 2\omega_1 U_{dc\_q2} - \frac{1}{2U_{DC} \cdot C}\left(E_{q20}I_{q20} - E_{d20}I_{d20}\right) \tag{5.11}$$

$$\dot{U_{dc\_q2}} = -2\omega_1 U_{dc\_d2} + \frac{1}{2U_{DC} \cdot C}\left(E_{d20}I_{q20} + E_{q20}I_{d20}\right) \tag{5.12}$$

Only the 40 Hz capacitor voltage ripple is considered and higher order components are neglected in this model, as the 40 Hz component has the largest magnitude and dominates in voltage ripples. It is going to be further discussed and verified by the time domain simulation in Section 5.4. In situations where higher order voltage ripples are preferable to be included, similar approach can be applied to model ripples (at 80, 120 Hz…) easily. But in this model:

$$u_{dc} \approx U_{dc\_0} + U_{dc\_2}\, sin(2\omega_1 t + \theta_2) \tag{5.13}$$

where U_{dc_2} and θ_2 are the magnitude and the phase angle of the 40 Hz capacitor voltage ripple.

5.3.2 Dynamics of the AC Current

Substitute (5.2) and (5.13) into (5.6), the 20 Hz and 60 Hz arm voltages can be calculated as:

$$\begin{cases} U_{arm_{20a}} = \dfrac{NE_a U_{dc_0}}{U_{DC}} sin(\omega_1 t + \alpha_1) + \dfrac{NU_{dc\_2}E_a}{2U_{DC}} cos(\omega_1 t + \theta_2 - \alpha_1) \\ U_{arm\_60u} = \dfrac{E_u U_{dc\_0}}{U_{DC}} \sin(\omega_3 t + \alpha_3) \end{cases} \tag{5.14}$$

Rewriting (5.14) in DQ components yields:

$$\begin{cases} U_{arm\_20d} = \dfrac{NU_{dc\_0}}{U_{DC}} E_{d20} + \dfrac{N}{2U_{DC}} (U_{dc\_q2} E_{q20} + U_{dc\_d2} E_{d20}) \\ U_{arm\_20q} = \dfrac{NU_{dc\_0}}{U_{DC}} E_{q20} - \dfrac{N}{2U_{DC}} (U_{dc\_d2} E_{q20} - U_{dc\_q2} E_{d20}) \end{cases} \tag{5.15}$$

$$\begin{cases} U_{arm\_60d} = \dfrac{U_{dc\_0}}{U_{DC}} E_{d60} \\ U_{arm\_60q} = \dfrac{U_{dc\_0}}{U_{DC}} E_{q60} \end{cases} \tag{5.16}$$

Apply Kirchhoff's law to M^{3}C, equations at 20 Hz and 60 Hz can be given by:

$$\begin{cases} e_a = U_{arm\_20a} + L \cdot \dot{\imath}_{au\_20} + R \cdot i_{au\_20} \\ 0 = U_{arm\_60u} + L \cdot \dot{\imath}_{au\_60} + R \cdot i_{au\_60} + e_u \end{cases} \tag{5.17}$$

Again transform voltage equations into DQ coordinate. The differential equations of the AC currents are given as:

$$\begin{cases} \dot{I_{d20}} = \dfrac{1}{L} U_{d20} - \dfrac{R}{L} I_{d20} + \omega_1 I_{q20} - \dfrac{1}{L} U_{arm\_20d} \\ \dot{I_{q20}} = \dfrac{1}{L} U_{q20} - \dfrac{R}{L} I_{q20} - \omega_1 I_{d20} - \dfrac{1}{L} U_{arm\_20q} \end{cases} \tag{5.18}$$

$$\begin{cases} \dot{I_{d60}} = -\dfrac{1}{L} U_{d60} - \dfrac{R}{L} I_{d60} + \omega_3 I_{q60} - \dfrac{1}{L} U_{arm\_60d} \\ \dot{I_{q60}} = -\dfrac{1}{L} U_{q60} - \dfrac{R}{L} I_{q60} - \omega_3 I_{d60} - \dfrac{1}{L} U_{arm\_60q} \end{cases} \tag{5.19}$$

To combine, the M^{3}C itself can be modelled with the state and input variables below:

$$x_{m3c} = [U_{dc\_0}, U_{dc\_d2}, U_{dc\_q2}, I_{d20}, I_{q20}, I_{d60}, I_{q60}]$$

$$u_{m3c} = [E_{d20}, E_{q20}, E_{d60}, E_{q60}, \omega_1, \omega_3, U_{d20}, U_{q20}, U_{d60}, U_{q60}]$$

5.3.3 Control System for the M^{3}C

The control method of the M^{3}C in this study adopts the widely used vector control. The generator side of the M^{3}C is responsible for controlling active power and the system side of the M^{3}C is responsible for controlling capacitor voltage. The Q axis of the outer loop can be used to control voltage or reactive power. For the sake of simplicity, the Q axis current reference is set to zero to maximise the active power transmitting capability. The control diagram is as shown in Fig. 5.2.

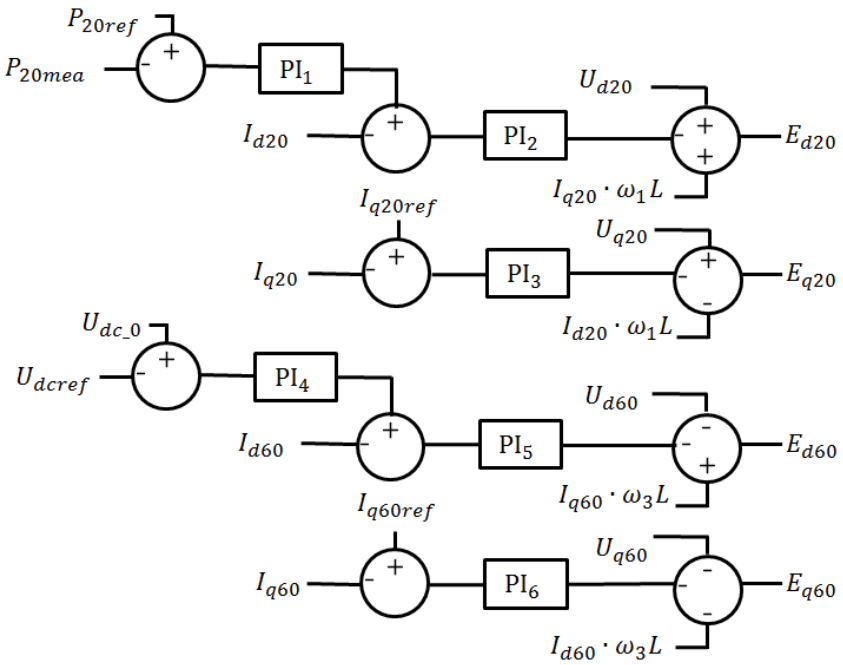

Fig. 5.2 Vector control topology of the M^{3}C.

As the vector control algorithm has been well documented in the literature [47, 51]. The differential equations are given here directly:

$$\dot{x_1} = P_{20\_ref} - P_{20mea} \tag{5.20}$$

$$\dot{x_2} = k_{p1}P_{20\_ref} - k_{p1}P_{20mea} + k_{i1}x_1 - I_{d20} \tag{5.21}$$

$$\dot{x_3} = I_{q20\_ref} - I_{q20} \tag{5.22}$$

$$\dot{x_4} = U_{dc\_0} - U_{dc\_ref} \tag{5.23}$$

$$\dot{x_5} = k_{p4}U_{dc\_0} - k_{p4}U_{dc\_ref} + k_{i4}x_4 - I_{d60} \tag{5.24}$$

$$\dot{x_6} = I_{q60\_ref} - I_{q60} \tag{5.25}$$

The PLL provides angle references and its dynamics should be included. The modelling method is the same as proposed in [112]. Four variables are added to model two PLLs at both 20 Hz and 60 Hz sides. x_7 and x_8 are the time integration of the Q axis voltages. And x_{pll} represents the output of the PLL.

$$\dot{x_7} = U_{q20} \tag{5.26}$$

$$\dot{x_{pll20}} = -k_{p-pll}U_{q20} - k_{i-pll}x_7 \tag{5.27}$$

$$\dot{x_8} = U_{q60} \tag{5.28}$$

$$\dot{x_{pll60}} = -k_{p-pll}U_{q60} - k_{i-pll}x_8 \tag{5.29}$$

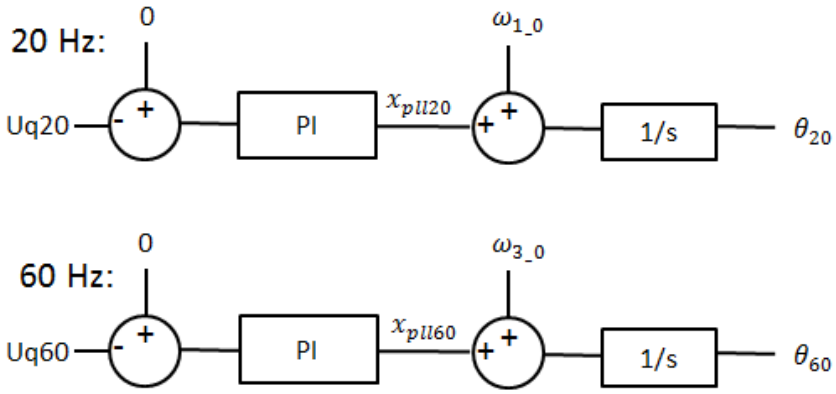

Fig. 5.3 Control diagram of PLL at 20 Hz and 60 Hz.

The measurement and calculation delay is modelled by a first order low pass filter for the power signal. It also filters the high frequency fluctuation. The differential equation is given by the following Equation (5.30), where P_{20} is the power transmitted from the 20 Hz side, which is a function related to $U_{d20,}I_{d20}, U_{q20}$ and I_{q20}. P_{20mea} is the measured power at the 20 Hz side, and T_{mea} is the first order time constant.

$$\dot{P_{20mea}} = \frac{P_{20}}{T_{mea}} - \frac{P_{20mea}}{T_{mea}} \tag{5.30}$$

In total, the combined control system has the following state and input variables:

$$x_{ctrl} = [x_1, x_2, x_3, x_4, x_5, x_6, x_7, x_{pll20}, x_8, x_{pll60}, P_{20mea}] \tag{5.31}$$

$$\begin{aligned} &u_{ctrl} \\ &= [U_{dc_0}, I_{d20}, I_{q20}, I_{d60}, I_{q60}, U_{d20}, U_{q20}, U_{d60}, U_{q60}, P_{20ref}, I_{q20ref}, U_{dcref}, I_{q60ref}] \end{aligned} \tag{5.32}$$

5.3.4 Combined System for the Small Signal Model

To get the small signal model of the complete system, the abovementioned two systems: the M^{3}C system and its control system are merged. In the first system, $E_{d20}, E_{q20}, E_{d60}$ and E_{q60} are the outputs from the vector control in the second system. And ω_1 and ω_3 are the outputs from the PLLs. $U_{d20}, U_{q20}, U_{d60}$ and U_{q60} provide interfaces with the 20 Hz and 60 Hz side AC systems respectively. The block diagram of the combined system is plotted in Fig 5.4 where variable flows indicate how sub-systems are interconnected.

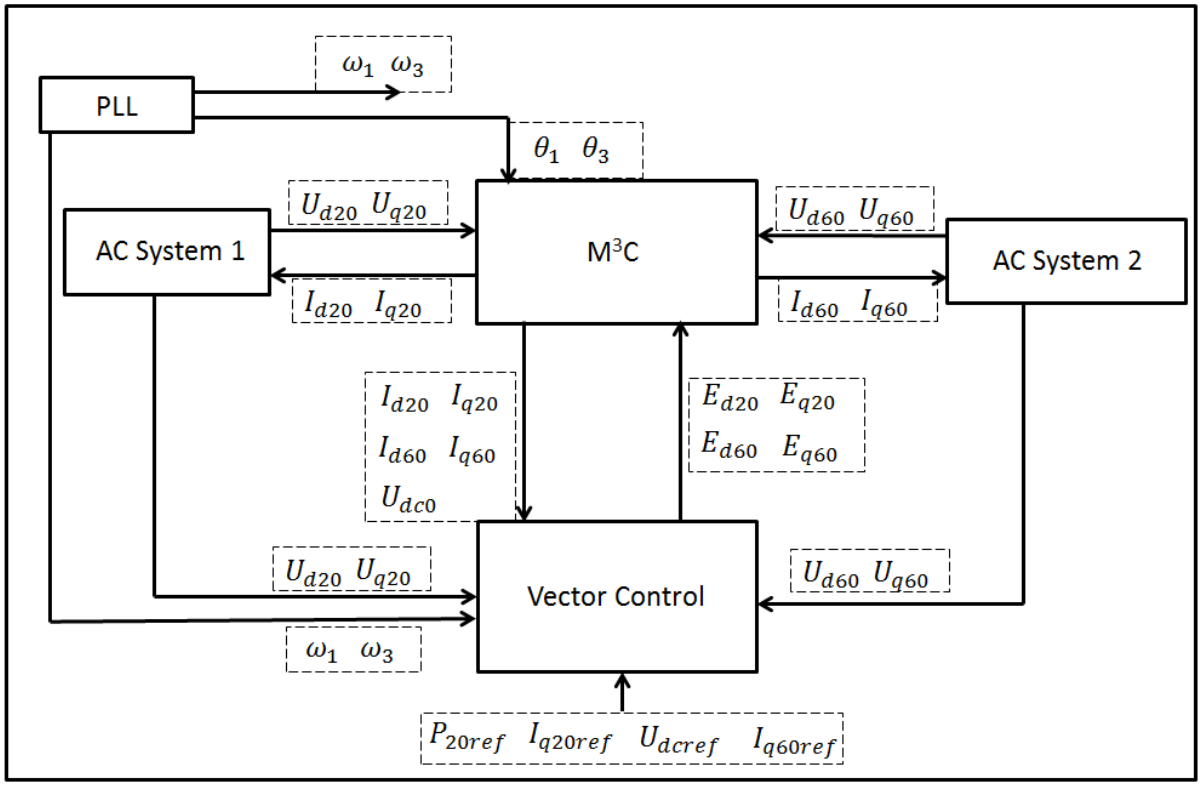

Fig. 5.4 State-space model of the combined M^{3}C system.

The combined model can be expressed in the form of:

$$\dot{x} = Ax + Bu \tag{5.33}$$

where the expression of the matrix *A* and *B* is given as:

A =

$$
\begin{bmatrix}
 & & & \frac{E_{d20}}{2U_{DC}\cdot C} & \frac{E_{q20}}{2U_{DC}\cdot C} & \frac{E_{d60}}{2U_{DC}\cdot C} & \frac{E_{q60}}{2U_{DC}\cdot C} & & & & & & & \\
 & & 2\omega_1 & \frac{E_{q20}}{2U_{DC}\cdot C} & -\frac{E_{d20}}{2U_{DC}\cdot C} & & & & & & & & & \\
 & -2\omega_1 & & \frac{E_{q20}}{2U_{DC}\cdot C} & \frac{E_{d20}}{2U_{DC}\cdot C} & & & & & & & & & \\
-\frac{NE_{d20}}{LU_{DC}} & -\frac{NE_{d20}}{2LU_{DC}} & -\frac{NE_{q20}}{2LU_{DC}} & -\frac{R}{L} & \omega_1 & & & & & & & & & \\
-\frac{NE_{q20}}{LU_{DC}} & \frac{NE_{q20}}{2LU_{DC}} & -\frac{NE_{d20}}{2LU_{DC}} & -\omega_1 & -\frac{R}{L} & & & & & & & & & \\
-\frac{NE_{d60}}{LU_{DC}} & & & & & -\frac{R}{L} & \omega_3 & & & & & & & \\
-\frac{NE_{q60}}{LU_{DC}} & & & & & -\omega_3 & -\frac{R}{L} & & & & & & & \\
 & & & & & & & & & & & & -1 & \\
 & & & -1 & & & & k_{i1} & & & & & -k_{p1} & \\
 & & & & -1 & & & & & & & & & \\
1 & & & & & & & & & & & & & \\
k_{p4} & & & & & -1 & & & k_{i4} & & & & & \\
 & & & & & & -1 & & & & & & & \\
 & & & & & & & & & & -k_{i-pll} & & & \\
 & & & & & & & & & & & -k_{i-pll} & & \\
 & & \frac{9U_{d20}}{2T_{fil}} & \frac{9U_{q20}}{2T_{fil}} & & & & & & & & & -\frac{1}{T_{mea}} &
\end{bmatrix}
$$

B=

$$
\begin{bmatrix}
 & & & & & & & & \\
\frac{1}{L} & & & & & & & & \\
 & \frac{1}{L} & & & & & & & \\
 & & -\frac{1}{L} & & & & & & \\
 & & & -\frac{1}{L} & & & & & \\
 & & & & 1 & & & & \\
 & & & & k_{p1} & & & & \\
 & & & & & 1 & & & \\
 & & & & & & -1 & & \\
 & & & & & & -k_{p4} & & \\
 & & & & & & & -1 & \\
 & 1 & & & & & & & \\
 & -k_{p-pll} & & & & & & & \\
 & & & 1 & & & & & \\
 & & & -k_{p-pll} & & & & &
\end{bmatrix}
$$

The small signal model can be derived by linearizing (5.33). The final model is of 18 orders and all the state variables are listed in (5.34) with an explanation given in Table 5.1. Input variables are listed in (5.35) and the explanation can be found in Table 5.2.

$$\Delta x = [\Delta U_{dc\_0}, \Delta U_{dc\_d2}, \Delta U_{dc\_q2}, \Delta I_{d20}, \Delta I_{q20}, \Delta I_{d60}, \Delta I_{q60}, \quad (5.34)$$

$$\Delta x_1, \Delta x_2, \Delta x_3, \Delta x_4, \Delta x_5, \Delta x_6, \Delta x_7, \Delta x_{pll20}, \Delta x_8, \Delta x_{pll60}, \Delta P_{20mea}]$$

$$\Delta u = [\Delta U_{d20}, \Delta U_{q20}, \Delta U_{d60}, \Delta U_{q60}, \Delta P_{20ref}, \Delta I_{q20ref}, \Delta U_{dcref}, \ \Delta I_{q60ref}] \quad (5.35)$$

Table 5.1 Explanation of the state variables

Sub-system		Meaning	State variable
M^3C	Sub-module capacitor voltage	DC component	U_{dc_0}
		40 Hz ripple D component	U_{dc_d2}
		40 Hz ripple Q component	U_{dc_q2}
	Arm current	20 Hz current D component	I_{d20}
		20 Hz current Q component	I_{q20}
		60 Hz current D component	I_{d60}
		60 Hz current Q component	I_{q60}
Control system	Vector control outer loop	20 Hz side outer loop controller	x_1
		60 Hz side outer loop controller	x_4
	Vector control inner loop	20 Hz side inner loop on D axis	x_2
		20 Hz side inner loop on Q axis	x_3
		60 Hz side inner loop on D axis	x_5
		60 Hz side inner loop on Q axis	x_6
	PLL AC system 1	20 Hz side PLL intermediate variable	x_7
		Output of 20 Hz side PLL	x_{pll20}
	PLL AC system 2	60 Hz side PLL intermediate variable	x_8
		Output of 60 Hz side PLL	x_{pll60}

Table 5.2 Explanation of the input variables

Sub-system	Meaning	Input variable
External AC Systems	AC system 1 voltage D axis component	U_{d20}
	AC system 1 voltage Q axis component	U_{q20}
	AC system 2 voltage D axis component	U_{d60}
	AC system 2 voltage Q axis component	U_{q60}
Vector control reference inputs	20 Hz D axis reference input: active power	P_{20ref}
	20 Hz Q axis reference input: reactive current	I_{q20ref}
	60 Hz D axis reference input: capacitor voltage	U_{dcref}
	60 Hz Q axis reference input: reactive current	I_{q60ref}

5.4 Model Verification and Stability Analysis

To validate the proposed small signal model, the combined model discussed in Section 5.3 is implemented in MATLAB/Simulink. Also, a non-linear detailed model of M^3C is developed in RTDS for EMT simulation, which has been introduced in Chapter 3.

In RTDS, The actual measured sub-module voltage is plotted in Fig. 5.5, together with the sub-module voltage added up only by the DC component and the 40 Hz ripple. It can be seen from the figure that the 40 Hz component takes up the largest magnitude of the ripples and two curves match closely. Thus, the discrepancy brought by neglecting high order capacitor voltage ripples is acceptable. If required, the proposed approach is capable of modelling high order ripple components.

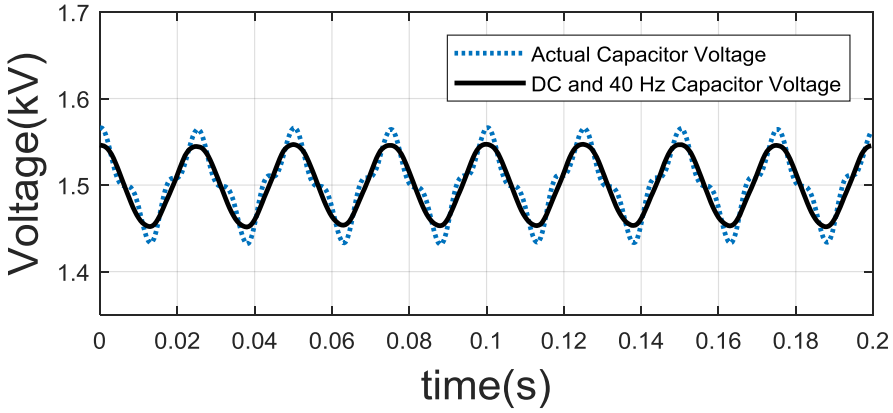

Fig. 5.5 Measured sub-module capacitor voltage versus capacitor voltage with only DC component and the 40 Hz ripple.

The switching frequency mainly affects the harmonics of the converter, and harmonics has a range of negative influences on stability, which will be thoroughly studied in Chapter 6. The higher the switching frequency, the more sinusoidal the output waveform would be. If the switching frequency is too low, the size of associated components such as the inductors, transformers and capacitors would increase to maintain an acceptable level of harmonics. However, higher switching frequency would lead to higher switching loss of the converter and therefore lower efficiency. As a trade-off, switching frequency is normally chosen at kHz level.

5.4.1 Dynamic Response of Step Change on Active Power Reference

At the initial state, 30 MW of active power is transmitted from the 20 Hz side to the 60 Hz side. At t = 0.4 s, a step change of P_{20ref} is applied from 30 MW to 32 MW. The dynamic response of the developed small signal model is compared to that of the detailed time domain simulation. Results from the small signal model and the time domain simulation are plotted together in Fig. 5.6. As is shown, the active power at 20 Hz side (Fig. 5.6 (a)) and the capacitor voltage (Fig. 5.6 (b)) show great consistency. For AC current waveforms (Fig. 5.6 (c)

- Fig. 5.6 (f)), overall there is a good agreement, except that the detailed simulation model contains high frequency fluctuations while the theoretical small signal model only represent their mean values. The step change dynamic response validates the proposed small signal model for M^3C. The PI control parameters are shown in Appendix A, and tuning of PI controller has been covered in Section 3.4. PI parameters are chosen based on two main considerations: Steady state and transient performance and stability. PI parameters should be chosen so that the system has negligible steady state error, small overshoot and short settling time. For example in Fig. 5.6, the active power is able to reach the new reference within 0.1s, without obvious overshoot and with negligible steady state error. Also, the PI parameters should be within certain ranges to ensure system stability. Otherwise, the system would be subject to instability or become oscillatory during transient period.

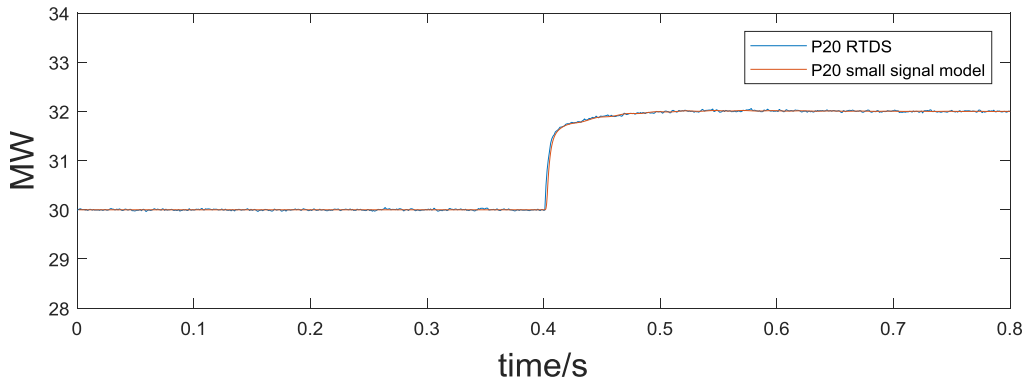

(a) Active power at 20 Hz side.

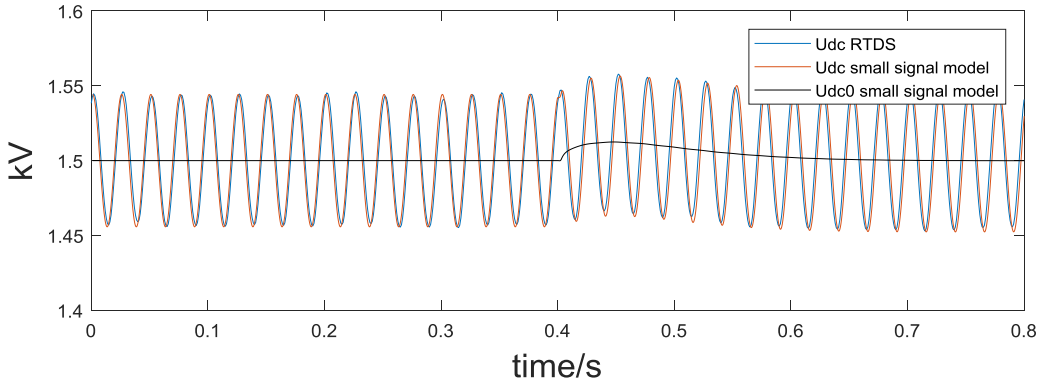

(b) Capacitor voltage (DC+40 Hz superposition) and DC component only.

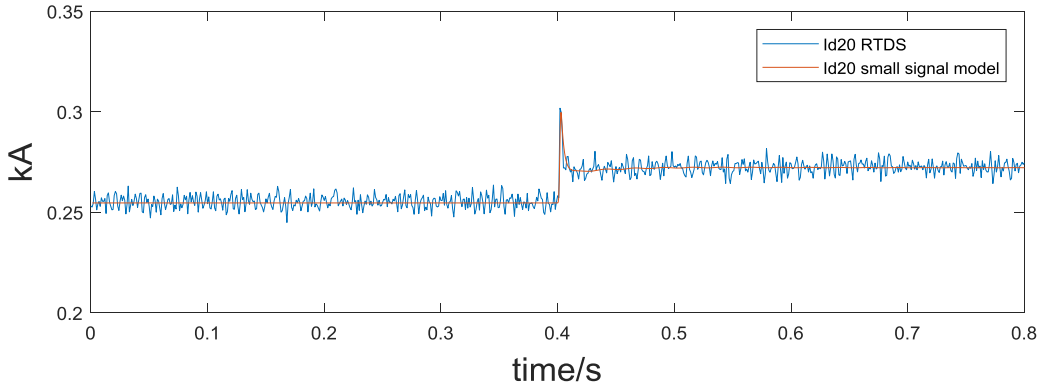

(c) D axis arm current of 20 Hz side.

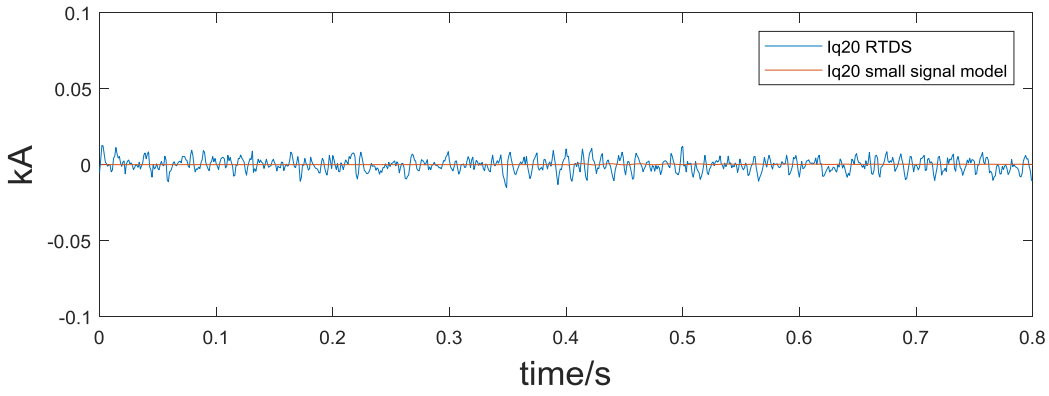

(d) Q axis arm current of 20 Hz side.

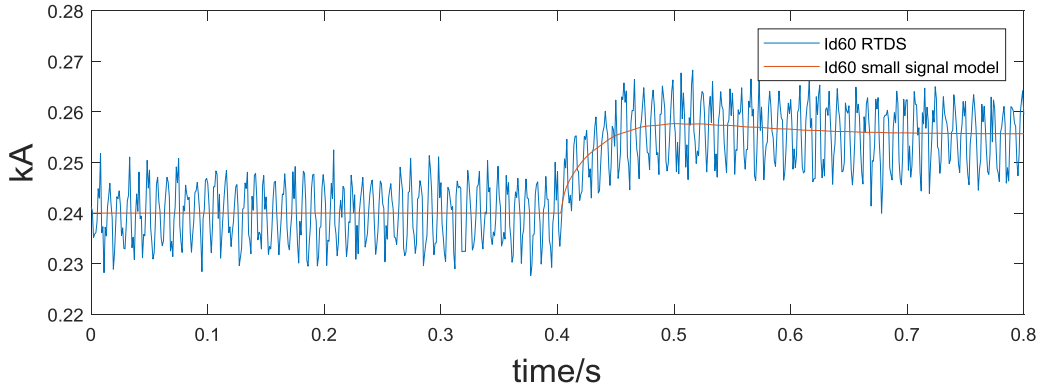

(e) D axis arm current of 60 Hz side.

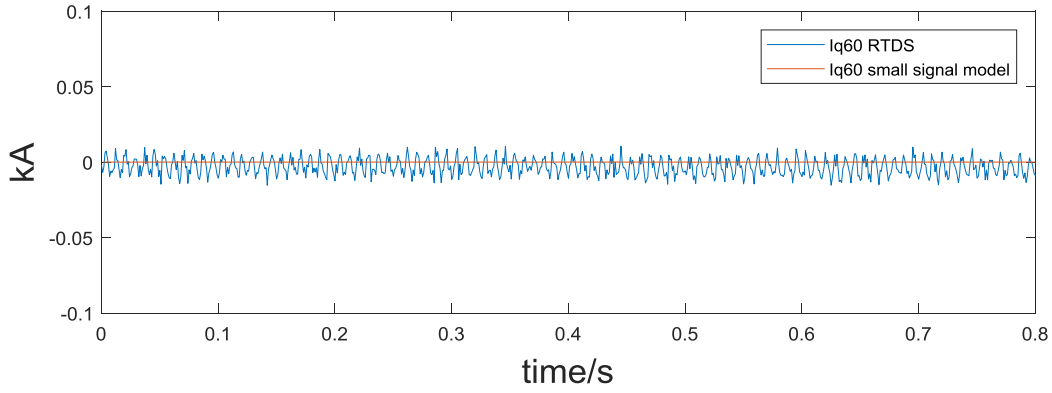

(f) Q axis arm current of 60 Hz side.

Fig. 5.6 Step change response of the small signal model (red line) and detailed EMT model (blue line).

5.4.2 Influence of the Outer Loop Controller

The developed small signal model is helpful on the selection of controller parameters. In this subsection, the outer loop PI controller parameter k_{i1} is studied. The root locus of the related modes is plotted in Fig. 5.7. As k_{i1} increases, the eigenvalues move towards the right half of the complex plane and the modes eventually become unstable. In RTDS, a step change of k_{i1} from 15 to 150 is applied at t = 0.25s. Since this controller is responsible for controlling the

active power at the 20 Hz side, the waveform of the measured P_{20} is shown in Fig. 5.8. As can be observed, the system loses its stability and the active power begins to oscillate with a period of 0.0047s. According to the eigenvalue analysis, the oscillation period of this mode is calculated as $2\pi/\omega$ = 0.0048s, which highly agrees with the simulation result. Therefore, the effectiveness of the proposed model is again validated. It is shown that the increasing outer loop integral gain has a negative effect on the small signal stability and therefore it should be limited within a certain range.

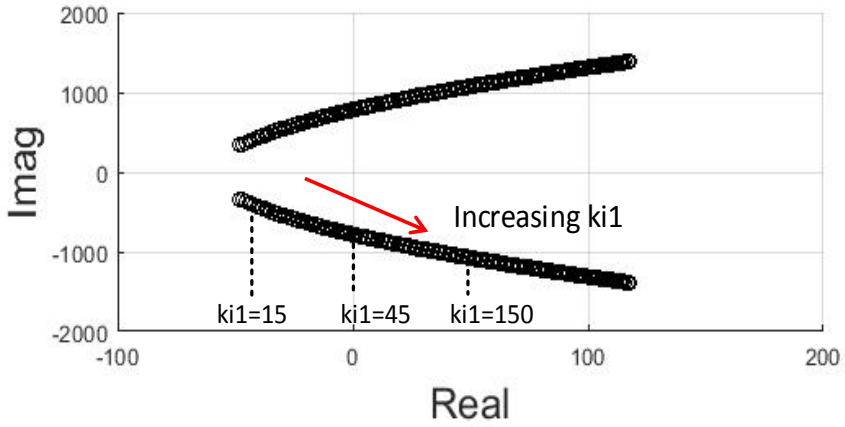

Fig. 5.7 Root locus of the related eigenvalues when k_i1 increases.

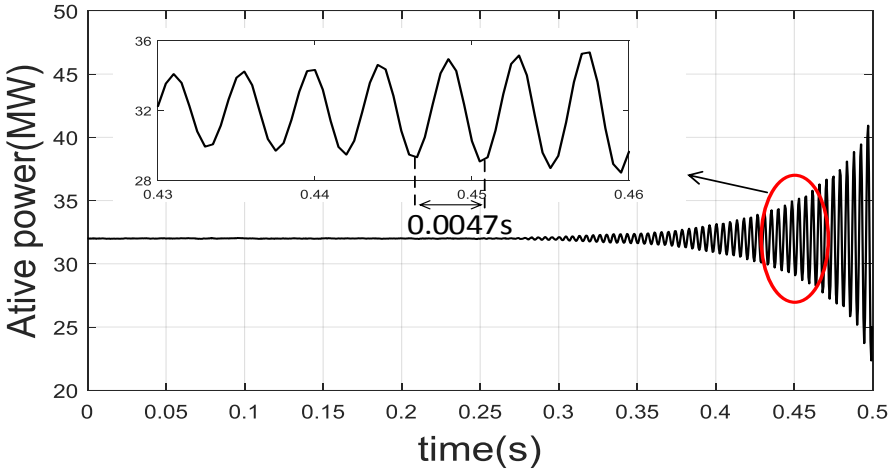

Fig. 5.8 Active power at 20 Hz side when step change is applied to k_i1.

5.4.3 Influence of the PLL

In this subsection, the control parameters of the PLL are analysed. If the eigenvalue of a mode is denoted as $\lambda = \sigma \pm j\omega$, the damping ratio of the mode is defined as $\xi = -\sigma/\sqrt{\sigma^2 + \omega^2}$. When the damping ratio is less than 5%, the mode is regarded as poorly damped. Fig. 5.9 plots the damping ratio of the mode related to PLL as the proportional gain grows from 0 to 2. It is shown that the damping ratio increases and then remains at 1. This mode has poor damping when k_{ppll} < 0.06. In addition, the root locus is plotted in Fig. 5.10 when k_{ppll} varies from 0 to 20 and k_{ipll} varies from 1 to 20. When k_{ppll} raises, the eigenvalues firstly move towards and then get onto the real axis. After that, one eigenvalue moves further away from the imaginary axis while the other gets closer to the right half pane. As a result, if k_{ppll} adopts a large value, the system may be vulnerable to small signal instability. For the integral gain of PLL k_{ipll}, the mode trajectory in the root locus plot is more straightforward. As the integral gain increases, the eigenvalue gets more negative and therefore the small signal stability enhances.

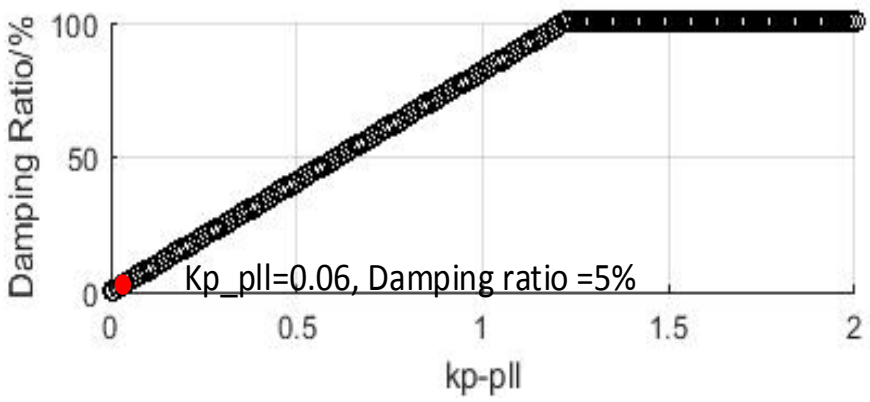

Fig. 5.9 Damping ratio as PLL proportional gain grows.

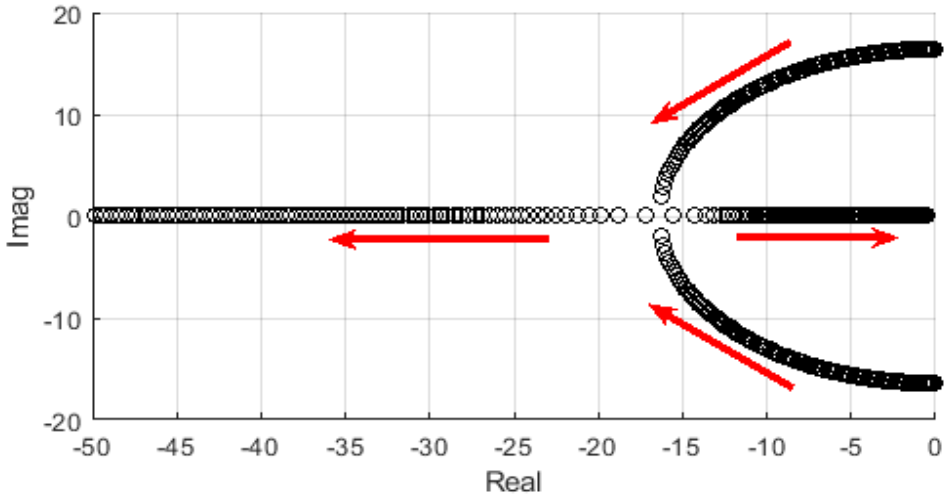

(a) Root locus when kp_pll increases.

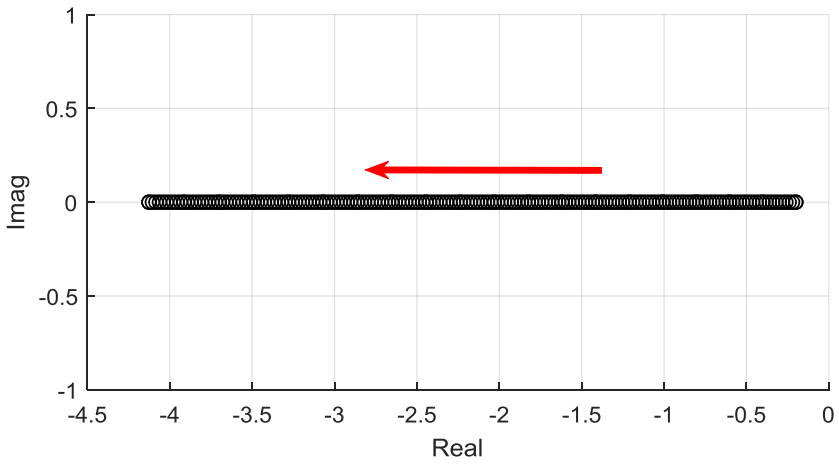

(b) Root locus when ki_pll increases.

Fig. 5.10 Root locus when kp_pll (a) and ki_pll (b) increase.

5.4.4 Analysis of the Sub-module Capacitor Mode

The small signal stability of the mode related to the capacitor voltage ripple is analysed in this subsection. The damping ratio is shown against the sub-module capacitance. As is shown in Fig. 5.11, a larger value of the capacitor would result in poorer damping of the mode. In other small signal studies for instance for two-level VSC or MMC, capacitor ripples are often

omitted and it is assumed that the capacitor voltage is DC [113, 114]. However, the M^{3}C model proposed in this thesis takes into account the sub-module voltage ripples. Therefore, it is able to identify the possible poorly damped mode and the small signal analysis can help select the sub-module capacitance.

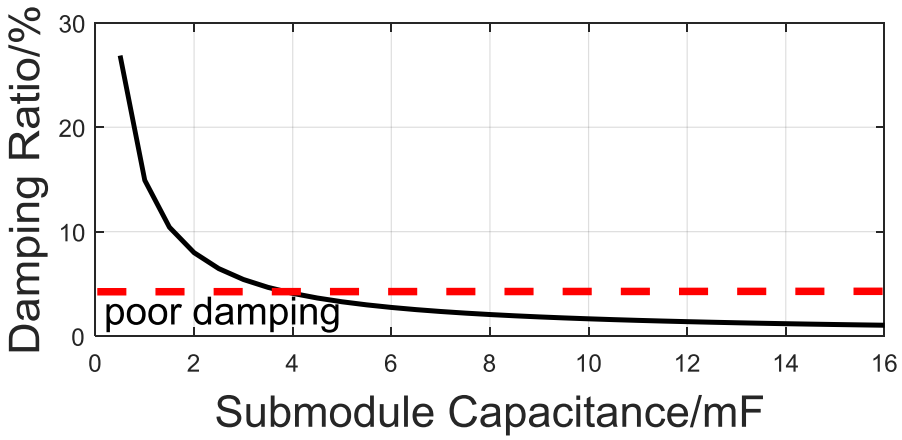

Fig. 5.11 Damping ratio of the mode related to capacitor ripple as sub-module capacitance increases.

5.5 Summary

As M^{3}C FFTS is one of the promising candidates for offshore wind power integration, there is need of a model to study its influence on the existing power systems. This chapter has developed a small signal model of M^{3}C providing easy interfaces with both the external AC systems and the control system. The dynamics of AC currents and the DC and ripple components on sub-module capacitor voltage have been considered. The control system includes dynamics of the outer and inner loop PI controllers, PLL controller and the measurement delay. The model provides insights to controller parameters and sub-module capacitance selection. It has been found that increasing the integral gain of the D axis outer loop control has an adverse effect and can induce power oscillation, while a larger integral

gain of the PLL improves the small signal stability. The choice of the proportional gain of the PLL should be within a certain range as the damping ratio can be poor when a very small gain is chosen but a very large gain pushes the related eigenvalue too close to the right-hand complex plane. Also, it has been found that the sub-module capacitance plays an important role in the capacitor ripple voltage mode. Damping ratio decreases as capacitance grows. Time domain simulation of a detailed EMT M^3C model has confirmed the correctness of the small signal model. The model is easy to implement and is beneficial to system stability study and controller design. But like any other small signal models, it has the limitation that the analysis only applies to small perturbation situations and is not suitable for large disturbance studies.

CHAPTER 6 HARMONIC ANALYSIS OF M^3C FOR OFFSHORE WIND POWER APPLICATION

6.1 Introduction

FFT is proven to be a promising technology for offshore wind power application and M^3C is the key component connecting the fractional frequency system to the normal frequency grid system. From the stability point of view, harmonic analysis is crucial for offshore wind power application. Locating in remote areas, offshore wind farm is often connected to a weak AC system and is prone to stability issues. It has been known that resonance and harmonic instability phenomena can occur when fast-switching devices interact with each other. Harmonic interaction has been recorded in an offshore wind farm system, leading to system shut-down and economic loss. With the fast-switching power electronics, oscillating voltage is induced on sub-module capacitors. Further interaction between the ripples and fundamental quantities at both generator side frequency and grid side frequency results in a complicated harmonic profile. Harmonic analysis is also crucial to prevent device damage and economic loss. In a MMC HVDC system, it is shown that circulating currents are in even orders, mainly in second order and they are confined within the converter. Besides, both the second order capacitor voltage and arm voltage are in negative sequence. However, the harmonic situation for a M^3C FFTS is still not clear. Undoubtedly, MMC and M^3C have similarities and they are often compared as counterparts. Nevertheless, without a DC link in M^3C, two frequencies intertwine in the converter, and hence the harmonic situation is fundamentally different from that in MMC. A detailed analysis of the harmonics is of significant importance. However,

although plenty of work on M^3C control has been carried out, limited attention has been paid to the harmonic analysis of M^3C.

In this chapter, a harmonic analysis method for M^3C is proposed. This method analyses how the harmonic components are generated. To begin with, the arm voltage and current relations are discussed. Then current harmonics at multiple frequencies are quantified. Based on the analysis, they are classified into three types. It is indicated that some current harmonics circulate within arms, some behave as positive-sequence fundamental current and the others are zero-sequence and can flow into AC systems. In addition, factors that have large impacts on harmonic magnitude are studied. Also, the influences of the harmonic components on M^3C itself and AC systems are discussed in a detailed manner. Analyses are conducted on sub-module capacitance and arm inductance selection. A zero-sequence current mitigation controller is implemented and tested for M^3C. The theoretical analysis is validated by the simulation results. The analysis provides insights to M^3C modelling and can serve for the development of new control methods.

6.2 Mathematical Model of M^3C

Similar to traditional HVAC transmission, a schematic diagram of an offshore wind FFTS is displayed in Fig. 6.1. The grid side frequency is chosen to be 60 Hz and the offshore wind farm generates power at 1/3 of the system frequency, which is 20 Hz. The voltage is stepped up by the transformers and then the wind power is transmitted onshore at fractional frequency. The M^3C station which locates onshore triples the frequency and delivers the power into the main grid.

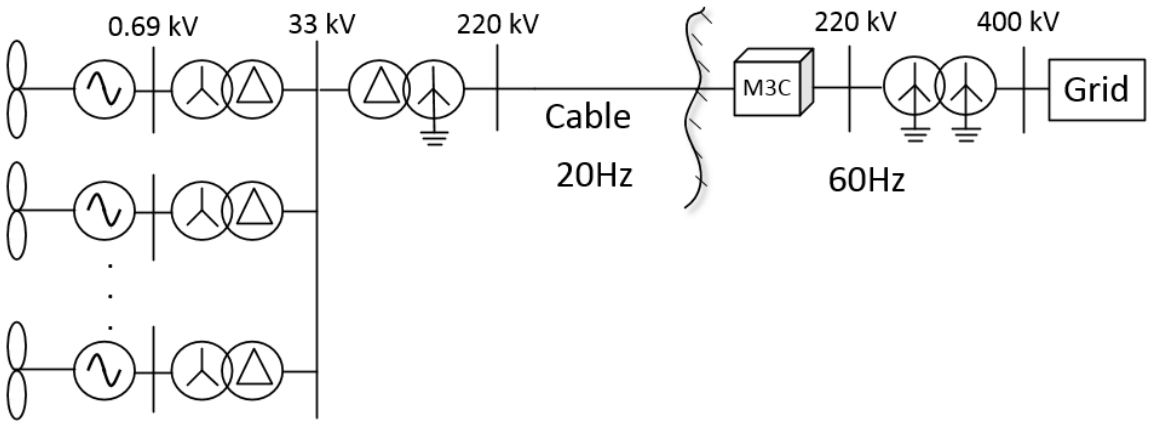

Fig. 6.1 The configuration of an offshore wind FFTS.

6.2.1 Arm Voltage and Current Expressions

Frequencies from the generator side ω_1 and the system side ω_3 couple in M^{3}C. At balanced steady state, the phase current is equally spread in three arms [74, 75]. For example, the arm current i_{au} contains one third of the phase current i_a, one third of the phase current i_u. When considering harmonics, the arm currents can be expressed as:

$$i_{arm} = \frac{1}{3} i_{20} + \frac{1}{3} i_{60} + i_{arm}^{harmonics} \tag{6.1}$$

where i_{20} and i_{60} are the phase currents of the fractional frequency side and the grid side. $i_{arm}^{harmonics}$ is the arm harmonics which will be discussed later in this section. When the harmonic current is insignificant, arm currents for all nine arms can be given as:

$$\begin{aligned} i_{au} &\approx \frac{1}{3} I_a \sin(\omega_1 t + \beta_1) + \frac{1}{3} I_u \sin(\omega_3 t + \beta_3) \\ i_{av} &\approx \frac{1}{3} I_a \sin(\omega_1 t + \beta_1) + \frac{1}{3} I_u \sin(\omega_3 t + \beta_3 - 120) \\ &\vdots \\ i_{cw} &\approx \frac{1}{3} I_a \sin(\omega_1 t + \beta_1 + 120) + \frac{1}{3} I_u \sin(\omega_3 t + \beta_3 + 120) \end{aligned} \tag{6.2}$$

where I_a, I_u, β_1 and β_3 are the magnitudes and phase angles of the generator side and system side current respectively. Also, the arm switching functions can be given by:

$$\begin{aligned} S_{au} &= m_a \sin(\omega_1 t + \alpha_1) - m_u \sin(\omega_3 t + \alpha_3) \\ S_{av} &= m_a \sin(\omega_1 t + \alpha_1) - m_u \sin(\omega_3 t + \alpha_3 - 120) \\ &\vdots \\ S_{cw} &= m_a \sin(\omega_1 t + \alpha_1 + 120) - m_u \sin(\omega_3 t + \alpha_3 + 120) \end{aligned} \tag{6.3}$$

where m_a, m_u, α_1 and α_3 are the generator side and system side voltage modulation ratios and angles. For the sake of convenience, recall the arm voltage and current equations from Chapter 5 here:

$$S_{arm}\ i_{arm} = C\ \frac{du_{dc}}{dt} \tag{6.4}$$

$$u_{arm} = N\ S_{arm}\ u_{dc} \tag{6.5}$$

6.2.2 Capacitor Voltage Ripples

Apply (6.4) to a specific arm for example the arm *au*, the sub-module capacitor voltage can be expressed as:

$$u_{dc\_au} = \int \frac{1}{C}\ S_{au}\ i_{au} \tag{6.6}$$

Substitute i_{au} from (6.2) and S_{au} from (6.3) into (6.6), the expression of the capacitor voltage in arm *au* can be derived. The expressions of the rest eight arms can be acquired in the same manner. The arm current and the switching function both contain fundamental frequency components at AC system frequencies ω_1 and ω_3. According to trigonometric product-to-sum identity, the capacitor voltage frequency spectrum contains $2\omega_1$, $2\omega_3$, $(\omega_3 \pm \omega_1)$ and 0 Hz

components. In this study, the system frequency is considered to be 60 Hz. In this case, beside the DC component, the capacitor voltage has ripples of 40 Hz (also 80 Hz and 120 Hz). It is interesting that these frequencies are different from frequencies at either side of the ac systems. The 40 Hz voltage ripple has the largest magnitude compared to components at other frequencies. This has been discussed and verified by the time domain simulation in the last chapter. The constituent terms at 40 Hz are analysed and the full expressions are calculated and shown as:

$$u_{dc_{au40}} = k_1[-m_a I_a \sin(\theta_1) + m_a I_u \sin(\theta_2) - m_u I_a \sin(\theta_3)]$$

$$u_{dc_{av40}} = k_1[-m_a I_a \sin(\theta_1) + m_a I_u \sin(\theta_2 - 120) - m_u I_a \sin(\theta_3 - 120)]$$

$$u_{dc_{aw40}} = k_1[-m_a I_a \sin(\theta_1) + m_a I_u \sin(\theta_2 + 120) - m_u I_a \sin(\theta_3 + 120)]$$

$$u_{dc_{bu40}} = k_1[-m_a I_a \sin(\theta_1 + 120) + m_a I_u \sin(\theta_2 + 120) - m_u I_a \sin(\theta_3 + 120)]$$

$$u_{dc_{bv40}} = k_1[-m_a I_a \sin(\theta_1 + 120) + m_a I_u \sin(\theta_2) - m_u I_a \sin(\theta_3)] \quad (6.7)$$

$$u_{dc_{bw40}} = k_1[-m_a I_a \sin(\theta_1 + 120) + m_a I_u \sin(\theta_2 - 120) - m_u I_a \sin(\theta_3 - 120)]$$

$$u_{dc_{cu40}} = k_1[-m_a I_a \sin(\theta_1 - 120) + m_a I_u \sin(\theta_2 - 120) - m_u I_a \sin(\theta_3 - 120)]$$

$$u_{dc_{cv40}} = k_1[-m_a I_a \sin(\theta_1 - 120) + m_a I_u \sin(\theta_2 + 120) - m_u I_a \sin(\theta_3 + 120)]$$

$$u_{dc_{cw40}} = k_1[-m_a I_a \sin(\theta_1 - 120) + m_a I_u \sin(\theta_2) - m_u I_a \sin(\theta_3)]$$

where: $k_1 = \frac{1}{12C\omega_1}$; $\theta_1 = 2\omega_1 t + \alpha_1 + \beta_1$; $\theta_2 = 2\omega_1 t + \beta_3 - \alpha_1$; $\theta_3 = 2\omega_1 t + \alpha_3 - \beta_1$

As can be seen from (6.7), the 40 Hz component of the capacitor voltage consists of three terms. For each term, the magnitude is the same for all nine arms while there can be a phase

shift between nine arms. When the high order components are neglected, the capacitor voltage can be expressed as the sum of the dc component and the 40 Hz component:

$$u_{dc} \approx u_{dc-0} + u_{dc\_40} \tag{6.8}$$

6.3 Arm Current Harmonics

The purpose of this section is to analyse the arm currents of the M^3C at various frequencies. In order to derive the expression of the arm currents, arm voltages are derived first. Then together with KVL equations, the arm currents are acquired so that the harmonics can be analysed.

In (6.3), switching function is of 20 Hz and 60 Hz. And in (6.8), capacitor voltage is of DC and 40 Hz. Substitute (6.3) and (6.8) into (6.5), components at different frequencies appear in arm voltage, which are shown in Table 6.1. As can be seen, arm voltage contains components at 20 Hz, 60 Hz and 100 Hz. How each component is generated is shown in the second column in Table 6.1. For instance, switching function at 60 Hz and capacitor voltage at 40 Hz gives arm voltage at 100 Hz and 20 Hz. The terms (20 + DC) and (60 + DC) are in positive sequence and they relate to the positive-sequence fundamental currents. These two terms do not belong to the scope of harmonics and therefore will not be analysed.

Table 6.1 Arm frequency components

Frequency (/Hz)	Components (/Hz)
20	(20 + DC); (40 - 20); (60 - 40)
60	(60 + DC); (20 + 40)
100	(60 + 40)

According to KVL, equations at 20 Hz, 60 Hz and 100 Hz can be written as:

$$\begin{aligned} e_a &= u_{arm\_au\_20} + L\frac{di_{au\_20}}{dt} \\ 0 &= u_{arm\_au\_60} + L\frac{di_{au\_60}}{dt} + e_u \\ 0 &= u_{arm\_au\_100} + L\frac{di_{au\_100}}{dt} \end{aligned} \tag{6.9}$$

As KVL does not alter frequency, the frequency components of the arm current remain the same as the ones of the arm voltage as Table 6.1 shows. Combine (6.3), (6.5) and (6.7) – (6.9), current harmonics at 20 Hz, 60 Hz and 100 Hz can be calculated.

6.3.1 Components at 100 Hz

The expression of the arm currents at 100 Hz is shown in (6.10). ω_5 is referred to the frequency at 100 Hz. The arm currents at 100 Hz are formed of three terms. For each term, the magnitude is the same for all nine arms. Adding up i_{au100}, i_{av100} and i_{aw100}, the three terms cancel out, which means that the arm currents at 100 Hz will not flow into phase *a* and exist only in the arm. Same rule applies to phase *b* and *c*, and therefore the arm currents at 100 Hz are isolated from the generator side AC system. In terms of the system side, the same procedure is carried out. Likewise, i_{au100}, i_{bu100} and i_{cu100} add up to zero (same for phase *v* and *w*) so no current at 100 Hz will flow into the system side. In conclusion, the natures of these currents are circulating currents which only circulate within the converter. They take up the current rating of the semiconductor devices and should be suppressed during operation.

$$i_{au100} = k_2[m_u m_a I_a \sin(\theta_4) - m_u m_a I_u \sin(\theta_5) + m_u^2 I_a \sin(\theta_6)]$$

$$i_{av100} = k_2[m_u m_a I_a \sin(\theta_4 - 120) - m_u m_a I_u \sin(\theta_5 + 120) + m_u^2 I_a \sin(\theta_6 + 120)]$$

$$i_{aw100} = k_2[m_u m_a I_a \sin(\theta_4 + 120) - m_u m_a I_u \sin(\theta_5 - 120) + m_u^2 I_a \sin(\theta_6 - 120)]$$

$$i_{bu100} = k_2[m_u m_a I_a \sin(\theta_4 + 120) - m_u m_a I_u \sin(\theta_5 + 120) + m_u^2 I_a \sin(\theta_6 + 120)]$$

$$i_{bv100} = k_2[m_u m_a I_a \sin(\theta_4) - m_u m_a I_u \sin(\theta_5 - 120) + m_u^2 I_a \sin(\theta_6 - 120)] \quad (6.10)$$

$$i_{bw100} = k_2[m_u m_a I_a \sin(\theta_4 - 120) - m_u m_a I_u \sin(\theta_5) + m_u^2 I_a \sin(\theta_6)]$$

$$i_{cu100} = k_2[m_u m_a I_a \sin(\theta_4 - 120) - m_u m_a I_u \sin(\theta_5 - 120) + m_u^2 I_a \sin(\theta_6 - 120)]$$

$$i_{cv100} = k_2[m_u m_a I_a \sin(\theta_4 + 120) - m_u m_a I_u \sin(\theta_5) + m_u^2 I_a \sin(\theta_6)]$$

$$i_{cw100} = k_2[m_u m_a I_a \sin(\theta_4) - m_u m_a I_u \sin(\theta_5 + 120) + m_u^2 I_a \sin(\theta_6 + 120)]$$

where:

$k_2 = \frac{N}{24LC\omega_1\omega_5}, \theta_4 = \omega_5 t + \alpha_3 + \alpha_1 + \beta_1, \theta_5 = \omega_5 t + \alpha_3 + \beta_3 - \alpha_1, \ \theta_6 = \omega_5 t + 2\alpha_3 - \beta_1$

6.3.2 Components at 60 Hz

According to Table 6.1, there are two sources of the 60 Hz arm currents. The first one is fundamental current and does not need to be analysed. The expression of the second component is calculated and shown in (6.11). As is shown, the first of the three terms of the

arm currents at 60 Hz has the same magnitude and phase angle for all nine arms of M^3C. As a result, it behaves as zero-sequence current for AC systems at both sides and it flows into both systems with equal magnitude if no countermeasure was implemented. This current is undesirable since it causes current distortion and can bring further instability issues like harmonic interaction and resonance. For the rest two terms, they cancel out at the fractional frequency side and are of positive sequence at the system side. They behave like the fundamental current and can be regulated by the current controller in vector control. The positive-sequence components are not problematic and strictly speaking, they do not belong to the harmonic scope.

$$
\begin{aligned}
i_{au60_2} &= k_3[-m_a^2 I_a \sin(\theta_7) + m_a^2 I_u \sin(\theta_8) - m_a m_u I_a \sin(\theta_9)] \\
i_{av60_2} &= k_3[-m_a^2 I_a \sin(\theta_7) + m_a^2 I_u \sin(\theta_8 - 120) - m_a m_u I_a \sin(\theta_9 - 120)] \\
i_{aw60_2} &= k_3[-m_a^2 I_a \sin(\theta_7) + m_a^2 I_u \sin(\theta_8 + 120) - m_a m_u I_a \sin(\theta_9 + 120)] \\
i_{bu60_2} &= k_3[-m_a^2 I_a \sin(\theta_7) + m_a^2 I_u \sin(\theta_8) - m_a m_u I_a \sin(\theta_9)] \\
i_{bv60_2} &= k_3[-m_a^2 I_a \sin(\theta_7) + m_a^2 I_u \sin(\theta_8 - 120) - m_a m_u I_a \sin(\theta_9 - 120)] \\
i_{bw60_2} &= k_3[-m_a^2 I_a \sin(\theta_7) + m_a^2 I_u \sin(\theta_8 + 120) - m_a m_u I_a \sin(\theta_9 + 120)] \\
i_{cu60_2} &= k_3[-m_a^2 I_a \sin(\theta_7) + m_a^2 I_u \sin(\theta_8) - m_a m_u I_a \sin(\theta_9)] \\
i_{cv60_2} &= k_3[-m_a^2 I_a \sin(\theta_7) + m_a^2 I_u \sin(\theta_8 - 120) - m_a m_u I_a \sin(\theta_9 - 120)] \\
i_{cw60\_2} &= k_3[-m_a^2 I_a \sin(\theta_7) + m_a^2 I_u \sin(\theta_8 + 120) - m_a m_u I_a \sin(\theta_9 + 120)]
\end{aligned}
\tag{6.11}
$$

where: $k_3 = \frac{N}{24LC\omega_1\omega_3}$; $\theta_7 = \omega_3 t + 2\alpha_1 + \beta_1$; $\theta_8 = \omega_3 t + \beta_3$; $\theta_9 = \omega_3 t + \alpha_1 + \alpha_3 - \beta_1$

6.3.3 Components at 20 Hz

The harmonic currents at 20 Hz are analysed by carrying out the same calculations to the second and the third terms of 20 Hz in Table 6.1. Results are concluded in Table 6.2. Detailed equations are expressed as (6.12) and (6.13). The first term of the component (40-20) Hz and the second and third terms of the component (60-40) Hz behave like the positive-sequence fundamental current. The second and third terms of the component (40-20) Hz and the first term of the component (60-40) Hz only exist in the arms and do not flow into AC systems.

Table 6.2 20 Hz arm current

Frequency (/Hz)		Generator Side	System Side
(40 - 20)	Term1	Positive sequence	Cancelled out
	Term2&3	Cancelled out	Cancelled out
(60 - 40)	Term1	Cancelled out	Cancelled out
	Term2&3	Positive sequence	Cancelled out

The expressions of the 20 Hz arm currents are calculated and shown as:

$$i_{au20_2} = k_4[m_a^2 I_a \, sin(\theta_{10}) - m_a^2 I_u \, sin(\theta_{11}) + m_a m_u I_a \, sin(\theta_{12})]$$

$$i_{av20_2} = k_4[m_a^2 I_a \, sin(\theta_{10}) - m_a^2 I_u \, sin(\theta_{11} - 120) + m_a m_u I_a \, sin(\theta_{12} - 120)] \quad (6.12)$$

$$i_{aw20_2} = k_4[m_a^2 I_a \, sin(\theta_{10}) - m_a^2 I_u \, sin(\theta_{11} + 120) + m_a m_u I_a \, sin(\theta_{12} + 120)]$$

$$i_{bu20_2} = k_4[m_a^2 I_a \sin(\theta_{10} - 120) - m_a^2 I_u \sin(\theta_{11} - 120) + m_a m_u I_a \sin(\theta_{12} - 120)]$$

$$i_{bv20_2} = k_4[m_a^2 I_a \sin(\theta_{10} - 120) - m_a^2 I_u \sin(\theta_{11} + 120) + m_a m_u I_a \sin(\theta_{12} + 120)]$$

$$i_{bw20_2} = k_4[m_a^2 I_a \sin(\theta_{10} - 120) - m_a^2 I_u \sin(\theta_{11}) + m_a m_u I_a \sin(\theta_{12})]$$

$$i_{cu20_2} = k_4[m_a^2 I_a \sin(\theta_{10} + 120) - m_a^2 I_u \sin(\theta_{11} + 120) + m_a m_u I_a \sin(\theta_{12} + 120)]$$

$$i_{cv20_2} = k_4[m_a^2 I_a \sin(\theta_{10} + 120) - m_a^2 I_u \sin(\theta_{11}) + m_a m_u I_a \sin(\theta_{12})]$$

$$i_{cw20\_2} = k_4[m_a^2 I_a \sin(\theta_{10} + 120) - m_a^2 I_u \sin(\theta_{11} - 120) + m_a m_u I_a \sin(\theta_{12} - 120)]$$

where: $k_4 = \frac{N}{24LC\omega_1^2}$; $\theta_{10} = \omega_1 t + \beta_1; \theta_{11} = \omega_1 t + \beta_3 - 2\alpha_1$; $\theta_{12} = \omega_1 t + \alpha_3 - \beta_1 - \alpha_1$

$$i_{au20_3} = k_4[-m_u m_a I_a \sin(\theta_{13}) + m_u m_a I_u \sin(\theta_{14}) - m_u^2 I_a \sin(\theta_{15})]$$

$$i_{av20\_3} = k_4[-m_u m_a I_a \sin(\theta_{13} - 120) + m_u m_a I_u \sin(\theta_{14}) - m_u^2 I_a \sin(\theta_{15})]$$

$$i_{aw20\_3} = k_4[-m_u m_a I_a \sin(\theta_{13} + 120) + m_u m_a I_u \sin(\theta_{14}) - m_u^2 I_a \sin(\theta_{15})] \quad (6.13)$$

$$i_{\mathrm{bu}20_3} = k_4[-m_u m_a I_a \sin(\theta_{13} - 120) + m_u m_a I_u \sin(\theta_{14} - 120) - m_u^2 I_a \sin(\theta_{15} - 120)]$$

$$i_{\mathrm{bv20_3}} = k_4[-m_u m_a I_a \, sin(\theta_{13} + 120) + m_u m_a I_u \, sin(\theta_{14} - 120) - m_u^2 I_a \, sin(\, \theta_{15} - 120)]$$

$$i_{\mathrm{bw20_3}} = k_4[-m_u m_a I_a \, sin(\theta_{13}) + m_u m_a I_u \, sin(\theta_{14} - 120) - m_u^2 I_a \, sin(\, \theta_{15} - 120)]$$

$$i_{\mathrm{cu20_3}} = k_4[-m_u m_a I_a \, sin(\theta_{13} + 120) + m_u m_a I_u \, sin(\theta_{14} + 120) - m_u^2 I_a \, sin(\, \theta_{15} + 120)]$$

$$i_{\mathrm{cv20_3}} = k_4[-m_u m_a I_a \, sin(\theta_{13}) + m_u m_a I_u \, sin(\theta_{14} + 120) - m_u^2 I_a \, sin(\, \theta_{15} + 120)]$$

$$i_{\mathrm{cw20\_3}} = k_4[-m_u m_a I_a \, sin(\theta_{13} - 120) + m_u m_a I_u \, sin(\theta_{14} + 120) - m_u^2 I_a \, sin(\, \theta_{15} + 120)]$$

where: $\theta_{13} = \omega_1 t + \alpha_3 - \alpha_1 - \beta_1;\ \ \theta_{14} = \omega_1 t + \alpha_3 - \beta_3 + \alpha_1;\ \theta_{15} = \omega_1 t + \beta_1$

To sum up, the components of the arm currents analysed above can be classified into three types. The first type only circulates within the M^{3}C and does not flow into AC systems. The second type does not cancel out at terminals and therefore goes into AC systems as zero-sequence current. The third type acts like positive-sequence fundamental current. The affecting factors of harmonic magnitude and influences of these harmonics on M^{3}C itself and also AC systems connected to it are discussed in the following section.

6.4 Affecting Factors and Influences of the Harmonic Components

As Equations (6.10) – (6.13) show, the magnitude of these harmonic components depends on the sub-module capacitance, the inductance, the frequency of the AC system etc. The smaller the capacitance or the inductance, the larger the harmonics magnitude would be. If the AC system frequency is very small, in theory the harmonic components become infinity and the system could not function properly. Thus, the working frequency of the FFTS cannot be too low. In addition, current harmonics are related to capacitor voltage ripples. Effective ripple control is beneficial to harmonic suppression. Some of the current components coincide with the system frequency and are easy to omit.

Based on the analysis in Section 6.3, it is indicated that there will be zero-sequence current flowing into the AC systems at both sides if no countermeasure was conducted. This can be problematic as wind farm is prone to stability problems [115]. Attention should also be paid to the system side, because offshore wind farms are often situated in remote areas, where the strength of the AC network is weak [116]. Among three types of currents discussed in the last section, the components in positive sequence are not harmful since they can be regulated by the close-loop current controller. Circulating current and zero-sequence current can adversely influence the converter and AC systems in the following aspects:

• Both circulating and zero-sequence currents take up current rating of the power electronic devices. They raise thermal issues and degrade the semiconductors. For multilevel converters, high voltage can be achieved by stacking up sub-modules but current ability limits the power rating. In terms of an offshore wind power transmission project, converter capital cost and power loss cost are therefore increased.

• The zero-sequence currents can flow into the AC network, which bring additional losses in devices including transformers and AC motors and raise the component temperature. The aging of devices is accelerated and power loss also leads to low efficiency.

• The harmonic currents flowing in the AC system can further cause instability problems. Large magnitude of zero-sequence current may trip the zero-sequence protection. When wind energy has high penetration, unexpected disconnection of a large wind power source would have a significant effect on power system stability. Besides, harmonic interaction or resonance may happen. Torsional oscillation can be triggered in generators with the existence of injected harmonic currents which results in shaft fatigue or even shaft failure [117, 118].

When the three phases of a transformer are manufactured to be close enough, the transformer is regarded as symmetric. And as transformer is not rotating, the positive-sequence and negative-sequence impedances of the transformer are the same. However, the zero-sequence impedance of a transformer depends on the winding connections and consequently affects zero-sequence current [45]. Fig. 6.2 and Fig. 6.3 show the zero-sequence equivalent circuit of Y/Δ connection and Y/y connection with grounding respectively, where Z_g represents the grounding impedance and Z_0 is the sum of primary side and secondary side leakage impedances per phase. For Y/Δ connection, the primary side provides a path for zero-sequence current. Zero-sequence current is inducted in the secondary side but it can only circulate within the delta winding and no zero-sequence current would occur on the external circuit connected to the secondary side of the transformer. Seen from the secondary side, delta winding does not provide a path for zero-sequence current so the equivalent impedance is infinite (open circuit). Contrarily, the zero-sequence current can flow through the transformer for the Y/y connection.

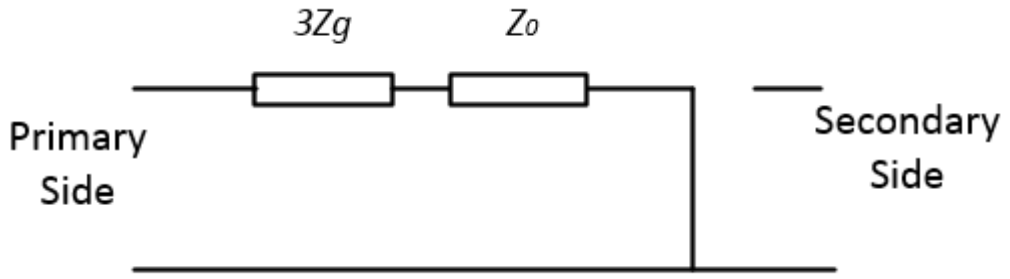

Fig. 6.2 Equivalent circuit of Y/Δ connected three-phase transformer on zero-sequence.

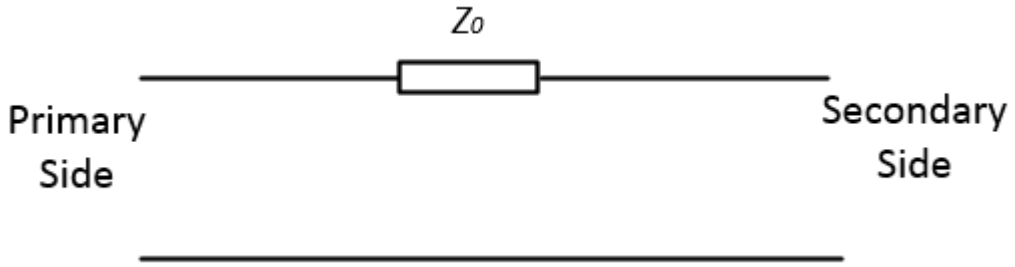

Fig. 6.3 Equivalent circuit of Y/y connected three-phase transformer on zero-sequence.

The transformer connection in an offshore wind power system based on real projects is shown in Fig. 6.1, with more details available in [119, 120]. The step-up transformer at the wind generator side usually includes delta connection, as a result of which, the zero-sequence currents could not reach the wind generator. Thus, it can be assumed that the wind farm side stability will not suffer from it. However, for the system side, due to protection considerations at high voltage level (several hundred kV), transformers are normally in Y/y connection with grounding. Y/y transformer enjoys the advantages of fewer turns for winding, lower insulation level, no phase displacement and therefore is cheaper and suitable for high voltage applications [121]. Further action should be taken when the harmonic magnitude is large. Besides FFT, another topology (As shown in Fig 6.4) to connect medium voltage high power wind turbine using M^3C is proposed in [122, 123]. In this application, maximum power point

tracking can be achieved and good dynamic performance was validated. However, in terms of harmonics, zero-sequence currents can impede the wind generator and also the electrical network, so further measures should be taken.

Undoubtedly, sub-module capacitance and arm inductance should be carefully selected to limit the harmonics. Besides, one option could be adopting delta winding for the grid-connecting transformer to cut off the path of the zero-sequence currents. However, in that case the benefits of the Y/y transformer would no longer exist. Another solution is to leave the transformer unchanged, but adopt a closed-loop controller to suppress the zero-sequence currents using the controllability of the M^3C. The control algorithm will be discussed and the effectiveness will be verified in Section 6.6.

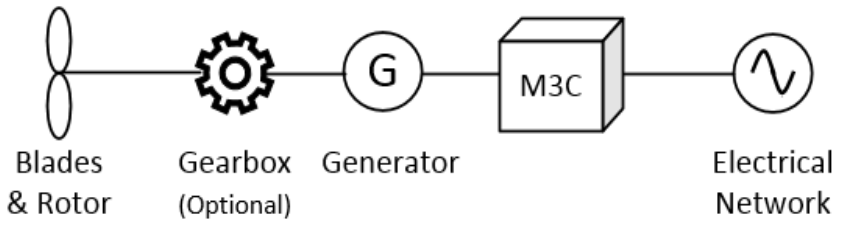

Fig. 6.4 Topology to connect a high power wind turbine via M^3C.

6.5 Simulation Validation and Analysis

To validate the theoretical analysis, a M^3C connecting two AC systems at 20 Hz and 60 Hz is simulated in RTDS (introduced in Chapter 3). Each arm has forty sub-modules. System at 20 Hz transmits power to 60 Hz side. Simulation parameters are provided in Appendix A. The M^3C simulated in RTDS is a detailed model and the simulation time step is set to 3 μs to guarantee the accuracy of the simulation results. The assumptions can be verified and the theoretical analysis can be compared to simulation results. The control method adopted is the

vector control with inner current loops and outer loops for active/reactive power control or capacitor voltage balancing control. Details of the control system have been discussed in Chapter 3. Note that in this chapter, the capacitor voltage for the control input should be the filtered version to avoid influence of the controller on the quantified analysis. Otherwise the controller would try to control the capacitor voltage ripple as well and cause discrepancy to the comparison. A low pass filter is applied to the active power signal for the same consideration.

Firstly, the harmonics at 20 Hz side is studied. Y/Δ connection is selected for the step-up transformer connecting the M^3C and the generator side, which can be shown in Fig. 6.1. The frequency spectrums of both sides of the transformer are plotted in Fig 6.5. It can be observed in Fig 6.5 (a) that the 60 Hz harmonic current does flow into the 20 Hz side AC system. But due to the delta connection of the transformer, it is isolated from the generator side (See Fig 6.5 (b)) and has no effect on wind generators. Besides, two sets of capacitance values are chosen as 0.01 F and 0.005 F respectively. It can be observed that when the capacitance is halved, the harmonic current magnitude doubles. Results validate the analysis in Section 6.3.

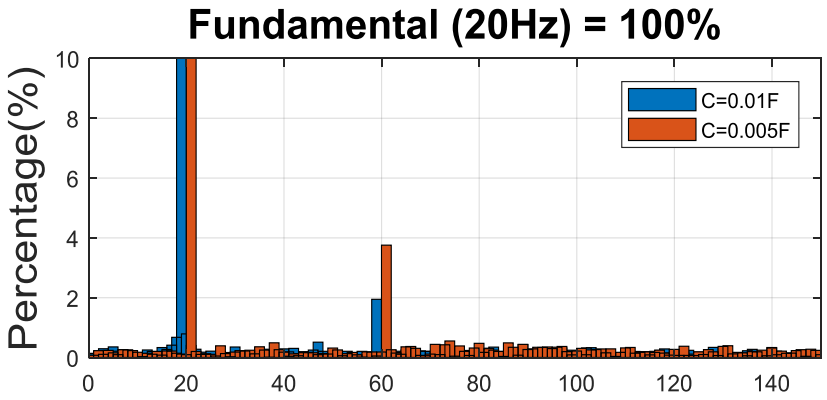

(a) M^3C side star connection current frequency spectrum.

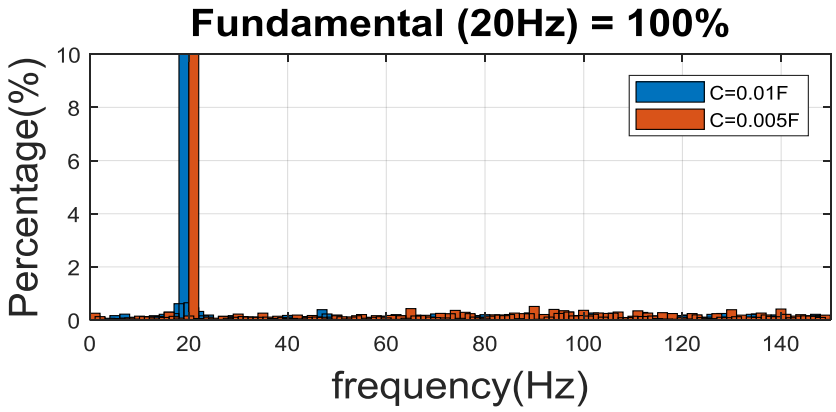

(b) Generator side delta connection current frequency spectrum.

Fig. 6.5 Frequency spectrum of currents at 20 Hz Side.

On the system side, the line currents are measured and decomposed into positive-sequence currents and zero-sequence current. Fig. 6.6 shows that the positive-sequence currents peak at 0.68 kA while the zero-sequence current peaks at 0.013 kA. The amplitude of the zero-sequence current is 2% of the base currents. And it agrees with the current frequency spectrum (left bar at 60Hz, Fig. 6.5 (a)).

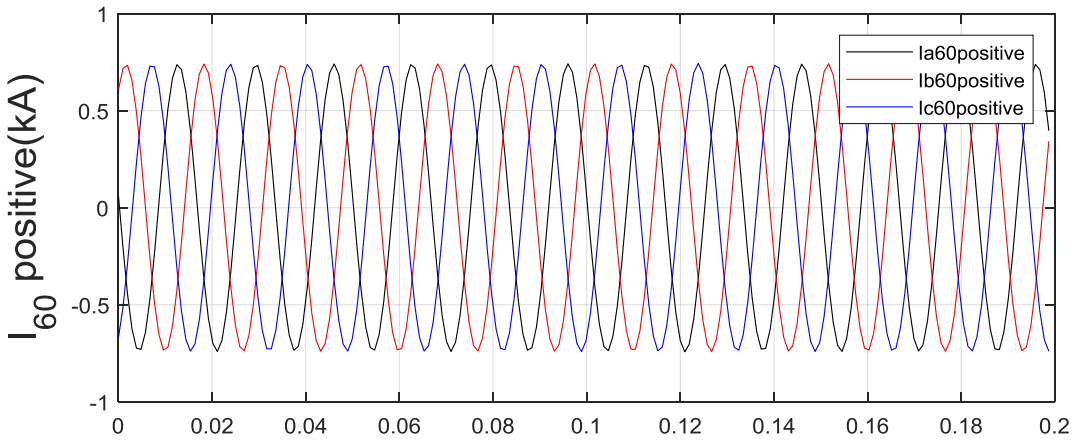

(a) Positive Sequence Currents at 60 Hz.

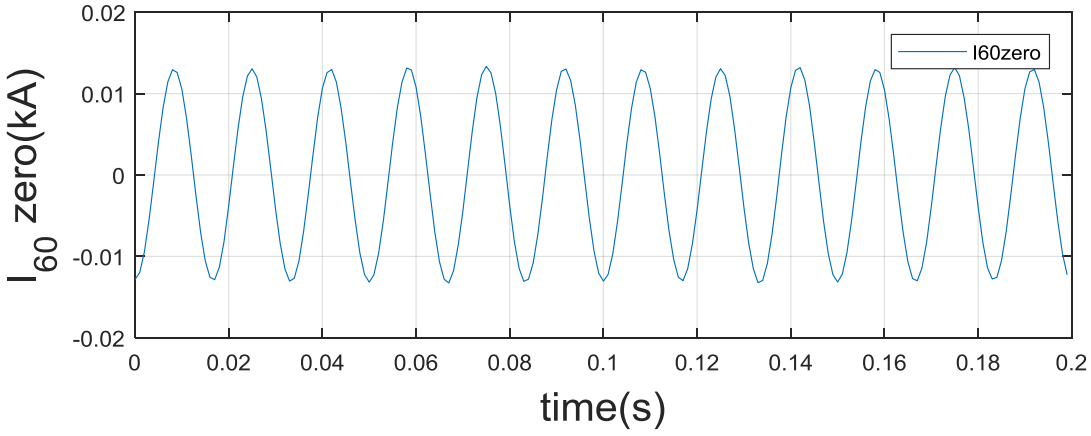

(b) Zero-Sequence Current at 60 Hz.

Fig. 6.6 Currents at 60 Hz Side.

Arm harmonic current can be calculated as ($i_{au} - \frac{1}{3} i_a - \frac{1}{3} i_u$). As an example, the frequency spectrum of harmonic current in arm *au* is plotted in Fig 6.7. As is expected, the arm harmonic current contains 20 Hz (circulating), 60 Hz (zero-sequence) and 100 Hz (circulating) components. There is also a small amount of 140 Hz component. It can be studied using the same method and including the higher order voltage ripples. When the capacitance is halved, similarly, harmonic magnitudes double. Again, the simulation result validates the theoretical analysis.

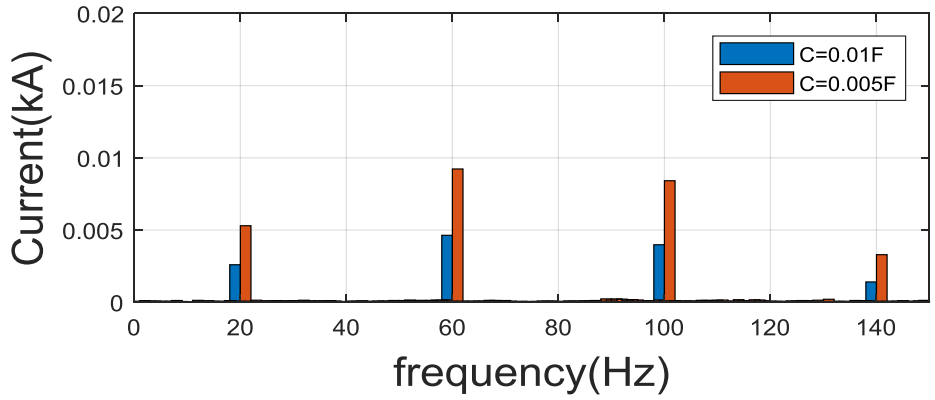

Fig. 6.7 Frequency spectrum of arm current harmonics.

To compare the analytical formulas with the simulation model, the calculated value (red) of the 40 Hz capacitor voltage ripple is plotted together with the measured ripple at 40 Hz in time domain simulation (black) in Fig 6.8. As can be seen, there is a good match between the two curves and therefore the calculated value has high accuracy. In addition, the calculated values of harmonic currents are compared with the measured values in simulation and the results are shown in Table 6.3. It can be seen that the difference is only 0.001-0.002 kA. However, the values of harmonic currents are small so the discrepancy in percentage can be around 20%. Hence, the current magnitude calculation is less accurate than the ripple voltage. Specifically, the calculated 60 Hz zero-sequence current is larger since theoretical analysis neglects resistance, with the presence of which, the actual current has a smaller value. For the 100 Hz and 20 Hz harmonic currents, the calculated values are smaller as is expected, because theoretical analysis does not include the higher orders of the capacitor voltage ripple that can also lead to harmonic currents at 100 Hz and 20 Hz. For example, the 80 Hz voltage ripple interacts with the 20 Hz component in switching function and produces 100 Hz harmonics (80 + 20), or interacts with the 60 Hz component and produces 20 Hz harmonics (80 - 60).

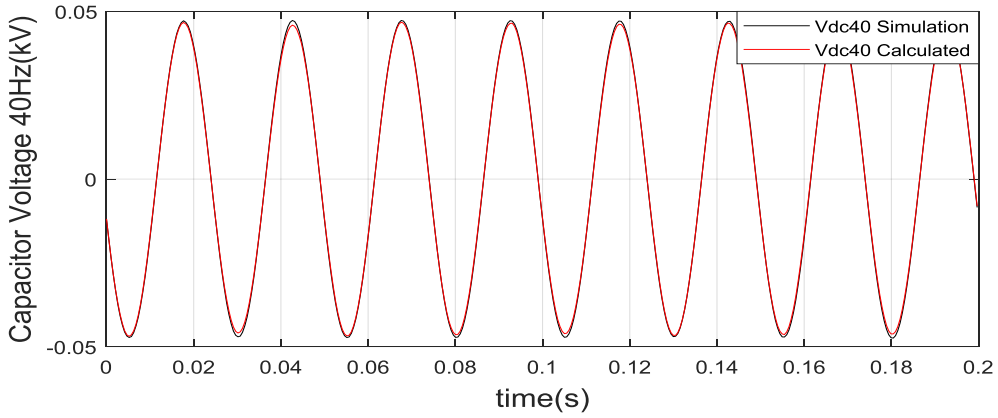

Fig. 6.8 Capacitor voltage 40 Hz – simulation result (black) and calculation value (red).

Table 6.3 Quantification comparison with simulation results

Harmonic Component	Calculation Value (kA)	Simulation Value (kA)	Discrepancy (%)
60 Hz	0.014	0.012	16.7
100 Hz	0.007	0.009	22.2
20 Hz	0.004	0.005	20.0

6.6 Suppression of M^{3}C Harmonics

M^{3}C harmonics can be controlled using hardware or software solutions. Based on the discussion in Section 6.4, it is known that sub-module capacitance and arm inductance are affecting factors of the harmonics. So, proper values of the elements can be selected to limit the harmonics within a certain range. A detailed analysis is conducted in this section to provide instructions for capacitor and inductor values selection for the purpose of limiting harmonics. Also, delta connection could be an option for the grid-connecting transformer on the offshore side to deal with zero-sequence harmonic currents. The above measures are regarded as hardware methods to suppress M^{3}C harmonics. On the other hand, an effective zero-sequence current mitigation control algorithm is proposed and tested for M^{3}C in Subsection 6.6.2, which is indicated as a software method for harmonic suppression. In this section, an index of revised total harmonic distortion (rTHD) is proposed for three-phase systems which can consider the sequence of the quantities. For this index, zero-sequence current is regarded as harmonic and a more accurate description of the harmonic condition of M^{3}C is provided.

6.6.1 Proper Selection of Sub-Module Capacitance and Arm Inductance

At steady-state operation, it is normally considered that the voltage deviation should be kept within 10% of the DC sub-module capacitor voltage [32]. In Fig. 6.9, the capacitor voltage ripple is plotted against the sub-module capacitance for the test system. As can be seen, capacitance should be 3 mF or above in this case so that the maximum voltage ripple requirement is satisfied. In addition, the voltage ripple is plotted against the reciprocal of the capacitance. As is shown in Fig. 6.10, it is very closed to a perfect straight line, and therefore the time domain simulation confirms the analytical formula, which indicates that the capacitor voltage ripple is inversely proportional to sub-module capacitance.

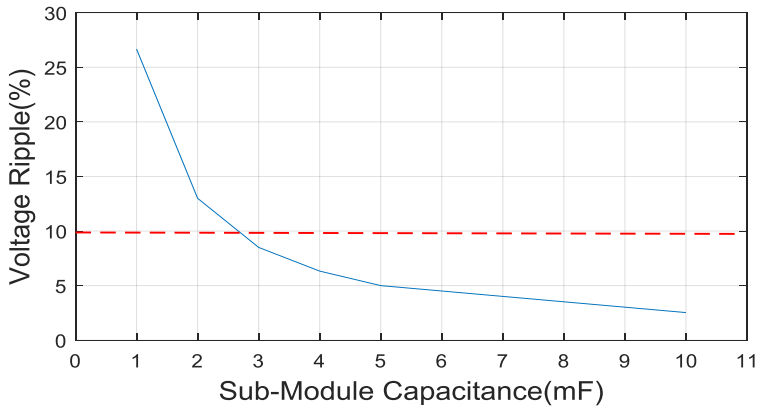

Fig. 6.9 Percentage voltage ripple versus sub-module capacitance.

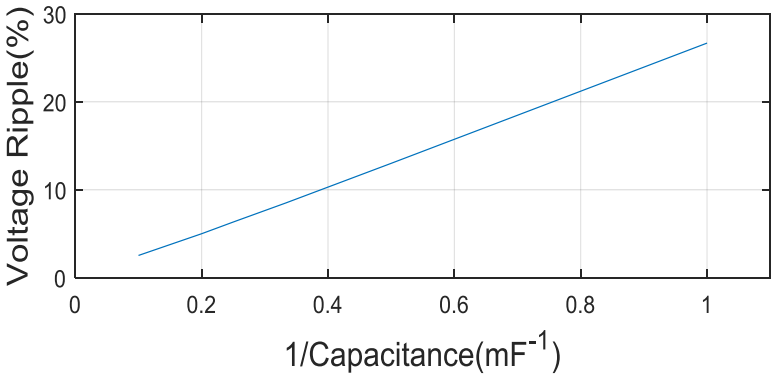

Fig. 6.10 Percentage voltage ripple versus 1/C.

The traditional current THD is defined as (6.14), where subscript 1 indicates the current at fundamental frequency and subscript 2, 3 and 4 refer to currents at second, third and fourth order etc. A suitable value should be selected for arm inductance to limit the THD within a certain level. But as is known, there is a zero-sequence harmonic component at 60 Hz and the traditional THD cannot distinguish it from the fundamental positive-sequence current. Therefore, there is need to propose a rTHD index to overcome this difficulty and take the 60 Hz zero-sequence harmonic current into consideration. It is proposed and defined as (6.15), where I_1^p is the fundamental positive-sequence current for a three-phase system.

$$THD_i = \frac{\sqrt{I_2^2 + I_3^2 + I_4^2 + \cdots}}{I_1} \tag{6.14}$$

$$rTHD_i = \frac{\sqrt{(I_1 - I_1^p)^2 + I_2^2 + I_3^2 + I_4^2 + \cdots}}{I_1^p} \tag{6.15}$$

When there is no zero-sequence or negative-sequence current at fundamental frequency, the values of THD and rTHD are the same. Otherwise, the value of rTHD would be always larger than that of THD. Both indexes are plotted with sub-module capacitance fixed at 5 mF and various arm inductances in Fig 6.11. For instance, if THD needs to be limited lower than 8%, an arm inductance larger than 10.6 mL is required. However, when rTHD is considered, a minimum of 11.5 mL is needed. When zero-sequence or negative-sequence quantity exists at fundamental frequency, THD could underestimate the distortion level of the current (or the voltage) or even provide misleading information. For instance, if the zero-sequence harmonic component is suppressed, according to the definition of THD, the numerator would remain the same and the denominator would decrease, resulting in a higher THD level, which indicates that the harmonic situation becomes worse but it is not the case. The proposed rTHD

is useful under such a circumstance and can provide a more accurate description of the system harmonic distortion level.

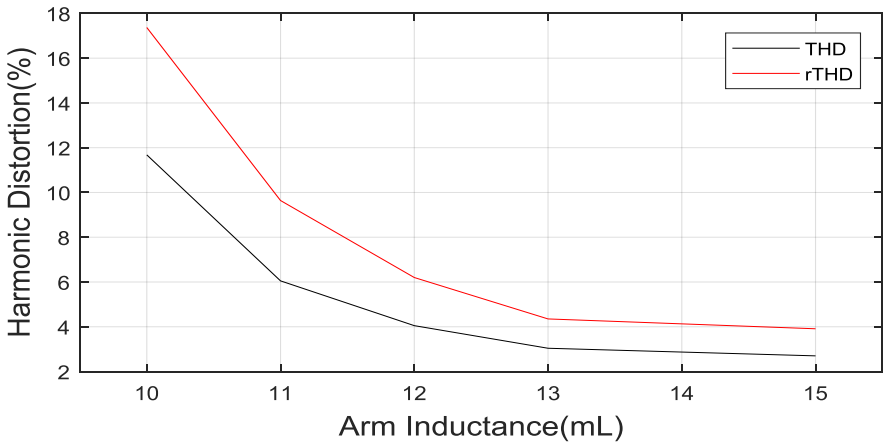

Fig. 6.11 THD and rTHD at different arm inductor values.

6.6.2 Zero-Sequence Current Mitigation Control

In this subsection, a zero-sequence current mitigation controller is proposed for M^3C and the control diagram is shown in Fig. 6.12. The principle is to use the M^3C to generate a compensating zero-sequence voltage v_0 based on the measured zero-sequence current. The control purpose is to reduce the undesirable zero-sequence current down to zero. θ_3 is the angle of the zero-sequence current and more details on the PLL for measuring it can be found in [124]. Considering that the zero-sequence harmonic currents are the same for all nine arms, only one controller is enough for all the arms in the M^3C to fulfil the control target.

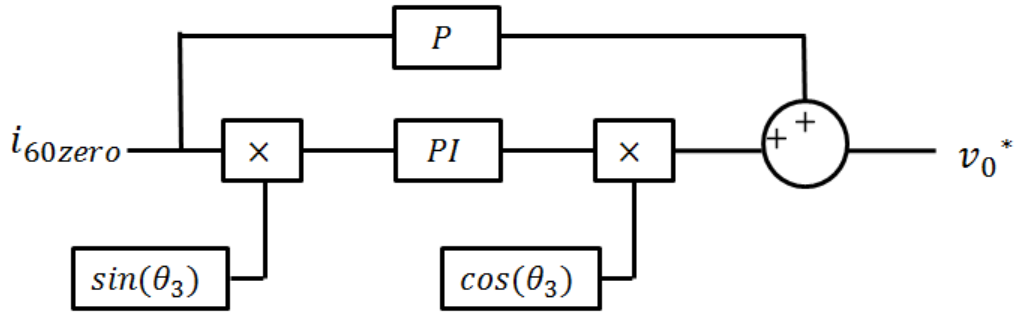

Fig. 6.12 Control diagram of the proposed zero-sequence current mitigation controller.

In terms of controller parameters determination, gains cannot be too large for the mitigation controller. The reason is that the zero-sequence current mitigation control is an auxiliary control and it should not affect the primary vector control. If large gains are used, when the controller is switched on, there would be a large zero-sequence voltage demand during the transient period. This zero-sequence voltage is superposed to the voltage reference from vector control and may cause saturation of the converter. For illustrative purpose, a very small sub-module capacitance is used (1 mF) to verify the effectiveness of the controller. Other parameters remain unchanged as in the last section. Controller parameters are available in the Appendix A. Note that besides 60 Hz, 180 Hz is also a prominent frequency that has zero-sequence current, so another controller is implemented based on the same principle. As can be seen in Fig. 6.13 (a), the AC current waveforms at both sides are of poor quality and have a high rTHD of 9.77% at 20 Hz side and 13.81% at 60 Hz side. Fig. 6.13 (b) shows the current waveforms after the mitigation control is implemented. A significant improvement can be seen and the rTHDs are greatly reduced to 3.13% and 3.98% respectively. The zero-sequence current is plotted in Fig. 6.14 with the controller switched on at the beginning of the simulation. It can be seen that with small gains, it may take seconds to fully drop the zero-

sequence current, but at steady state, the zero-sequence current can be suppressed to a negligible level and the effectiveness of the controller is verified.

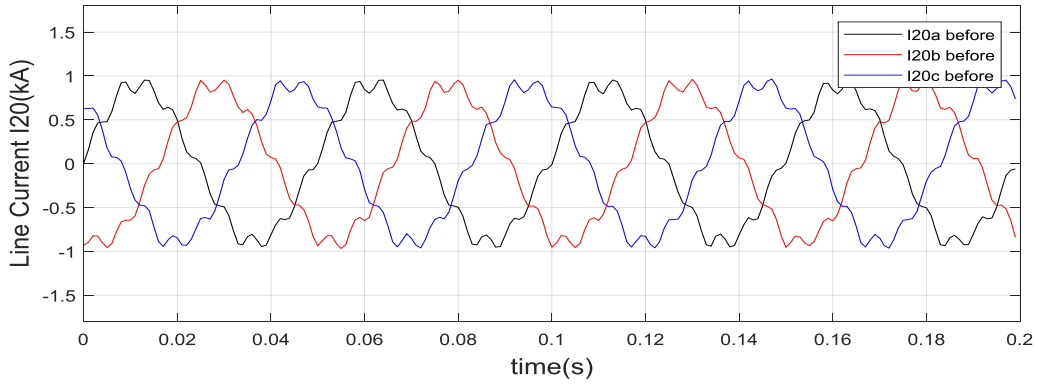

(a) Line currents at 20 Hz side before controller implemented.

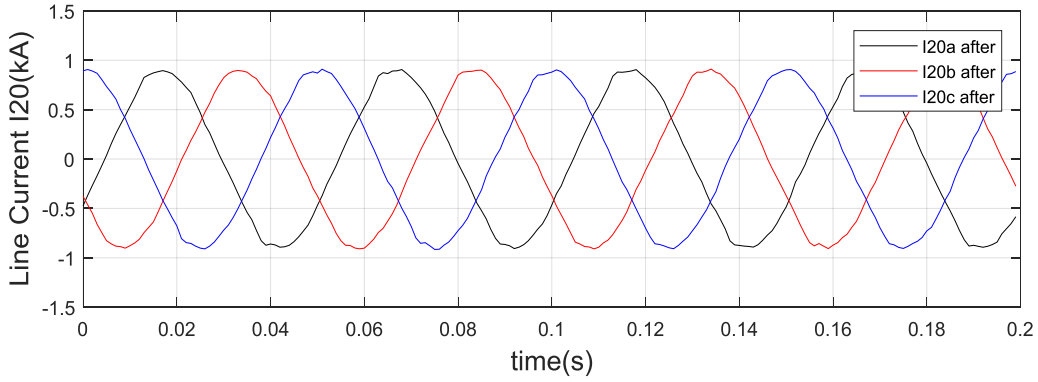

(b) Line currents at 20 Hz side after controller implemented.

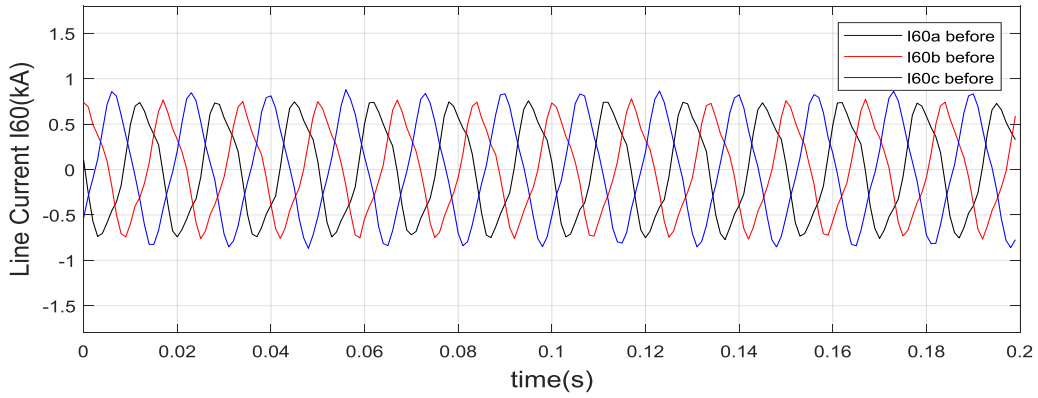

(c) Line currents at 60 Hz side before controller implemented.

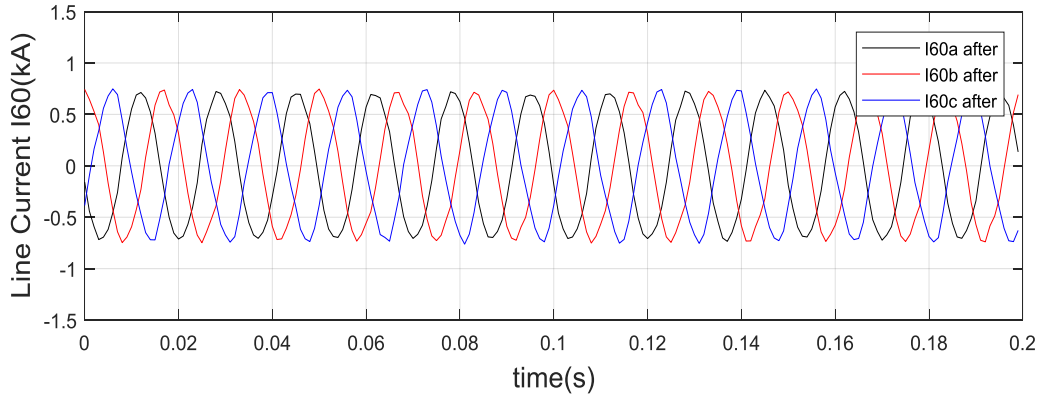

(d) Line currents at 60 Hz side after controller implemented.

Fig. 6.13 Line currents at 20 Hz and 60 Hz sides before and after the zero-sequence current mitigation controller implementation.

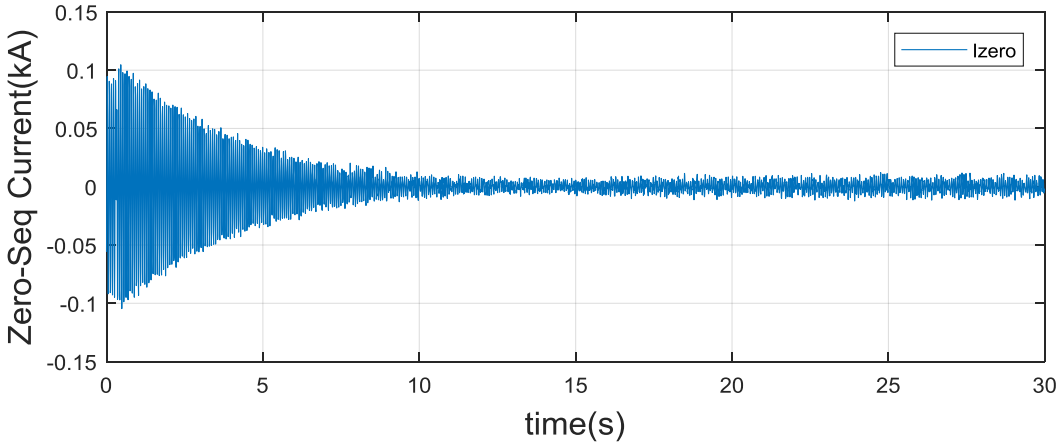

Fig. 6.14 Mitigation of zero-sequence current with controller switched on at the start of simulation.

6.7 Summary

As M^3C is the core device in the FFTS, its harmonics have a considerable influence on the overall system performance. This chapter has conducted a detailed harmonic analysis for M^3C. Owing to the interaction between the switching function and the arm current at multiple frequencies, capacitor voltage ripples are induced on top of the DC voltage component. In

addition, it has been indicated that these ripples affect the arm voltages and further the arm currents. Also, it has been found that the arm currents contain harmonic components at 20 Hz, 60 Hz and 100 Hz and they have been analysed respectively. The expressions of currents for all nine arms have been derived so that each component can be quantified. It has been found that several factors have large impact on the current harmonic magnitude, including capacitance, inductance and system operating frequency. The analysis has also revealed the nature of all the terms of the harmonic components. Some terms flow into AC systems at both sides, some terms are cancelled out and only exist in the arms, and the others have similar characteristics as the fundamental currents. Positive-sequence components can be regulated by the current controller and are not problematic. Zero-sequence components can cause instability problems, bringing risks of tripping zero-sequence protection, harmonics interaction and torsional oscillation. Both zero-sequence and circulating components take up current rating of the converter and have negative economic impact. They also bring extra losses, raise thermal issues and adversely affect the operation of other devices. Delta connection provides an isolation on zero-sequence currents. In other cases, the harmonic currents can flow into the system or the generator and can cause a series of problems. The quantified calculation has been compared with simulation results in RTDS and good matches have validated the theoretical analysis. Instructions on sub-module capacitance and arm inductance have been given to limit the capacitor voltage ripple and harmonic currents within a certain range. The index of rTHD has been proposed to provide a more precise description of M^3C harmonic level. A zero-sequence current mitigation control has been implemented and tested. Although the analysis has been carried out for FFT in this chapter, the procedure is general and can be beneficial to M^3C modelling and control method development.

CHAPTER 7 CONCLUSIONS AND FUTURE WORK

7.1 Conclusions

For the sake of reducing carbon emission and the usage of fossil fuel energy, countries worldwide are developing renewable energy with their great effort. In the past two decades, projects of wind power have been blooming and the development of offshore wind power is particularly dramatic. Offshore wind power enjoys the merits of high and rich resource, suitability for large-scale exploitation and low social impact on populated areas. In the literature there are three mainstream types of transmission technologies for offshore wind farm. HVAC is a mature and economical option for short distance offshore wind power system integration. It is adopted by most wind farms nowadays to reduce risk and improve the profit-return ability of the expensive offshore wind projects. However, the transmission distance of HVAC is limited by the capacitive charging current and therefore it cannot fulfil the requirement of future offshore wind power development. HVDC is a suitable choice for long distance transmission and it has been employed by several offshore projects in Germany. Besides, FFT can mitigate the charging current disadvantage of HVAC and is known as a promising candidate for offshore wind power application. Chapter 1 has presented a comparison between the three technologies and highlight the relatively new technology FFT. A brief introduction of M^3C has been given. Research motivations, objectives and contributions have also been presented.

M^3C is considered as the next-generation AC/AC converter for high power applications and it is the core component for FFT. It is favoured with the merits of satisfactory controllability, flexible scalability and low loss. Chapter 2 has reviewed relevant research in the literature,

providing an overall picture and necessary information for the following chapters. Existing economic analysis of offshore wind power systems has been reviewed, with four popular economic-analysis methods presented and discussed. The principle of small signal analysis has been provided, so does an amount of existing work on converter small signal modelling. The applications and various control strategies of M^3C have been discussed to present a complete image of the multilevel AC/AC converter.

Chapter 3 has thoroughly discussed the configuration, operating principle and the control strategy of the M^3C, building up the fundamental knowledge base for the M^3C small signal modelling and harmonic analysis. Sub-module level, arm level and converter level controls have been discussed to give a complete description of the M^3C control strategy. The test system used in the doctoral study has been developed according to the principle and control method. The performance of the M^3C has been verified as the frequency changer.

The offshore wind power industry is money-driven and stake holders pay more attention to risk and profit rather than the novelty of the technology. If a technology is proven to be not economical for offshore wind power application, the significance of related research work would be impeded as the outcome is not very likely to make contribution to an actual project in reality. Therefore, this thesis first investigates the economic aspects of the M^3C FFT. In Chapter 4, a cost model has been developed taking into account both the capital cost and the time-related costs including unavailability cost, O&M cost and power loss cost. A cost analysis has been presented to identify the major cost elements of the offshore wind power system. It has been found that the capital cost of the wind turbines is the most costly and the overall O&M cost throughout the whole project ranks second in the cost constituents. A detailed cost comparison has been presented between M^3C FFT and MMC HVDC. The economical transmission distance range has been indicated for both technologies under

different power ratings of the offshore wind power system. It has been found that M^3C FFT is economically advantageous over MMC HVDC at medium transmission distance. Sensitivity analysis has shown that energy price and capacity factor have larger impact on the cost comparison while discount rate and project life time are less sensitive. It has been found that DFIG can maximise the economic strength of M^3C FFT and it is still the more cost-effective transmission technology even at a distance about 300 km.

Besides economic analysis, this thesis has also looked into the technical aspects of M^3C. In Chapter 5, a small signal model of M^3C has been developed. As M^3C FFT is a competitive solution for offshore wind power transmission, there is great need of a model to investigate its impact on existing power systems. The proposed small signal model is easy to implement and can contribute to system stability analysis with simple interfaces with external AC systems and control system. It has considered the dynamics of AC currents and sub-module capacitor voltage with DC and ripple components. Besides the vector control, the dynamics of PLL control and the measurement unit have been included. The small signal model can provide useful advice on controller parameters and sub-module capacitance selection. It has been found that a large integral gain of the D axis outer loop control is not recommended as it can cause power oscillation, making the system unstable. Contrarily, increasing integral gain of the PLL improves the small signal stability. The selection of the proportional gain of PLL should be careful since it has been found that a small gain does not provide sufficient damping while a very large gain moves the related eigenvalue towards the unstable half of the complex plane. Also, it has been found that the analysis of the capacitor ripple voltage modes is necessary as they can have poor damping if the sub-module capacitance is chosen inappropriately. The small signal model is beneficial to system stability study and controller design.

Harmonic analysis of M^3C is of significant importance from the stability point of view and is also important to prevent device damage and economic loss. Without a DC link, quantities at two frequencies intertwine in M^3C, and further interaction with the switching function induces sub-module capacitor voltage ripples and complex harmonic profile. It has been found that 20 Hz, 60 Hz and 100 Hz harmonic components exist in the arm currents and they have been analysed respectively. The expressions of harmonic currents for all nine arms have been calculated so that the analysis can be quantified. Besides, the impact of each harmonic term has been discussed. It has been found that some terms are cancelled out at both ends of the AC systems and circulate only within the converter. Circulating currents take up current rating of the converter and have negative impact on the converter. Some terms are zero-sequence and can flow into AC systems, bringing instability problems and may trip the zero-sequence protection. The other terms are positive-sequence components which behave just as fundamental currents. They are not within the scope of harmonics and can be regulated by the decoupling current controller. It has been found that the current harmonic magnitude is affected by sub-module capacitance, phase reactance and system operating frequencies. Solutions to suppress M^3C harmonics have been provided including a proper selection of circuit element values and a zero-sequence current mitigation controller. The procedure used in the analysis is general for other applications apart from FFT. It is helpful for M^3C modelling and control method development. All theoretical analysis has been validated by RTDS time domain simulations.

7.2 Future Work

A list of possible future work is discussed as follows:

• In Chapter 4, the economic analysis is carried out based on a point-to-point topology connecting the offshore wind farm to the onshore grid. As the development of offshore wind power, offshore grids are very likely to be developed. It would be interesting to analyse the economic aspects when a more complex topology is adopted, that is to say, AC or DC offshore grids. Furthermore, a hybrid system may be formed and taken into consideration. Besides, the cost model can be refined. For the sake of simplicity, the current analysis assumes that the O&M cost is identical each year through the project life time. However, in reality the O&M cost may be lower for the first few years, and increases as equipment aging. More study could be carried out to consider this trend into the model.

• The prerequisite of power system small signal analysis is the small signal models of all the components in the system. In chapter 5, a small signal model of M^3C has been developed, with simple interfaces with external AC systems and control system. The next step could be investigating how a M^3C FFT system would affect the small signal stability of an existing power system. The impact on the oscillation modes and damping could be analysed. Also, the case can be considered as the renewable offshore wind power replacing traditional fossil fuel power. The total inertial of the system would be lower and the controllability from the synchronous generators would decrease. It would be interesting to investigate the stability of such a system with a high penetration of offshore wind power integrated by M^3C FFT.

• Chapter 6 has presented a harmonic analysis of M^3C at three-phase balanced state. One deficiency is that the analysis is supported only by simulations and no hardware experiment has been done. When conditions permit, a prototype of M^3C should be developed. Besides, the converter could be slightly three-phase unbalanced for instance due to sub-module discrepancy. The system would also be unbalanced during the fault period. It would be possible to further look into the harmonic profile under three-phase unbalance circumstance.

If required, a controller might need to be developed to take care of the issue brought by unbalanced situation.

LIST OF REFERENCES

[1] M. Z. Jacobson, *et al.*, "100% clean and renewable wind, water, and sunlight all-sector energy roadmaps for 139 countries of the world," *Joule*, vol. 1, no. 1, pp. 108-121, 2017.

[2] REN21, "Renewables 2018 Global Status Report," 2018.

[3] J. Twidell and T. Weir, *Renewable energy resources*. Routledge, 2015.

[4] UK Government Department for Business Energy & Industrial Strategy, "Renewable electricity capacity and generation," 2019, Available: https://www.gov.uk/government/statistics/energy-trends-section-6-renewables.

[5] Wind Europe, "Offshore Wind in Europe: Key Trends and Statistics 2018," 2018.

[6] The Crown Estate, "Offshore Wind Operational Report," 2017.

[7] Mark Macaskill. (2018). *Too much wind shocks electric bill payers*. Available: https://www.thetimes.co.uk/article/too-much-wind-shocks-electric-bill-payers-lcgw3cwpz

[8] Z. Yang, K. Li, and A. Foley, "Computational scheduling methods for integrating plug-in electric vehicles with power systems: A review," *Renewable and Sustainable Energy Reviews*, vol. 51, pp. 396-416, 2015.

[9] E. Muljadi, *et al.*, *Understanding inertial and frequency response of wind power plants*. IEEE, 2012.

[10] Q.-C. Zhong and G. Weiss, "Synchronverters: Inverters that mimic synchronous generators," *IEEE Trans. on Industrial Electronics*, vol. 58, no. 4, pp. 1259-1267, 2011.

[11] J. Zhu, *et al.*, "Inertia emulation control strategy for VSC-HVDC transmission systems," *IEEE Trans. Power Syst*, vol. 28, no. 2, pp. 1277-1287, 2013.

[12] Wind Europe, "Offshore Wind in Europe: Key Trends and Statistics 2017," 2017.

[13] *The Wind Power Database*. Available: https://www.thewindpower.net/country-datasheet-windfarms-8-united-kingdom.php

[14] J. A. Baroudi, V. Dinavahi, and A. M. Knight, "A review of power converter topologies for wind generators," *Renewable Energy*, vol. 32, no. 14, pp. 2369-2385, 2007.

[15] N. B. Negra, J. Todorovic, and T. Ackermann, "Loss evaluation of HVAC and HVDC transmission solutions for large offshore wind farms," *Electric power systems research*, vol. 76, no. 11, pp. 916-927, 2006.

[16] C. Guo, *et al.*, "An Evolved Capacitor-Commutated Converter Embedded With Antiparallel Thyristors Based Dual-Directional Full-Bridge Module," *IEEE Trans.s on Power Delivery*, vol. 33, no. 2, pp. 928-937, 2018.

[17] B. R. Andersen and L. Xu, "Hybrid HVDC system for power transmission to island networks," *IEEE Trans.s on Power Delivery*, vol. 19, no. 4, pp. 1884-1890, 2004.

[18] P. Bresesti, *et al.*, "HVDC Connection of Offshore Wind Farms to the Transmission System," *IEEE Trans.s on Energy Conversion*, vol. 22, no. 1, pp. 37-43, 2007.

[19] G. Shi, *et al.*, "Coordinated control of multi-terminal VSC-HVDC transmission for large offshore wind farms," in *Proceedings of The 7th International Power Electronics and Motion Control Conference*, 2012, vol. 2, pp. 1278-1282.

[20] X. Wang, "The fractional frequency transmission system," *Proc. Inst. Elect. Eng. Jap. Power Energy*, pp. 53-58, 1994.

[21] J. Li and X. P. Zhang, "Small signal stability of fractional frequency transmission system with offshore wind farms," *IEEE Trans. on Sustainable Energy*, vol. 7, no. 4, pp. 1538-1546, 2016.

[22] X. Wang, C. Cao, and Z. Zhou, "Experiment on fractional frequency transmission system," *IEEE Trans. on Power Systems*, vol. 21, no. 1, pp. 372-377, 2006.

[23] J. Ruddy, R. Meere, and T. O'Donnell, "Low frequency AC transmission for offshore wind power: A review," *Renewable and Sustainable Energy Reviews*, vol. 56, pp. 75-86, 2016.

[24] R. W. Erickson and O. A. Al-Naseem, "A new family of matrix converters," in *The 27th Annual Conf. of the IEEE*, 2001, vol. 2, pp. 1515-1520.

[25] K. Sharifabadi, *et al.*, *Design, control, and application of modular multilevel converters for HVDC transmission systems*. John Wiley & Sons, 2016.

[26] Wikipedia. *Insulated-gate bipolar transistor*. Available: https://en.wikipedia.org/wiki/Insulated-gate_bipolar_transistor

[27] S. Liu, *et al.*, "A Decoupled Control Strategy of Modular Multilevel Matrix Converter for Fractional Frequency Transmission System," *IEEE Trans.s on Power Delivery*, vol. 32, no. 4, pp. 2111-2121, 2017.

[28] IRENA, "Renewable Power Generation Costs in 2017."

[29] A. G. Gonzalez-Rodriguez, "Review of offshore wind farm cost components," *Energy for Sustainable Development*, vol. 37, pp. 10-19, 2017.

[30] B. C. Ummels, E. Pelgrum, and W. L. Kling, "Integration of large-scale wind power and use of energy storage in the netherlands' electricity supply," *IET Renewable Power Generation*, vol. 2, no. 1, pp. 34-46, 2008.

[31] E. Haghi, M. Fwoler, and K. Raahemifar, "Economic analysis of hydrogen production in context of a microgrid," in *2017 IEEE International Conference on Smart Energy Grid Engineering (SEGE)*, 2017, pp. 79-84.

[32] H. Tebibel, "Wind Turbine Power System for Hydrogen Production and Storage: Techno-economic Analysis," in *2018 International Conference on Wind Energy and Applications in Algeria (ICWEAA)*, 2018, pp. 1-6.

[33] B. F. Ronad and S. H. Jangamshetti, "Optimal cost analysis of wind-solar hybrid system powered AC and DC irrigation pumps using HOMER," in *2015 International Conference on Renewable Energy Research and Applications (ICRERA)*, 2015, pp. 1038-1042.

[34] X. Zhao, Z. Yan, and X. Zhang, "A Wind-Wave Farm System With Self-Energy Storage and Smoothed Power Output," *IEEE Access*, vol. 4, pp. 8634-8642, 2016.

[35] C. Pérez-Collazo, D. Greaves, and G. Iglesias, "A review of combined wave and offshore wind energy," *Renewable and Sustainable Energy Reviews*, vol. 42, pp. 141-153, 2015.

[36] M. R. Kabir, *et al.*, "Comparative life cycle energy, emission, and economic analysis of 100 kW nameplate wind power generation," *Renewable Energy*, vol. 37, no. 1, pp. 133-141, 2012.

[37] L. Wang, *et al.*, "Benefit Evaluation of Wind Turbine Generators in Wind Farms Using Capacity-Factor Analysis and Economic-Cost Methods," *IEEE Trans.s on Power Systems*, vol. 24, no. 2, pp. 692-704, 2009.

[38] E. Dupont, R. Koppelaar, and H. Jeanmart, "Global available wind energy with physical and energy return on investment constraints," *Applied Energy*, vol. 209, pp. 322-338, 2018.

[39] W. Ma, X. Xue, and G. Liu, "Techno-economic evaluation for hybrid renewable energy system: Application and merits," *Energy*, vol. 159, pp. 385-409, 2018.

[40] OWPB, "Offshore Wind Programme Board Annual Report 2015," 2015.

[41] Wind Europe, "Wind in power 2017: Annual combined onshore and offshore wind energy statistics," 2017.

[42] D. Elliott, *et al.*, "A comparison of AC and HVDC options for the connection of offshore wind generation in Great Britain," *IEEE Trans. Power Delivery*, vol. 31, pp. 798-809, 2016.

[43] X. Xiang, M. Merlin, and T. Green, "Cost analysis and comparison of HVAC, LFAC and HVDC for offshore wind power connection," in *12th IET Int. Conf. AC DC Power Transmission*, 2016, pp. 1-6.

[44] J. Ruddy, R. Meere, and T. O'Donnell, "A Comparison of VSC-HVDC with Low Frequency AC for Offshore Wind Farm Design and Interconnection," *Energy Procedia*, vol. 80, pp. 185-192, 2015.

[45] P. Kundar, *Power System Stability and Control*. New York: McGraw-Hill, 1994.

[46] X.-F. Wang, Y. Song, and M. Irving, *Modern power systems analysis*. Springer Science & Business Media, 2010.

[47] C. Schauder and H. Mehta, "Vector analysis and control of advanced static VAr compensators," *IEE Proc. C - Generation, Transmission and Distribution*, vol. 140, no. 4, pp. 299-306, 1993.

[48] R. Pena, J. Clare, and G. Asher, "Doubly fed induction generator using back-to-back PWM converters and its application to variable-speed wind-energy generation," *IEE Proceedings-Electric Power Applications*, vol. 143, no. 3, pp. 231-241, 1996.

[49] L. Xu, L. Yao, and C. Sasse, "Grid Integration of Large DFIG-Based Wind Farms Using VSC Transmission," *IEEE Trans.s on Power Systems*, vol. 22, no. 3, pp. 976-984, 2007.

[50] Q. Hao, *et al.*, "Reduced-Order Small-Signal Models of Modular Multilevel Converter and MMC-Based HVdc Grid," *IEEE Trans.s on Industrial Electronics*, vol. 66, no. 3, pp. 2257-2268, 2019.

[51] F. Wu, *et al.*, "Small signal stability analysis and optimal control of a wind turbine with doubly fed induction generator," *IET Generation, Transmission & Distribution*, vol. 1, no. 5, pp. 751-760, 2007.

[52] Y. Liu, *et al.*, "Small-Signal Model-Based Control Strategy for Balancing Individual DC Capacitor Voltages in Cascade Multilevel Inverter-Based STATCOM," *IEEE Trans.s on Industrial Electronics*, vol. 56, no. 6, pp. 2259-2269, 2009.

[53] C. Andalib-Bin-Karim, *et al.*, "Small signal stability analysis of power system equipped with VSC based back to back HVDC," in *2015 International Conference on Electrical Engineering and Information Communication Technology (ICEEICT)*, 2015, pp. 1-6: IEEE.

[54] T. Li, A. M. Gole, and C. Zhao, "Harmonic instability in MMC-HVDC converters resulting from internal dynamics," *IEEE Trans. on Power Delivery*, vol. 31, no. 4, pp. 1738-1747, 2016.

[55] G. B. Diaz, J. A. Suul, and S. D. Arco, "Small-signal state-space modeling of modular multilevel converters for system stability analysis," in *2015 IEEE Energy Conversion Congress and Exposition (ECCE)*, 2015, pp. 5822-5829.

[56] A. Jamshidifar and D. Jovcic, "Small-Signal Dynamic DQ Model of Modular Multilevel Converter for System Studies," *IEEE Trans. on Power Delivery*, vol. 31, no. 1, pp. 191-199, 2016.

[57] S. Liu, M. Saeedifard, and X. Wang, "Analysis and control of the modular multilevel matrix converter under unbalanced grid conditions," *IEEE Journal of Emerging and Selected Topics in Power Electronics*, vol. 6, no. 4, pp. 1979-1989, 2018.

[58] Y. Miura, *et al.*, "Modular multilevel matrix converter for low frequency AC transmission," in *IEEE 10th Int. Conf. on Power Electronics and Drive Systems* 2013, pp. 1079-1084.

[59] W. Kawamura, M. Hagiwara, and H. Akagi, "Control and experiment of a modular multilevel cascade converter based on triple-star bridge cells," *IEEE Trans. on Industry Applications*, vol. 50, no. 5, pp. 3536-3548, 2014.

[60] W. Kawamura, *et al.*, "AC-Inductors design for a modular multilevel TSBC converter, and performance of a low-speed high-torque motor drive using the converter," *IEEE Trans. on Industry Applications*, vol. 53, no. 5, pp. 4718-4729, 2017.

[61] Q. Xu, *et al.*, "Analysis and control of M3C-based UPQC for power quality improvement in medium/high-voltage power grid," *IEEE Trans. on Power Electronics*, vol. 31, no. 12, pp. 8182-8194, 2016.

[62] S. Hillmansen and C. Roberts, "Energy storage devices in hybrid railway vehicles: a kinematic analysis," *Proceedings of the Institution of Mechanical Engineers, Part F: Journal of Rail and Rapid Transit*, vol. 221, no. 1, pp. 135-143, 2007.

[63] S. Lu, *et al.*, "Increasing the Regenerative Braking Energy for Railway Vehicles," *IEEE Trans.s on Intelligent Transportation Systems*, vol. 15, no. 6, pp. 2506-2515, 2014.

[64] W. Kawamura, M. Hagiwara, and H. Akagi, "Control and Experiment of a Modular Multilevel Cascade Converter Based on Triple-Star Bridge Cells," *IEEE Trans.s on Industry Applications*, vol. 50, no. 5, pp. 3536-3548, 2014.

[65] Y. Miura, *et al.*, "Control scheme of the modular multilevel matrix converter using space vector modulation for wide frequency range operation," in *2017 IEEE Energy Conversion Congress and Exposition (ECCE)*, 2017, pp. 1084-1091.

[66] F. Kammerer, J. Kolb, and M. Braun, "Fully decoupled current control and energy balancing of the modular multilevel matrix converter," in *15th International Power Electronics and Motion Control Conference* 2012, pp. LS2a. 3-1 - 3-8.

[67] S. Liu, *et al.*, "A decoupled control strategy of modular multilevel matrix converter for fractional frequency transmission system," *IEEE Trans. on Power Delivery*, vol. 32, no. 4, pp. 2111-2121, 2017.

[68] W. Yao, J. Liu, and Z. Lu, "Distributed Control for the Modular Multilevel Matrix Converter," *IEEE Trans.s on Power Electronics*, vol. 34, no. 4, pp. 3775-3788, 2019.

[69] S. Liu and et al, "A Current Reallocation Strategy to Attenuate the Peak Arm Current of the Modular Multilevel Matrix Converter," *IEEE Journal of Emerging and Selected Topics in Power Electronics,* pp. 1-1, 2019.

[70] R. Alaei, S. A. Khajehoddin, and W. Xu, "Control and experiment of AC/AC sparse modular multilevel converter," *IEEE Trans. on Power Delivery*, vol. 32, no. 3, pp. 1527-1534, 2017.

[71] B. Fan and et al, "Optimized Branch Current Control of Modular Multilevel Matrix Converters Under Branch Fault Conditions," *IEEE Trans. on Power Electronics,* vol. 33, no. 6, pp. 4578-4583, 2018.

[72] M. Diaz, *et al.*, "Vector Control of a Modular Multilevel Matrix Converter Operating Over the Full Output-Frequency Range," *IEEE Trans.s on Industrial Electronics,* vol. 66, no. 7, pp. 5102-5114, 2019.

[73] C. Melendez, *et al.*, "Frequency Support Control of a Modular Multilevel Matrix Converter based Wind Energy Conversion System," in *IEEE International Conference on Automation/XXIII Congress of the Chilean Association of Automatic Control (ICA-ACCA)*, 2018, pp. 1-6.

[74] P. Sun, *et al.*, "The harmonic analysis and the arm capacitor parameters selection of module multilevel matrix converter," in *IEEE PES Asia-Pacific Power and Energy Engineering Conf. (APPEEC)*, 2016, pp. 1617-1621.

[75] J. Ma, *et al.*, "Modular multilevel matrix converter for offshore low frequency AC transmission system," in *IEEE 26th Int. Symposium on Industrial Electronics*, 2017, pp. 768-774.

[76] L. Sainz, *et al.*, "Effect of wind turbine converter control on wind power plant harmonic response and resonances," *IET Electric Power Applications,* vol. 11, no. 2, pp. 157-168, 2017.

[77] H. Saad, *et al.*, "On resonances and harmonics in HVDC-MMC station connected to AC grid," *IEEE Trans. on Power Delivery*, vol. 32, no. 3, pp. 1565-1573, 2017.

[78] C. Buchhagen, *et al.*, "BorWin1-First experiences with harmonic interactions in converter dominated grids," in *Proceedings of International ETG Congress*, 2015, pp. 1-7.

[79] Q. Tu, Z. Xu, and L. Xu, "Reduced switching-frequency modulation and circulating current suppression for modular multilevel converters," *IEEE Trans. on Power Delivery*, vol. 26, no. 3, pp. 2009-2017, 2011.

[80] S. Pengwei, *et al.*, "The harmonic analysis and the arm capacitor parameters selection of module multilevel matrix converter," in *IEEE PES Asia-Pacific Power and Energy Engineering Conf. (APPEEC)*, 2016, pp. 1617-1621.

[81] M. Guan, Z. Xu, and C. Hairong, "Control and modulation strategies for modular multilevel converter based HVDC system," in *IECON 2011 - 37th Annual Conference of the IEEE Industrial Electronics Society*, 2011, pp. 849-854.

[82] S. Shang, *et al.*, "Research on modeling and control strategy of modular multilevel matrix converter supplying passive networks," in *IEEE PES Asia-Pacific Power and Energy Engineering Conf.(APPEEC)*, 2016, pp. 1974-1978.

[83] *Introduction of Real Time Digital Simulator*. Available: https://www.rtds.com/about/company-profile/

[84] H. Khatib, *Economic evaluation of projects in the electricity supply industry* (no. 44). IET, 2003.

[85] T. J. Stehly, D. M. Heimiller, and G. N. Scott, "2016 Cost of Wind Energy Review," National Renewable Energy Lab.(NREL), Golden, CO (United States)2017.

[86] RenewablesFirst. *Wind power learning center* Available: http://www.renewablesfirst.co.uk/windpower/windpower-learning-centre/how-much-does-a-farm-wind-turbine-small-wind-farm-turbine-cost/

[87] X. Wang, *et al.*, "Feasibility of integrating large wind farm via fractional frequency transmission system a case study," *International Trans.s on Electrical Energy Systems*, vol. 24, no. 1, pp. 64-74, 2014.

[88] X. Zhang, *et al.*, "Selection of the rated frequency for fractional frequency offshore wind power system," in *2017 IEEE Conference on Energy Internet and Energy System Integration (EI2)*, 2017, pp. 1-6.

[89] Vestas. *V164 8MW Technical Brochure*. Available: http://www.homepages.ucl.ac.uk/~uceseug/Fluids2/Wind_Turbines/Turbines/V164-8MW.pdf

[90] NorthSeaGrid, "Annexes to the Final Report," 2014, Available: http://northseagrid.info/sites/default/files/NorthSeaGrid_Final_Report_Annexes.pdf.

[91] S. Liu, *et al.*, "Integrating offshore wind power via fractional frequency transmission system," *IEEE Trans. on Power Delivery*, vol. 32, no. 3, pp. 1253-1261, 2017.

[92] D. Woodford, "Symmetrical monopole VSC transmission," *Electranix technical paper*, 2014.

[93] Working Group B1.40, "CIGRE Report 610: Offshore Generation Cable Connections," 2015.

[94] A. F. M. Luckett, "Economic Analysis of Large Submarine Cables," Edif ERA2016.

[95] I. E. Commission, "Time Based Availability for Wind Turbines (IEC 61400-26-1)," ed, 2010.

[96] D. McMillan and G. Ault, "Specification of reliability benchmarks for offshore wind farms," *Proceedings of the European safety and reliability*, pp. 22-25, 2008.

[97] J. Carroll, A. McDonald, and D. McMillan, "Reliability comparison of wind turbines with DFIG and PMG drive trains," *IEEE Trans.s on Energy Conversion*, vol. 30, no. 2, pp. 663-670, 2015.

[98] Working Group B3.36, "CIGRE Report 612: Special Considerations for AC Collector Systems and Substations Associated with HVDC," 2015.

[99] M. Bennett, N. Dhaliwal, and A. Leirbukt, "A survey of the reliability of HVDC systems throughout the world," *44rd CIGRE Session, Paris, France*.

[100] 4Coffshore. *Offshore converter events*. Available: https://www.4coffshore.com/transmission/

[101] L. L. Rademakers, H. H. Braam, and T. T. Obdam, "Operation and maintenance of offshore wind energy systems," in *Wind Energy Systems*: Elsevier, 2011, pp. 546-583.

[102] B. Van Eeckhout, *et al.*, "Economic comparison of VSC HVDC and HVAC as transmission system for a 300 MW offshore wind farm," *European Trans.s on Electrical Power*, vol. 20, no. 5, pp. 661-671, 2010.

[103] J. Tamura, "Calculation method of losses and efficiency of wind generators," in *Wind energy conversion systems*: Springer, 2012, pp. 25-51.

[104] A. Papadopoulos, *et al.*, "Collection and transmission losses of offshore wind farms for optimization purposes," in *Energy Conversion Congress and Exposition (ECCE), 2015 IEEE*, 2015, pp. 6724-6732: IEEE.

[105] P. S. Jones and C. C. Davidson, "Calculation of power losses for MMC-based VSC HVDC stations," in *Power Electronics and Applications (EPE), 2013 15th European Conference on*, 2013, pp. 1-10: IEEE.

[106] Energynumbers. *Offshore wind capacity factors*. Available: http://energynumbers.info/uk-offshore-wind-capacity-factors

[107] Elexon. (2018). *Balancing mechanism reporting system*. Available: http://www.bmreports.com/

[108] Y. Tang, *et al.*, "Capacitor Selection for Modular Multilevel Converter," *IEEE Trans. on Industry Applications*, vol. 52, no. 4, pp. 3279-3293, 2016.

[109] M. Zygmanowski, B. Grzesik, and R. Nalepa, "Capacitance and inductance selection of the modular multilevel converter," in *15th European Conf. on Power Electronics and Applications (EPE)*, 2013, pp. 1-10.

[110] W. Zhou and et al, "Common-mode voltage injection-based nearest level modulation with loss reduction for modular multilevel converters," *IET Renewable Power Generation*, vol. 10, no. 6, pp. 798-806, 2016.

[111] F. Deng and Z. Chen, "A Control Method for Voltage Balancing in Modular Multilevel Converters," *IEEE Trans. on Power Electronics*, vol. 29, no. 1, pp. 66-76, 2014.

[112] J. Z. Zhou, *et al.*, "Impact of Short-Circuit Ratio and Phase-Locked-Loop Parameters on the Small-Signal Behavior of a VSC-HVDC Converter," *IEEE Trans. on Power Delivery*, vol. 29, no. 5, pp. 2287-2296, 2014.

[113] G. O. Kalcon, *et al.*, "Small-Signal Stability Analysis of Multi-Terminal VSC-Based DC Transmission Systems," *IEEE Trans. on Power Systems*, vol. 27, no. 4, pp. 1818-1830, 2012.

[114] J. Peralta and et al, "Detailed and Averaged Models for a 401-Level MMC–HVDC System," *IEEE Trans. on Power Delivery*, vol. 27, no. 3, pp. 1501-1508, 2012.

[115] E. Ebrahimzadeh, *et al.*, "Harmonic instability source identification in large wind farms," in *2017 IEEE Power & Energy Society General Meeting*, 2017, pp. 1-5.

[116] N. P. Strachan and D. Jovcic, "Stability of a variable-speed permanent magnet wind generator with weak AC grids," *IEEE Trans. on Power Delivery*, vol. 25, no. 4, pp. 2779-2788, 2010.

[117] X. Wang, F. Blaabjerg, and W. Wu, "Modeling and analysis of harmonic stability in an AC power-electronics-based power system," *IEEE Trans. on Power Electronics*, vol. 29, no. 12, pp. 6421-6432, 2014.

[118] W. Hu, *et al.*, "Modeling and control of zero-sequence current in multiple grid connected converter," in *IEEE PESC Power Electronics Specialists Conference*, 2008, pp. 2064-2069.

[119] B. Gao, *et al.*, "Differential protection for an outgoing transformer of large-scale doubly fed induction generator-based wind farms," *Energies*, vol. 7, no. 9, pp. 5566-5585, 2014.

[120] B. Zhang, *et al.*, "Impact of wind farm integration on relay protection (6): analysis of distance protection for wind farm outgoing transmission line," *Electric Power Automation Equipment*, vol. 6, pp. 1-6, 2013.

[121] M. Heathcote, *J & P transformer book*. Elsevier, 2011.

[122] M. Diaz, *et al.*, "Modelling and control of the modular multilevel matrix converter and its application to wind energy conversion systems," in *IECON 2016 - 42nd Annual Conference of the IEEE Industrial Electronics Society*, 2016, pp. 5052-5057.

[123] M. Diaz, *et al.*, "Control of wind energy conversion systems based on the modular multilevel matrix converter," *IEEE Trans. on Industrial Electronics*, vol. 64, no. 11, pp. 8799-8810, 2017.

[124] Y. Wang, *et al.*, "Open-Winding Power Conversion Systems Fed by Half-Controlled Converters," *IEEE Trans. on Power Electronics*, vol. 28, no. 5, pp. 2427-2436, 2013.

LIST OF PUBLICATIONS

Conference Paper:

1. Jiajie Luo, Kai Lin, Jianing Li, Ying Xue and Xiao-Ping Zhang, "Cost Analysis and Comparison between Modular Multilevel Converter (MMC) and Modular Multilevel Matrix Converter (M^3C) for Offshore Wind Power Transmission", *15th IET Int. Conf. AC DC Power Transmission,* 2019.

Journal Papers:

2. Jiajie Luo, Xiao-Ping Zhang and Ying Xue, "Small Signal Model of Modular Multilevel Matrix Converter for Fractional Frequency Transmission System", *IEEE Access,* 2019.

3. Jiajie Luo, Xiao-Ping Zhang, Ying Xue and Kanghui Gu, "Harmonic Analysis of Modular Multilevel Matrix Converter for Fractional Frequency Transmission System", *IEEE Transaction on Power Delivery (accepted).*

4. Kanghui Gu, Feng Wu, Xiao-Ping Zhang, Ping Ju, Jiajie Luo and Jianing Li, "SSR Analysis of DFIG-based Wind Farm with VSM Control Strategy", *IEEE Access (accepted).*

5. Xianxian Zhao, Ying Xue, Xiao-Ping Zhang and Jiajie Luo, "Isolation and Suppression of Forced Oscillations by Controlling Wind Farm Kinetic Energy", *IEEE Transaction on Power System (under review).*

APPENDIX A

Table A.1 Circuit and control parameters

Symbol	Quantity	Value
f_1	Fractional frequency	20 Hz
f_3	System frequency	60 Hz
V_{l-l}	Rated AC system voltage	33 kV
N	Sub-module number each arm	40
L	Inductance	15 mL
C	Sub-module capacitance	5 mF
R	Arm resistance	0.25 Ω
U_{dcref}	Capacitor voltage reference	1.5 kV
P_{20ref}	Active power reference 20 Hz	30 MV
I_{qref}	Q axis current reference	0 kA
k_{p1}	Proportional gain of PI controller 1	0.025
k_{i1}	Integral gain of PI controller 1	1
k_{p2}	Proportional gain of PI controller 2	100
k_{i2}	Integral gain of PI controller 2	20
k_{p3},	Proportional gain of PI controller 3	100
k_{i3}	Integral gain of PI controller 3	20
k_{p4}	Proportional gain of PI controller 4	0.5
k_{i4}	Integral gain of PI controller 4	10
k_{p5}	Proportional gain of PI controller 5	50
k_{i5}	Integral gain of PI controller 5	50
k_{p6}	Proportional gain of PI controller 6	50
k_{i6}	Integral gain of PI controller 6	50
k_{ppll}	PLL proportional gain	5
k_{ipll}	PLL integral gain	100

T_{mea}	First order time constant of measurement	0.01s
k_{pz1}	Mitigation controller proportional gain 1	1.0
k_{iz1}	Mitigation controller integral gain	1.2
k_{pz2}	Mitigation controller proportional gain 2	0.2

APPENDIX B

This appendix gives an explanation of the simulation system of M^3C in RTDS.

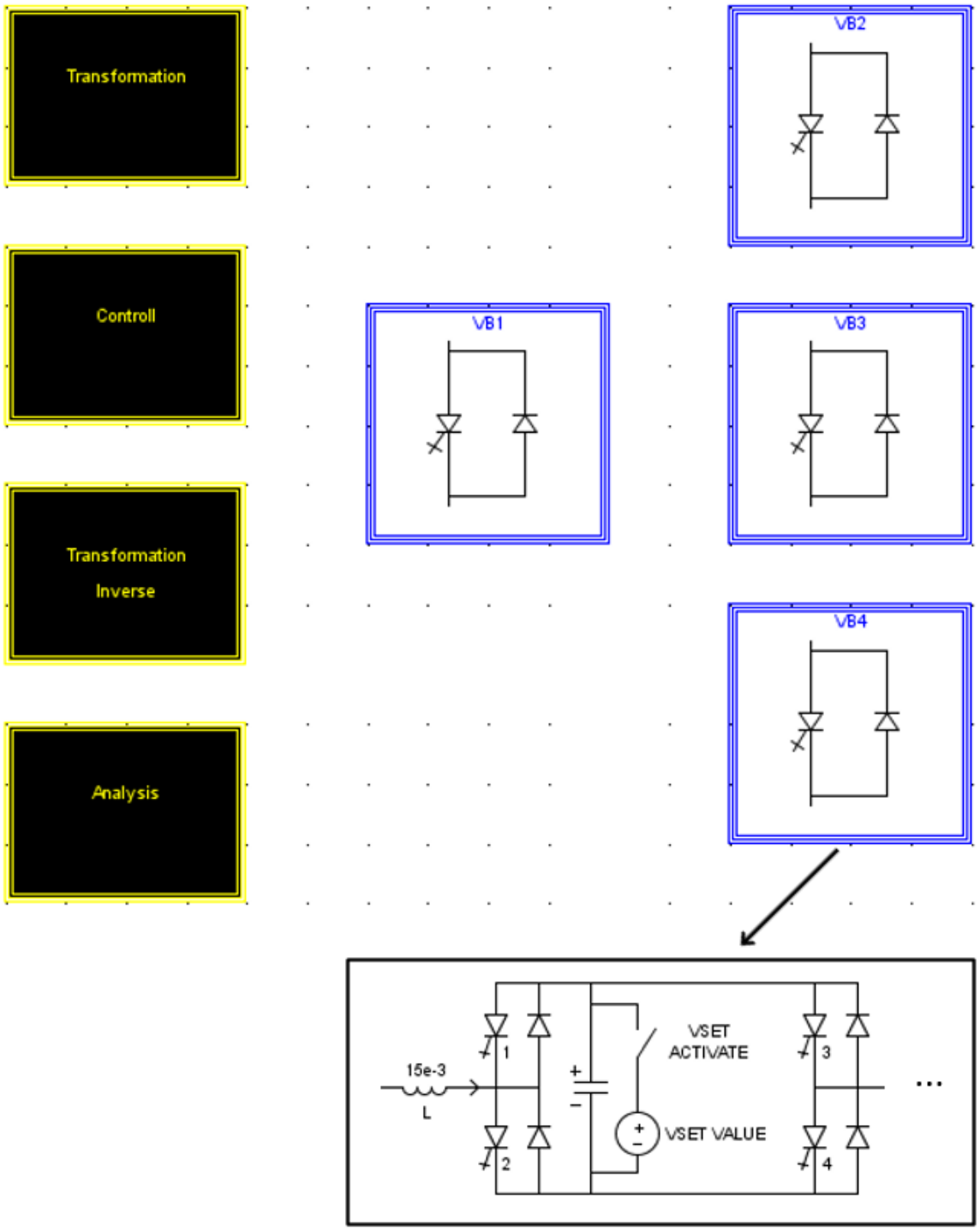

Fig. B.1 Time domain simulation system layout in RTDS.

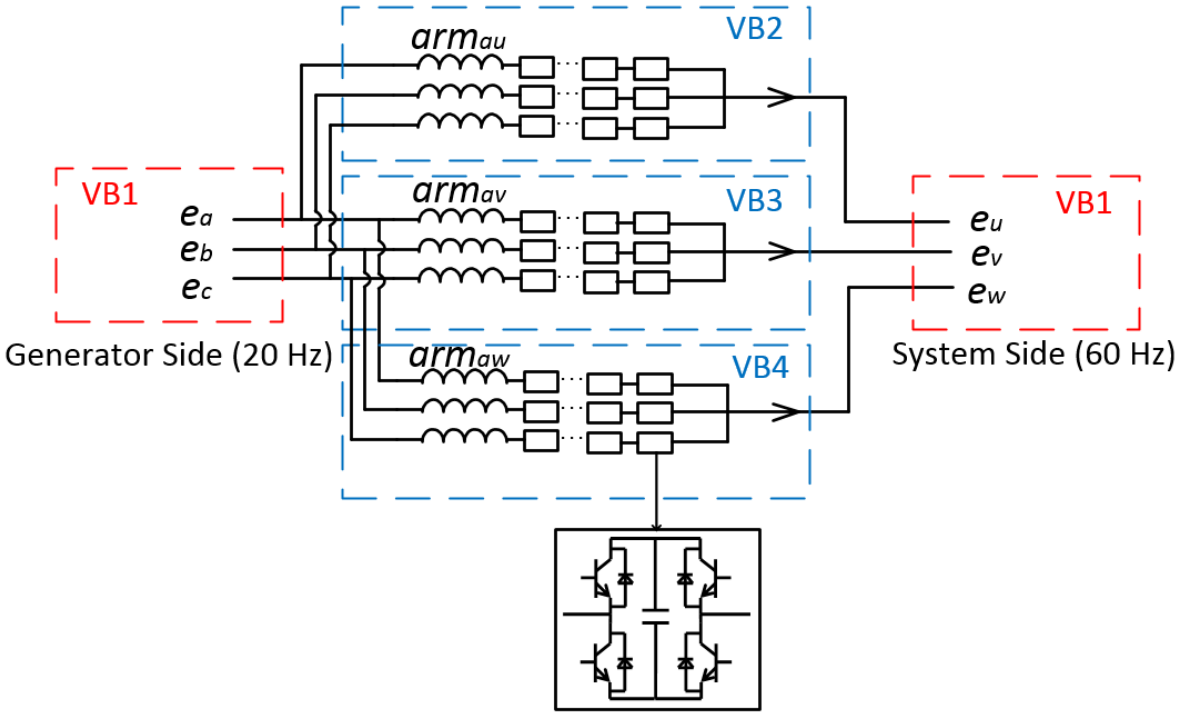

Fig. B.2 Corresponding schematic diagram of the M^3C simulation system.

The M^3C simulated in RTDS is a detailed model for electromagnetic transient phenomena study. The system layout is shown in Fig. B.1 where there are four small signal boxes (VB1 – VB4) and several control and analysis blocks on the left of the figure. Fig. B.2 is a corresponding schematic diagram of the time domain simulation system. AC systems on both sides are placed in the small signal box VB1, and nine arms of the M^3C are symmetrically allocated in VB2, VB3 and VB4 respectively. Each arm is formed of forty full bridge sub-module. The offshore generator side AC system is at 20 Hz and the grid side is at 60 Hz. The active power flow direction is from the 20 Hz side to the 60 Hz side. A small simulation time step of 3 microseconds is used to accurately simulate the switching dynamics of power electronics.

In the ‘Transformation’ block, signals are transformed from time-varying to time-invariant using Clarke transformation and Park transformation. An example of the signal transformation implemented in time domain simulation is shown in Fig. B.3. Time-invariant signals are favoured for control purpose and the signals after transformation are fed into the DQ decoupling controllers. The controllers locate in the ‘Control’ block. Fig. B.4 is the NLM implementation in RTDS which is introduced in Section 3.3. Fig. B.5 shows the implementation of the decoupling control in time domain simulation for the 20 Hz side D axis. The control objective is to regulate the transmitted active power on the 20 Hz side to the active power reference given. The active power difference is fed to the PI controller and the output is the 20 Hz side active current reference which is used for the inner loop. The inner loop current controller follows the active current reference and the output is the D axis voltage reference. Next, the ‘Transformation Inverse’ block transforms the voltage references back in ABC frame and then switching signals are generated after signal modulation. The ‘Analysis’ block is created to realise some supporting functions, including extracting components at certain frequencies from a signal (e.g., extracting the DC and 40 Hz components from the sub-module capacitor voltage), computing the positive-sequence, negative-sequence and zero-sequence components of three-phase quantities, and some miscellaneous calculations.

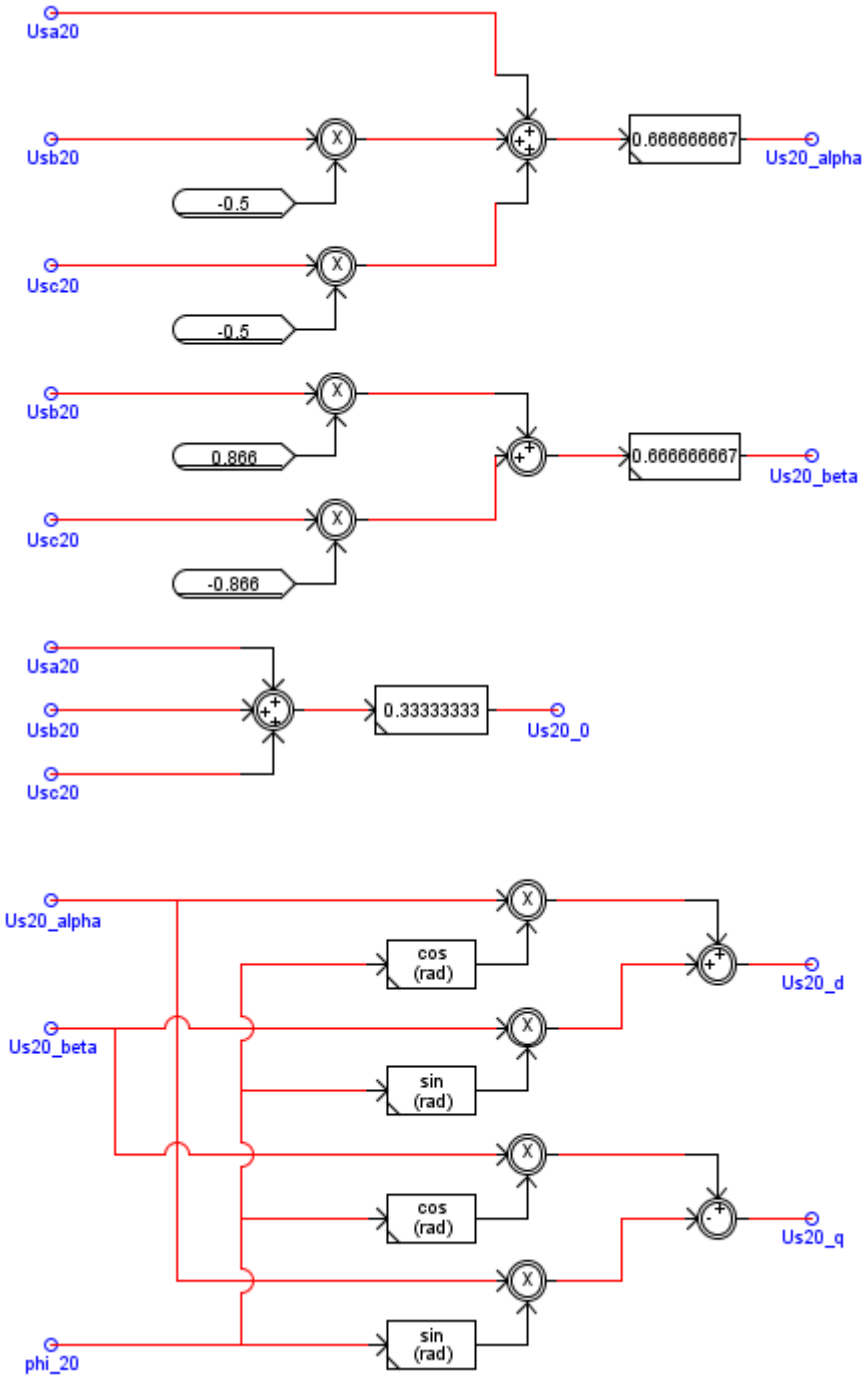

Fig. B.3 Example Clarke and Park transformation implemented in time domain simulation.

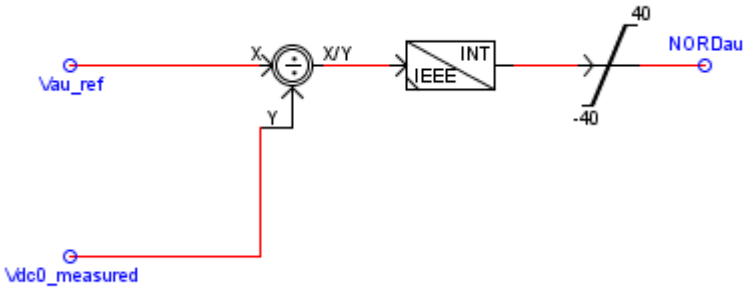

Fig. B.4 Example NLM block of an arm implemented in time domain simulation.

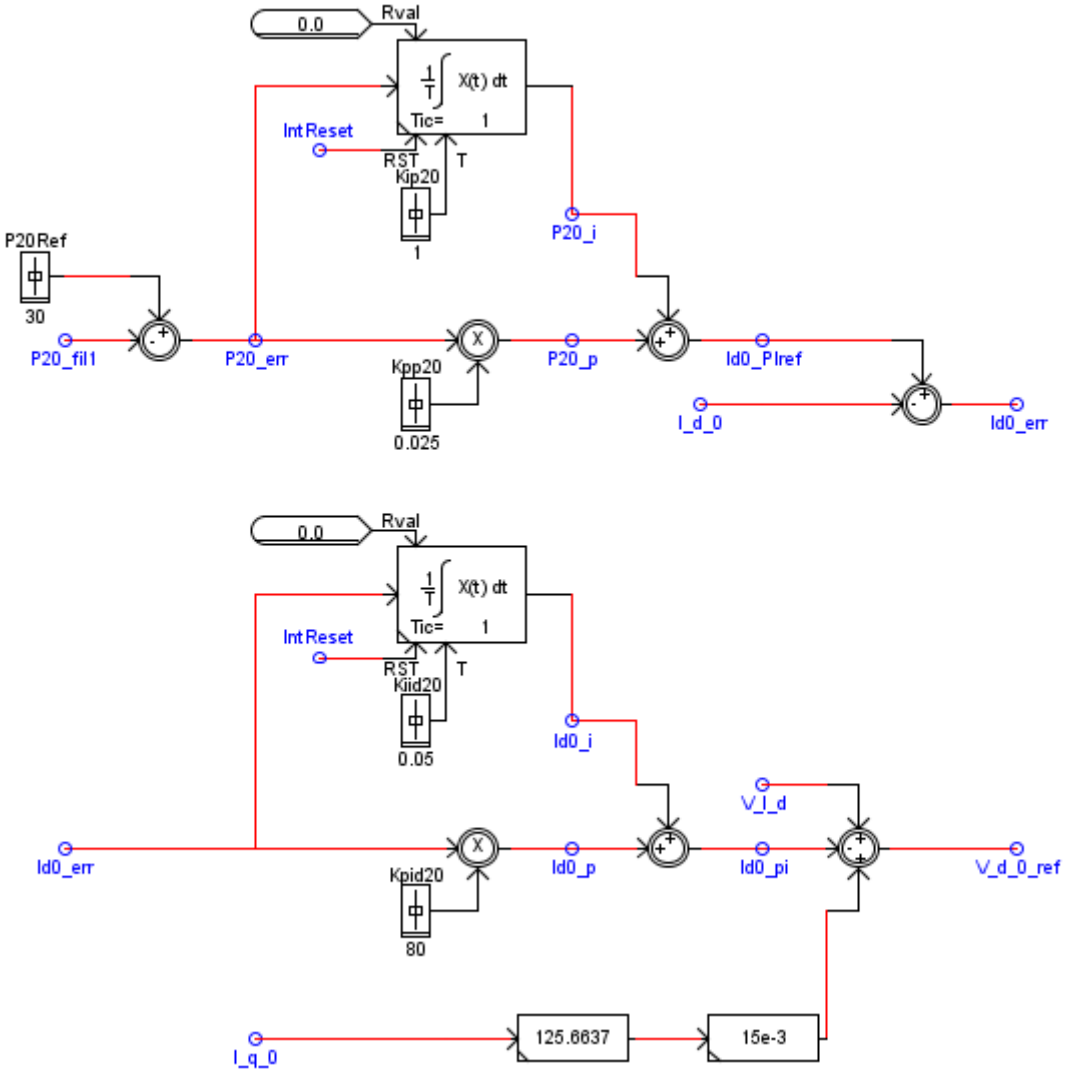

Fig. B.5 Example DQ decoupling control implemented in time domain simulation.

APPENDIX C

Detailed derivation of the small signal model:

The full Kirchhoff's law equations can be expressed as:

$$\begin{bmatrix} u_a & u_a & u_a \\ u_b & u_b & u_b \\ u_c & u_c & u_c \end{bmatrix} = \begin{bmatrix} v_{au} & v_{av} & v_{aw} \\ v_{bu} & v_{bv} & v_{bw} \\ v_{cu} & v_{cv} & v_{cw} \end{bmatrix} + \left(R + L\frac{d}{dt}\right) \begin{bmatrix} i_{au} & i_{av} & i_{aw} \\ i_{bu} & i_{bv} & i_{bw} \\ i_{cu} & i_{cv} & i_{cw} \end{bmatrix} + \begin{bmatrix} u_u & u_v & u_w \\ u_u & u_v & u_w \\ u_u & u_v & u_w \end{bmatrix} \qquad \begin{pmatrix} C1 & C2 & C3 \\ C4 & C5 & C6 \\ C7 & C8 & C9 \end{pmatrix}$$

Apply ABC − αβ0 transformation to C1 - C3, C4 - C6, and C7 - C9 respectively and extract the zero sequence equations:

$$\begin{bmatrix} u_a \\ u_b \\ u_c \end{bmatrix} = \begin{bmatrix} v_{a0} \\ v_{b0} \\ v_{c0} \end{bmatrix} + \left(R + L\frac{d}{dt}\right) \begin{bmatrix} i_{a0} \\ i_{b0} \\ i_{c0} \end{bmatrix} + \begin{bmatrix} u_{060} \\ u_{060} \\ u_{060} \end{bmatrix} \qquad \begin{pmatrix} C10 \\ C11 \\ C12 \end{pmatrix}$$

When the AC system is balanced, there is no zero sequence voltage so u_{060} can be omitted. Further apply ABC − DQ transformation to C10 - C12:

$$\begin{bmatrix} E_{d20} \\ E_{q20} \end{bmatrix} = \begin{bmatrix} U_{d20} \\ U_{q20} \end{bmatrix} - \left(R + L\frac{d}{dt}\right) \begin{bmatrix} I_{d20} \\ I_{q20} \end{bmatrix} + \omega_1 L \begin{bmatrix} I_{q20} \\ -I_{d20} \end{bmatrix} \qquad \begin{pmatrix} C13 \\ C14 \end{pmatrix}$$

where E_{d20} and E_{q20} are the DQ arm voltage for 20 Hz. In this form, decoupled control can be applied to form the inner current loop. At the 20 Hz side, the outer loop is selected to control active power. The 60 Hz side can be derived using similar approach. Or alternatively, after the ABC − αβ0 transformation, apply Park transformation to three sets of equations in alpha/beta frame. At symmetrical state, the cluster voltages are balanced [82], so V_{adq}, V_{bdq} and V_{cdq} can be denoted as E_{d60} and E_{q60} uniformly:

$$\begin{bmatrix} E_{d60} \\ E_{q60} \end{bmatrix} = -\begin{bmatrix} U_{d60} \\ U_{q60} \end{bmatrix} - \left(R + L\frac{d}{dt}\right)\begin{bmatrix} I_{d60} \\ I_{q60} \end{bmatrix} + \omega_3 L \begin{bmatrix} I_{q60} \\ -I_{d60} \end{bmatrix} \qquad \begin{matrix} C15 \\ C16 \end{matrix}$$

Outer loop is selected to balance the capacitor voltage of three clusters respectively. Take cluster A for instance, the differential equation of the 40 Hz capacitor voltage ripple can be calculated as:

$$C \cdot \dot{U_{dc\_a2}} = -\frac{E_a I_a}{2U_{DC}} \cos(2\omega_1 + \alpha_1 + \beta_1) \qquad (C17)$$

Cluster B and C are similar and transform the equations for three clusters into DQ frame, Equations (5.11) and (5.12) can be derived.